

COMPUTATIONAL FLUID DYNAMIC ANALYSIS OF
HIGHWAY BRIDGE SUPERSTRUCTURES
EXPOSED TO HURRICANE WAVES

by

Mehrdad Bozorgnia

A Dissertation Presented to the
FACULTY OF THE USC GRADUATE SCHOOL
UNIVERSITY OF SOUTHERN CALIFORNIA

In Partial Fulfillment of the
Requirements for the Degree
DOCTOR OF PHILOSOPHY
(CIVIL ENGINEERING)

December 2012

Copyright 2012

Mehrdad Bozorgnia

I would like to dedicate this dissertation work to my beloved family.

Acknowledgments

Many people have provided their help and encouragement during this dissertation study. This work would not have been done without them. I like to specially thank my advisor, Professor Jiin-Jen Lee, who not only gave me the great opportunity to pursue a Ph.D. degree at the University of Southern California, but also provided invaluable advice, assistance, and encouragement throughout the whole study.

I also like to thank other members of the dissertation committee, Professors Carter Wellford, Vincent Lee, and Iraj Nasserri in the Department of Civil and Environmental Engineering and Professor James Moore in the Department of Industrial and System Engineering at USC, for their guidance and help.

I would like to thank all of my past and present group members: Jen Chang, Chanin Chaun-Im, Marmar Ghadiri, Ziyi Huang, Hyoung-Jin Kim, Zhiqing Kou, Shentong Lu, Yuan-Hung Tan, Ben Willardson, and Xiuying Xing (following the alphabetic sequence of the last names, no special order) for their incessant help and the warm atmosphere they provided since I came to USC.

I would like to thank High-Performance Computing and Communications staff especially, Brian Mendenhall for his countless hours of assistance in setting up the CFD software on HPCC Linux cluster and for continuous support and assistance throughout different phases of this thesis.

I would like to thank Shane Gillis from CD-adapco for his valuable advice regarding application of the CFD software to wave-bridge interaction problem and for continuous support and assistance throughout different phases of this thesis.

My very special thanks goes to my parents Fatemeh Sakhdari and Ahmad Bozorgnia, and my lovely sister Dr. Mehrshid Bozorgnia and all those with whom I have shared my life in the past five years. In particular I would like to thank Hossein Ataei, Hossein Hayati, Reza Jafarkhani, Mohammadreza Jahanshahi, Hadi Meidani, and Arash Noshadravan. I wish you a life full of success, health and happiness.

Contents

| | |
|---|-------------|
| Dedication | ii |
| Acknowledgments | iii |
| List of Figures | viii |
| List of Tables | xiii |
| List of Notations | xiv |
| Abstract | xvi |
| Chapter 1 INTRODUCTION | 1 |
| 1.1 Background | 1 |
| 1.2 Objective and Scope of Present Study | 5 |
| Chapter 2 LITERATURE SURVEY | 7 |
| Chapter 3 MATHEMATICAL FORMULATION OF PROBLEM | 16 |
| 3.1 Introduction | 16 |
| 3.2 Governing Equations | 16 |
| 3.3 Discretization | 18 |
| 3.3.1 Momentum Equation in Discrete Form | 19 |
| 3.3.2 Continuity Equation in Discrete Form | 20 |
| 3.4 SIMPLE Solver Algorithm | 22 |
| 3.5 Numerical Method for Solving Algebraic Equations | 24 |
| 3.6 Multigrid Concept | 26 |
| 3.7 Multiphase Methods | 30 |
| Chapter 4 MODEL VALIDATION FOR UPLIFT FORCES ON FLAT PLATE | 34 |
| 4.1 Solitary Wave | 34 |
| 4.2 Interaction of Solitary Wave with Platform over Horizontal Bottom | 36 |

| | |
|---|------------|
| Chapter 5 EXPERIMENTAL SETUP AND NUMERICAL METHODOLOGY | 41 |
| 5.1 Experimental Setup | 42 |
| 5.2 Computation on High Performance Computing and Communications Center (HPCC) at USC | 48 |
| 5.3 Numerical Methodology and Solver Parameters | 53 |
| 5.4 Choice of Wave Profile | 54 |
| 5.5 Choice of Boundary Conditions | 56 |
| 5.6 Choice of Mesh Size and Time Step | 57 |
| 5.7 Solution Convergence | 63 |
| 5.8 Spectral Analysis | 66 |
| 5.9 Slamming Force and Structural Response | 67 |
| Chapter 6 NUMERICAL RESULTS FOR LARGE SCALE WAVE BRIDGE INTERACTION | 73 |
| 6.1 2D Model | 73 |
| 6.1.1 Simulation Results for Test #1 | 74 |
| 6.1.2 Simulation Results for Test #2 | 77 |
| 6.1.3 Simulation Results for Test #3 | 85 |
| 6.2 3D Model | 90 |
| 6.2.1 Simulation Results for Test #4 | 92 |
| 6.2.2 Simulation Results for Test #5 | 95 |
| 6.2.3 Simulation Results for Test #6 | 98 |
| 6.3 Discussion on Slamming Force | 111 |
| 6.4 Discussion on Simulation Results | 114 |
| 6.5 Guidelines for Choosing Mesh and Time Step Size in Wave-Structure Interaction Problems | 117 |
| 6.6 Viscous Effects | 118 |
| Chapter 7 SCALE EFFECTS ON HYDRODYNAMIC FORCES AND COMPARISON OF SIMULATED FORCES TO AASHTO GUIDELINES | 123 |
| 7.1 Scale Effects | 123 |
| 7.2 AASHTO Guidelines | 132 |
| 7.3 Comparison of Simulated Wave Forces to AASHTO Guidelines | 135 |
| Chapter 8 RETROFITTING OPTIONS AVAILABLE FOR COASTAL BRIDGES EXPOSED TO WAVES | 140 |
| 8.1 Airvents in Bridge Deck | 141 |
| 8.2 Airvents in Bridge Diaphragm | 148 |
| Chapter 9 CONCLUDING REMARKS | 153 |

| | |
|--|------------|
| Reference List | 159 |
| Appendix A DISCRETIZATION SCHEMES USED IN STAR CCM+ | 163 |
| A.1 Transport Equation in Discrete Form | 163 |
| A.2 Gradient Computation | 166 |

List of Figures

| | | |
|-----|---|----|
| 1.1 | Damage to the U.S. 90 Biloxi Bay bridge caused by Hurricane Katrina. This photo is taken looking northeast from Biloxi 9/21/05 (source Douglass et al. (2006)). | 2 |
| 1.2 | I-10 bridge, Mobile Bay, Alabama, damaged by Hurricane Katrina (source Douglass et al. (2006)). | 3 |
| 1.3 | I-10 bridge over Escambia Bay, Florida, damaged by Hurricane Ivan (Pensacola News Journal photo). | 3 |
| 3.1 | A typical CV and the notation used for cartesian 2D grid | 18 |
| 3.2 | Residual reduction pattern by iterative solver for different grid resolutions (adapted from Versteeg and Malalasekera (2007)) | 27 |
| 3.3 | V-cycle adapted from CD-adapco (2010) | 29 |
| 3.4 | Illustration of girds that are suitable (right) and unsuitable (left) for two phase flows using VOF model adapted from CD-adapco (2010) | 31 |
| 3.5 | Upwind, downwind and central cells used in the analysis (left) and convection boundedness criterion in the NVD diagram (right) adapted from CD-adapco (2010) | 33 |
| 3.6 | a) True interface b) Volume Fraction | 33 |
| 4.1 | Experimental setup (French 1969) for numerical model validation | 36 |
| 4.2 | Mesh used in the simulation | 37 |
| 4.3 | Horizontal water particle velocities $H/d=0.15, s/d=0.1, y/d=0.0, d=12'', L=2''$ | 37 |
| 4.4 | Horizontal water particle velocities $H/d=0.15, s/d=0.1, y/d=-0.5, d=12'', L=2''$ | 38 |
| 4.5 | Normalized total hydrodynamic force per unit width $H/d=0.24, s/d=0.2, L/d=4, d=15''$ | 39 |
| 4.6 | Normalized total hydrodynamic force per unit width $H/d=0.32, s/d=0.2, L/d=4, d=15''$ | 39 |
| 4.7 | Normalized total hydrodynamic force per unit width $H/d=0.4, s/d=0.2, L/d=4, d=15''$ | 40 |
| 5.1 | Elevation view of typical prototype bridge (courtesy of Thomas Schumacher, Oregon State University.) | 41 |
| 5.2 | Elevation view of wave flume with experimental setup (courtesy of Thomas Schumacher, Oregon State University). | 42 |

| | | |
|------|---|----|
| 5.3 | Pre-cast bridge specimen prior to attachment of deck (Bradner and Cox (2008)). | 43 |
| 5.4 | Test setup installed in Large Wave Flume (Bradner and Cox (2008)) . . | 44 |
| 5.5 | Elevation view (side) of test specimen and reaction frame along with horizontal and vertical load cells (Bradner and Cox (2008)) | 45 |
| 5.6 | Instrumentation plan for pressure gages and load cells; plan view (Bradner and Cox (2008)). | 45 |
| 5.7 | Photo of the bridge specimen during wave trial (Bradner and Cox (2008)). | 46 |
| 5.8 | Time series of total horizontal force (LC1+LC2) for wave trial 1325. Markers indicate data points used to compute mean positive and negative peak forces (Bradner and Cox (2008)). | 47 |
| 5.9 | Time series of total vertical force (LC3+LC4+LC5+LC6) for wave trial 1325. Markers indicate data points used to compute mean positive and negative peak forces (Bradner and Cox (2008)). | 47 |
| 5.10 | Horizontal and vertical reaction forces for various wave heights for T=2.5s (Schumacher et al. (2008)). | 48 |
| 5.11 | HPCC at USC. | 49 |
| 5.12 | Relationship between client and parallel server adapted from (CD-adapco (2010)) | 50 |
| 5.13 | Script used for submitting the CFD job to HPCC Linux cluster | 51 |
| 5.14 | Number of CPU per node vs speed-up | 52 |
| 5.15 | Total number of CPU vs speed-up | 52 |
| 5.16 | Applicability ranges of various wave theories (after Mhaut et al. (1968)). d: mean water depth; H: wave height; T: wave period; g: gravitational acceleration. | 55 |
| 5.17 | Incident wave generated using stokes fifth order theory for H=0.5m and T=2.5 s | 56 |
| 5.18 | Boundary Conditions used in 2D simulation cases | 57 |
| 5.19 | Mesh regions | 58 |
| 5.20 | Simulation domain dimension | 58 |
| 5.21 | Effect of time step choice on total horizontal wave forces for dt=0.02s and dt=0.004s | 61 |
| 5.22 | Effect of time step choice on total vertical wave forces for dt=0.02s and dt=0.004s | 61 |
| 5.23 | Convective Courant Number for Test #6 | 62 |
| 5.24 | Residuals for continuity and momentum equations | 64 |
| 5.25 | Convergence in several time steps | 65 |
| 5.26 | Convergence in one time step | 65 |
| 5.27 | Vertical force reaching asymptotic limit in one time step before going to next time step | 65 |
| 5.28 | Horizontal force power spectral density | 66 |
| 5.29 | Vertical force power spectral density | 67 |

| | | |
|------|---|-----|
| 5.30 | Typical vertical wave force versus time plot for a subaerial structure with girders adapted from (FDOT (2008)). | 67 |
| 5.31 | Spring-mass-dashpot system | 69 |
| 5.32 | Amplitude amplification as a function of forcing frequency and damping | 70 |
| 5.33 | Example of filtered and unfiltered vertical force for a subaerial slab. . . | 70 |
| 5.34 | Quasi steady vs. raw horizontal wave forces | 71 |
| 5.35 | Quasi steady vs. raw vertical wave forces | 72 |
| | | |
| 6.1 | Horizontal force simulation results for Test #1 | 75 |
| 6.2 | Vertical force simulation results for Test #1 | 76 |
| 6.3 | Comparison of horizontal and vertical simulation wave forces for Test #1 to experimental data | 76 |
| 6.4 | Horizontal force simulation results for Test #2 | 77 |
| 6.5 | Vertical force simulation results for Test #2 | 79 |
| 6.6 | Comparison of horizontal and vertical simulation wave forces for Test #2 to experimental data | 79 |
| 6.7 | Volume of fluid (VOF) scene for H=0.84m (Test #2) | 81 |
| 6.8 | Absolute pressure scene for H=0.84m (Test #2) | 82 |
| 6.9 | Velocity vector scene for H=0.84m (Test #2) | 83 |
| 6.10 | Velocity magnitude in horizontal direction for H=0.84m (Test #2) | 84 |
| 6.11 | Velocity magnitude in vertical direction for H=0.84m (Test #2) | 85 |
| 6.12 | Horizontal force simulation results for Test #3 | 87 |
| 6.13 | Vertical force simulation results for Test #3 | 88 |
| 6.14 | Comparison of horizontal and vertical simulation wave forces for Test #3 to experimental data | 88 |
| 6.15 | Volume of fluid (VOF) scene for H=0.84m, dt=0.02 (Test #3) | 89 |
| 6.16 | Meshed bridge in full 3D model | 90 |
| 6.17 | Meshed bridge in 3D model with symmetry plane | 90 |
| 6.18 | Comparison of total horizontal force in the full bridge superstructure model to the bridge superstructure model with symmetry plane | 91 |
| 6.19 | Comparison of total vertical force in the full bridge superstructure model to the bridge superstructure model with symmetry plane | 91 |
| 6.20 | Horizontal force simulation results for Test #4 | 93 |
| 6.21 | Vertical force simulation results for Test #4 | 94 |
| 6.22 | Comparison of horizontal and vertical simulation wave forces for Test #4 to experimental data | 94 |
| 6.23 | Horizontal force simulation results for Test #5 | 96 |
| 6.24 | Vertical force simulation results for Test #5 | 97 |
| 6.25 | Comparison of horizontal and vertical simulation wave forces for Test #5 to experimental data | 97 |
| 6.26 | Horizontal force simulation results for Test #6 | 99 |
| 6.27 | Vertical force simulation results for Test #6 | 100 |

| | | |
|------|---|-----|
| 6.28 | Comparison of horizontal and vertical simulation wave forces to experimental data for Test #6 | 100 |
| 6.29 | Comparison of positive and negative horizontal forces to experimental data | 101 |
| 6.30 | Comparison of positive and negative vertical forces to experimental data | 102 |
| 6.31 | Error distribution for quasi-steady horizontal wave forces for Test #6 . . | 102 |
| 6.32 | Error distribution for quasi-steady vertical wave forces for Test #6 . . . | 103 |
| 6.33 | Volume of fluid (VOF) scene for H=0.84m (Test #6) | 105 |
| 6.34 | Pressure scene for H=0.84m (Test #6) | 106 |
| 6.35 | Velocity vector scene for H=0.84m (Test #6) | 107 |
| 6.36 | Velocity magnitude in horizontal direction for H=0.84m (Test #6) | 108 |
| 6.37 | Velocity magnitude in vertical direction for H=0.84m (Test #6) | 109 |
| 6.38 | 3D iso surface for H=0.84m (Test #6) | 110 |
| 6.39 | Pressure measurement taken beneath the deck adapted from Bradner and Cox (2008) | 111 |
| 6.40 | Corresponding measurement of the nearest load cell adapted from Bradner and Cox (2008) | 111 |
| 6.41 | Vertical force time history for one wave period for Test #6 for different wave heights | 113 |
| 6.42 | Effect of model choice and mesh size on magnitude of slamming force oscillation | 113 |
| 6.43 | Comparison of horizontal forces using SST K-Omega model to inviscid model for H=0.34m for Test #6 | 120 |
| 6.44 | Comparison of vertical forces using SST K-Omega model simulation to inviscid model for H=0.34m for Test #6 | 121 |
| 6.45 | Comparison of vertical forces using SST K-Omega model simulation to inviscid model for H=0.84m for Test #6 | 121 |
| 6.46 | Comparison of vertical forces using SST K-Omega model simulation to inviscid model for H=0.84m for Test #6 | 122 |
| 7.1 | Horizontal force simulation results for prototype bridge vs. results archived from model bridge using Froude similitude law | 126 |
| 7.2 | Vertical force simulation results for prototype bridge vs. results archived from model bridge using Froude similitude law | 127 |
| 7.3 | Volume of fluid (VOF) scenes for H=4.2m wave interacting with prototype bridge | 128 |
| 7.4 | Pressure scenes for H=4.2m wave interacting with prototype bridge . . . | 129 |
| 7.5 | Velocity magnitude in horizontal direction for H=4.2m wave interacting with prototype bridge | 130 |
| 7.6 | Velocity magnitude in vertical direction for H=4.2m wave interacting with prototype bridge | 131 |
| 7.7 | Nomenclature in equation 7.3 and 7.2 adapted from AASHTO (2008) . | 134 |

| | | |
|------|--|-----|
| 7.8 | Comparison of simulated forces for model bridge to AASHTO guideline | 136 |
| 7.9 | Comparison of simulated quasi-steady forces for model bridge to AASHTO guideline | 137 |
| 7.10 | Comparison of simulated forces for prototype bridge to AASHTO guideline | 138 |
| 7.11 | Comparison of simulated quasi-steady forces for prototype bridge to AASHTO guideline | 138 |
| 8.1 | Retrofit option 1 | 141 |
| 8.2 | Volume of fluid (VOF) scene for option 1 | 142 |
| 8.3 | 3D iso surface for option 1 | 143 |
| 8.4 | Effect of option 1 retrofit on horizontal force time history for H=0.34m | 145 |
| 8.5 | Effect of option 1 retrofit on horizontal force time history for H=0.84m . | 145 |
| 8.6 | Effect of option 1 retrofit on vertical force time history for H=0.34m . . | 146 |
| 8.7 | Effect of option 1 retrofit on vertical force time history for H=0.84m . . | 146 |
| 8.8 | Effect of option 1 retrofit on horizontal force for various wave heights . | 147 |
| 8.9 | Effect of option 1 retrofit on vertical force for various wave heights . . . | 148 |
| 8.10 | Retrofit option 2 | 149 |
| 8.11 | Effect of option 2 retrofit on horizontal force time history for H=0.34m . | 150 |
| 8.12 | Effect of option 2 retrofit on horizontal force time history for H=0.84m . | 150 |
| 8.13 | Effect of option 2 retrofit on vertical force time history for H=0.34m . . | 151 |
| 8.14 | Effect of option 2 retrofit on vertical force time history for H=0.84m . . | 151 |
| 8.15 | Effect of option 2 retrofit on horizontal force for various wave heights . | 152 |
| 8.16 | Effect of option 1 retrofit on vertical force for various wave heights . . . | 152 |
| A.1 | decomposition used in calculation of Diffusion term | 165 |

List of Tables

| | | |
|-----|--|-----|
| 5.1 | Properties of model test specimen and corresponding prototype bridge (Bradner and Cox (2008)) | 43 |
| 5.2 | Solver settings used in all simulations | 54 |
| 5.3 | Mesh sizes and time steps investigated | 59 |
| 6.1 | Different mesh sizes and time steps investigated in 2D model | 74 |
| 6.2 | Different mesh sizes and time steps investigated in 3D model | 92 |
| 6.3 | Error witnessed in simulation results for different Test cases | 115 |
| 6.4 | Mesh used in Test #6 in terms of wave length λ and wave height H (λ is calculated for $H=0.84\text{m}$) | 118 |
| 7.1 | Example of relationship between model and prototype wave condition . | 124 |

List of Notations

| | | |
|----------------|---|----|
| ' | correction (superscript) | 20 |
| * | Predictor value (superscript) | 20 |
| 0 | cell-0 quantity (subscript) | 19 |
| 1 | cell-1 quantity (subscript) | 19 |
| α_i | volume fraction of the i th phase | 32 |
| γ_f | Rhie-Chow-type dissipation | 20 |
| μ_{eff} | effective dynamic viscosity | 17 |
| ω | under-relaxation factor | 24 |
| $\vec{\alpha}$ | face metric quantity | 19 |
| ϕ | scalar quantity | 24 |
| V | control volume | 17 |
| v | fluid velocity vector | 17 |
| A | coefficient matrix | 26 |
| a | face area vector | 19 |
| a | linear coefficient | 21 |
| b | residual vector | 24 |
| b | vector of all body forces | 17 |
| ds | vector between cell centroids | 19 |
| e | error vector | 26 |
| f | face value (subscript) | 19 |

| | | |
|-------------|--|----|
| I | identity matrix | 17 |
| k | iteration k (superscript) | 24 |
| n | neighbor coefficient (subscript) | 21 |
| p | center coefficient (subscript) | 21 |
| p | pressure | 19 |
| r | residual (scalar) | 21 |
| T | iteration matrix | 26 |
| T | viscous stress tensor | 17 |
| t | time | 17 |
| x | solution vector | 26 |
| y | approximate solution vector | 26 |
| ρ | fluid density | 17 |
| v_g | grid velocity | 17 |
| G_f | grid flux | 20 |
| Q_f | coefficient in dissipation | 20 |
| \dot{m}_f | face mass flow | 20 |

Abstract

Highway bridges are one of the most vulnerable critical components of transportation system. Several coastal highway bridges were severely damaged during past hurricanes due to hurricane induced storm surge. The total cost of bridge repair or replacement after Hurricane Katrina was estimated to exceed 1 billion dollar TCLEE (2006).

The objective of this study is to calculate the hydrodynamic forces applied to bridge superstructure due to hurricane induced wave via Computational Fluid Dynamic (CFD) with an emphasis on the effect of air entrapment under highway bridge superstructure. Three dimensional numerical wave-load model based on two-phase Navier-Stokes equations is used to evaluate dynamic wave forces exerted on the bridge deck. In order to accurately capture the complex interaction of waves with bridge deck, several millions of mesh cells are used in the simulation domain and simulations are ran on High Performance Computing and Communication Center (HPCC) cluster at University of Southern California.

First, CFD software was validated by simulating interaction of a solitary wave with a flat plate. The simulation results for pressure under the plate and velocities at different points inside the simulation domain were compared with experimental data available from French (1970).

Second, validated numerical model was applied to a 1:5 scale old Escambia Bay bridge which was heavily damaged during Hurricane Ivan. Compared to simple flat

plate problem, Highway bridge superstructure is more challenging due to its complex geometry, bluff profile, and other complexities rising from trapped air under bridge superstructure, turbulence, structural response and scale effects. Simulation results were compared to experimental data available from the O.H. Hinsdale Wave Research Laboratory at Oregon State University. Influence of modeling (2D vs 3D), time step, grid size and viscous effects on total hydrodynamic forces applied to highway bridge superstructure have been investigated. Some guidelines based on simulation results are developed for the best mesh configuration and optimum choice of mesh size and time step for similar wave-structure interaction problems.

Third, in order to evaluate scale effects in the wave-bridge interaction problem, a bridge prototype with exact old Escambia Bay Bridge dimensions is setup. Equivalent wave heights and period are calculated using Froude similitude laws from the wave heights and periods used in model simulations. The forces obtained from CFD simulations for prototype bridge are compared to forces calculated using Froude similitude law from model bridge simulations. Next, CFD simulation results for model and prototype bridge are compared with recently published AASHTO guidelines for coastal bridges vulnerable to storms (AASHTO (2008)).

Forth, since air entrapped between bridge girders and diaphragm was determined to be a major contributing factor behind many highway bridge failures during recent hurricanes , two retrofitting options are evaluated in terms of their efficacy in reducing hydrodynamics forces applied to bridge superstructure. These two options include using airvents in bridge deck and using airvents in bridge diaphragms.

Chapter 1

INTRODUCTION

1.1 Background

The problem of wave-structure interaction has long been of interest to civil and ocean engineers as marine structures are constructed to interact with ocean waves. Accurate determination of wave forces on structures including both the impact and uplift forces plays an important role in design of safe and economical hydraulic structures.

At the beginning of September 2005, Hurricane Katrina stroked the coasts of Alabama, Mississippi and Louisiana. Hurricane Katrina was the fourth strongest hurricane to record which claimed a large number of casualties and was responsible for extensive damage to civil engineering infrastructure at various locations along the Gulf coast FEMAa (2006) FEMAb (2006). According to Houston et al. (2005), more than quarter million people were displaced and more than 1,000 people lost their lives, and the property damage exceeded 100 billion dollars. The 9 m water surge generated by the hurricane is the highest storm surge ever recorded in the United States. Apart from extensive damage to offshore oil rigs and pipe lines in the Gulf of Mexico, civil engineering infrastructure, including levees, highway, roads, bridges, ports, and harbors throughout the north Gulf Coast in Louisiana, Mississippi, and Alabama suffered substantially by the generated surge and waves. The cost of rebuilding all the coastal bridges damaged by Hurricane Katrina (2005) and Ivan (2004) will exceed 1 billion dollars TCLEE (2006).



Figure 1.1: Damage to the U.S. 90 Biloxi Bay bridge caused by Hurricane Katrina. This photo is taken looking northeast from Biloxi 9/21/05 (source Douglass et al. (2006)).

Bridges are one examples of hydraulic structures heavily damaged during Hurricane Katrina and Ivan and are vital components of the nations transportation network . Figure 1.1 shows I-10 bridge across Biloxi Bay and Bay St. Louis in Mississippi where the simple span bridge decks have moved off the pile caps to the left except where they were at higher elevations on the approach to a ship channel in the background. Figure 1.2 shows I-10 bridge across Mobile Bay in Alabama which was also extensively damaged during Hurricane Katrina. Figure 1.3 shows I-10 bridge over Escambia Bay, Florida which was damaged by Hurricane Ivan. A more comprehensive listing of bridges damaged by Hurricane Katrina can be found in TCLEE (2006).

Damage to bridges is caused as the storm surge raises the water to an elevation where larger waves can strike the bridge super structure. Storm waves produce both horizontal and vertical forces on bridge superstructure. Hydrodynamic forces when combined with buoyancy forces produced by air pockets trapped under the bridge decks can significantly damage bridge superstructure. Estimating magnitude of these forces



Figure 1.2: I-10 bridge, Mobile Bay, Alabama, damaged by Hurricane Katrina (source Douglass et al. (2006)).



Figure 1.3: I-10 bridge over Escambia Bay, Florida, damaged by Hurricane Ivan (Pensacola News Journal photo).

are needed in order to evaluate stability and structural response of these structures during extreme events such as hurricanes.

Problems in science and technology are usually addressed via two complementary approaches: experimental and analytical. In many applications such as the fluid mechanics of streams or wave impact on bridges, the governing equations are non linear and,

except in special circumstances, analytical solutions are not available. While, it is possible to address some of these problems through experiment, full scale experiments are not usually possible for problems such as wave-bridge interaction because simply such models can not be built in Lab environment. Therefore, researchers usually use smaller scale and simplified representation of the physical configuration and extrapolate results to apply to actual conditions. Some degree of uncertainty will remain in this extrapolation and use of simplified experiments to predict the behavior of the complex physical system.

Recently, with the help of powerful supercomputers and Computational Fluid Dynamic (CFD) programs, a third approach became available. CFD can complement the experimental and analytical approaches by numerically solving the underlying governing equations that represent the flow of fluids. CFD enables scientists to model true geometry of the given physical condition and can include actual observed boundary conditions that might be impossible to represent in laboratory experiments. In addition, CFD allows for parametric studies on material properties and physical conditions that might be expensive or time consuming to perform experimentally. CFD, also allows for modeling various "what-if" scenarios which might be very costly to do in laboratory environment. CFD modeling should ideally include all of the physical processes such as wave breaking, non linear effects, irregularity of waves, energy dissipation to friction and turbulence, air entrapment and entrainment, etc... However, due to complexities involved some degree of simplification is required to get solution to the problem. These simplifications are discussed and justified in the following chapters.

1.2 Objective and Scope of Present Study

The major objective of the present study is to investigate the wave hydrodynamic effects on highway bridge superstructures. A numerical wave-load model based on two-phase Navier-Stokes type equations is used to evaluate dynamic wave forces exerted on these hydraulic structures with special emphasis on the effect of air entrainment and entrapment. The Volume of Fluid method (VOF) is adopted in the model to describe dynamic free surface, which is capable of simulating complex discontinuous free surface associated with wave-deck interactions.

For present study the flow is assumed to be inviscid. Assumption of no viscosity is valid for present study, because we are dealing with large amplitude waves interaction with bridge superstructure in a very short time. This makes the inertia term in Navier Stokes equation much more important than viscous term and hence making the viscous effect negligible. This assumption greatly simplifies our numerical discretization schemes as allows for solving Euler equations instead of full Navier Stokes equations.

Chapter 2 includes brief review of previous numerical and experimental studies about hydrodynamic forces on hydraulic structures. In Chapter 3 the mathematical formulation of the problem is described which includes underlying equations and discretization schemes used to discretize these equations. Chapter 4 includes numerical model validation for uplift forces on a flat plate. Chapter 5 Explains the experimental setup used at O.H. Hinsdale Wave Research Laboratory at Oregon State University and solver settings and parameters used in the CFD software. Chapter 6 presents the numerical results and their comparison to experimental data available from Oregon State University. Chapter 7 investigates effects of scaling in wave-bridge interaction problem and validity of Froude similitude law to extrapolate simulation results from model to prototype. It also compares the simulation results for both model and prototype bridge to the latest AASHTO guidelines. Chapter 8 explores retrofitting efficacy of some of

the retrofitting options recommended in literature to protect the bridges against violent waves. Chapter 9 summarizes the findings of this dissertation.

Chapter 2

LITERATURE SURVEY

In this Chapter previous investigations on wave-structure interaction will be briefly reviewed. Most of published research studies regarding wave forces on hydraulic structures is based on laboratory experiments.

El.Ghamry (1963) conducted extensive experiments on docks supported by piles over flat and sloping bottoms. His experiments were conducted in a 105 ft long, 1 ft wide wave flume with monochromatic waves with variable wave height, period and clearance above the still water. El.Ghamry (1963) found that the force time history was a function of wave period and elevation of the deck above still water. He also found that the force time history consisted of positive uplift force due to boundary condition imposed on velocity and negative uplift force associated with advance of the trough under the deck. He then modified his experimental setup to quantify the role of entrapped air under the deck by using structural members such as beams and diaphragms. He reported that for certain wave periods, for slopping beach cases, air entrapment could cause impulsive uplift forces up to 100 times greater than the loads measured in other tests where the wave condition did not trap air.

Wang (1967) used linear wave theory and general impulse momentum relation to calculate impact pressure based on mass of the amount of water responsible for impact and velocity at the instant of contact. He also used Eulerian equations to arrive at a relation for slowly varying pressure in terms of incident wave characteristics. In addition, Wang (1970) conducted some experiments on dispersive waves interacting with a flat plate made of plexiglass at Naval Civil Engineering Laboratory which was 94 ft long,

92 ft wide and 3 ft deep. These tests were done for plate suspended at clearances varied from 0 to 0.125 ft above the still water level and at various distances from the wave generator. Like El.Ghamry (1963) Wang concluded that pressure time history consisted of two parts: a very short-duration impact pressure and a longer duration, slowly varying pressure. He compared both slowly varying and impulsive impact pressure to theoretical values he previously calculated. The recorded impact pressure correlated poorly with theoretical values and slow rising pressure component was about one to two times the hydrostatic pressure while the duration of this loading depended on how long the wave was in contact with structure.

French (1970) at California Institute of Technology conducted experiment on interaction of solitary wave with a horizontal platform with positive soffit clearance. Experiments were performed in a horizontal channel 24 inch deep 15 1/2 inch wide and 100 ft long. He used a horizontal flat, aluminum plate 15 inch wide, 1/2 inch thick and 5 ft long instrumented with pressure transducers, which was placed about 75 ft away from the wave generator. He performed his experiments by considering variety of wave heights, deck clearances, and water depths. He concluded that the peak pressure was subject to considerable variance because of entrained air in the flow near the wave front. He also showed that slowly varying pressure was approximately equal to incident wave height less the soffit clearance above still water level and normalized negative pressure was found to depend on the ratio of soffit clearance to still water depth and ratio of platform length to still water depth.

Denson (1978) and Denson (1980) studied wave loads on a (1:24) model bridge similar to U.S. 90 Bay St. Louis bridge damaged by surge and wave in Hurricane Camille. He used monochromatic waves with period of $T = 3$ s and varied the elevation of the deck, the water depth, and wave height. He concluded that during Hurricane

Camille, wave induced moments caused the most damage. He proposed stronger anchorage of bridge deck to its supports which was very inexpensive and simple for mitigating damage to bridge superstructure. His experiments had some fundamental problems due to very small flume dimensions and lack of sufficient explanation about force measuring apparatus which was used in his experiments Douglass et al. (2006). Denson (1980) reports significantly higher wave loads in his 1980 experiments. He does not explain the reason, but he mentions that the difference to his old experiments is likely due to inclusion of structural diaphragms in his basin models that were not included in his earlier flume tests.

Iradjpanah (1983) and Lai (1986), studied wave uplift pressures on horizontal platforms with positive soffit clearance. They used Finite element method to investigate aspects of wave hydrodynamic effects on a horizontal platform over horizontal sea bottom. Hydrodynamic equations of motion for each element were independently mapped in to group of simple geometry planes using isoparametric procedure. The resulting discrete equations were solved iteratively using multi grid method. Their numerical results agreed well with French (1970) work.

Kaplan (1992) Kaplan et al. (1995) modified traditional Morison's equation by including inertia and drag terms and presented a theoretical model for determining the time history of impact loads on horizontal circular members and horizontal decks on offshore oil exploration and production platforms. He concluded that vertical loads on decks were about 8 times as large as horizontal loads and that vertical loads reduce to approximately horizontal loads when the deck is removed leaving only the deck beams. One of major assumptions he made in deriving these formulas was that wave kinematics were not greatly affected by the structure. This is not necessarily applicable to highway bridge superstructures as submerged bridge decks are likely to have some significant interactions with the incident wave kinematics Douglass et al. (2006).

Bea et al. (1999) and Bea et al. (2001) presented a method to estimate horizontal wave forces on offshore oil and gas exploration rigs. Total buoyancy force in their method includes four components: a drag force (horizontal, velocity dependent), a lift force (vertical, velocity dependent), an inertial force (acceleration dependent), and a slamming force that occurs as the wave crest first hits the platform deck. His method can be used for estimating hydrodynamic forces on highway bridge superstructures however it requires empirical coefficients appropriate to these specific structures and needs to be extended to be able to calculate vertical forces as well.

Overbeek and Klabbers (2001) assumed that wave induced loads consist of a slowly varying pressure accompanied by short duration impact pressure. He related the slowly varying pressure to the difference between the elevation of the crest of the maximum wave and the elevation of the bottom of the deck and impact pressure to maximum wave height. In his formulas for impact and slowly varying pressure, he neglected the dynamic effect and assumed that no water exist on top side of the deck. Both formulas for impact and slowly varying pressure contain empirical coefficients for which he recommends different values.

McConnell et al. (2004) conducted extensive experiments on wave loads on horizontal decks elevated above still water level at HR Wallingford laboratory in England and came up with empirical formulas similar to Overbeek and Klabbers (2001). Their tests were done in wave flume with modern wave generating capabilities at nominal Froude scale of 1:25 and varied significant wave height between 0.1m and 0.22m, mean wave period between 1 to 3 seconds, water depths between 0.75 m and 0.6 m and deck elevations above still water level between 0.01 m to 0.16 m. Like others he found that force time history consisted of slowly varying load with period consistent with wave period and a very short duration impact pressure. Their experimental setup allowed for individual measurement of loads on individual portions of their typical deck, including

internal beams and bridge girders as well as seaward and internal deck sections. This means, to calculate total force applied to bridge superstructure, one needs to add the loads from individual portions of an elevated deck together to obtain and estimate of the total load. Also their experimental setup did not allow for air entrapment and during experiments water was observed to vertically shoot out of the gaps between their deck and beam sections.

Douglass et al. (2006) provided a comprehensive report titled " Wave Forces on Bridge Decks" which includes a summary of most of empirical methods available in the literature for design of coastal bridges till 2006. This report includes case studies concerning recent damage to highway bridge structures during Hurricane Katrina and Ivan. They also conducted experiments at the three dimensional (3-D) wave basin in the Haynes Laboratory at Texas A&M University. The laboratory model was scaled using the Froude criteria. Selecting a model:prototype scale of 1:15 gave a deck with dimensions of approximately 32 inches by 48 inches. The bottom of the girders was approximately 1.53 ft above the floor of the basin giving a prototype depth above bottom of 23 ft. At the end of this report they proposed an interim method for estimating wave loads on typical U.S. bridge spans. The formula proposed for estimating horizontal forces is a function of the projected area of the bridge deck onto the vertical plane, difference between the elevation of the crest of the maximum wave and the elevation of the centroid of bridge superstructure, and empirical coefficient which depend on the geometry of bridge superstructure. The formula proposed for estimating vertical forces is a function of the area of the bridge contributing to vertical uplift, the difference between the elevation of the crest of the maximum wave and the elevation of the underside of the bridge deck and an empirical coefficient which can be 1 for most cases.

AASHTO (2008) have developed series of equations to calculate design loads on coastal bridges exposed to waves. These equations are designed to calculate Maximum

horizontal and vertical quasi-steady force, overturning moments and vertical slamming force. These equations are parametrization of the physical-based model (PBM) derived from Kaplan's equations of wave forces on platform deck structures, which was developed for offshore oil platforms Kaplan (1992), Kaplan et al. (1995). These equations account for the bridge span design (slab vs. girder), as well as the type of girders used. In addition, these equations also include the effect of air entrapment through Trapped Air Factor (TAF) which is applied to quasi-steady vertical forces. The recommended application of the TAF allows the designer to calculate a range of quasi-steady vertical forces based on the minimum and maximum of TAF. While the guidance is specific on calculating the range, it is left to the designer to determine the specific TAF used to calculate these forces.

(FHWA) (2009) used multidimensional programs to study hydrodynamic forces on flooded bridge decks. The study included experiments (physical modeling) at the TFHRC J. Sterling Jones Hydraulics Laboratory and High Performance Computational Fluid Dynamics (CFD) modeling at the Argonne National Laboratory. Their research included analysis of lift forces produced perpendicular to flow of a fluid; drag forces exerted on objects in the path of fluids; and moment coefficients. Overall calculated velocities using CFD software seemed quite comparable with experiments. The CFD models performed reasonably well at estimating the force coefficient for 6 girder bridge for certain ranges of inundation coefficients while they performed fairly poorly in reproducing the critical coefficient values.

Cuomo et al. (2009) presented findings from large scale (1:10 Froude scale) experimental work carried out in the wave basin of Yokohama Port and Airport Technical Investigation Office. Measurements from physical model tests were used to gain insight on the dynamics of wave-loading on coastal bridges and to drive a prediction method for both quasi static and impulsive wave load. In addition, they evaluated the effect of

air entrapment on quasi-static and impulsive wave in deck loads on coastal bridges and effect of using openings in the bridge deck. They also measured vertical wave loads applied to both transversal and longitudinal beams. Cuomo et al. (2009) experiments showed that overall, wave crest decay more rapidly when slots in the deck are left open, while waves seem to conserve their energy while traveling along the deck if the slots are kept closed. Cuomo et al. (2009) showed that allowing pressure to be released from top of the slab reduces the overall upward loads for all monitored structural members over most of the range of parameters tested. In addition, while openings are beneficial in reducing upward forces, downward wave-in-deck loads on beams might be amplified due to the presence of open slots in the bridge deck. Cuomo et al. (2009) did not evaluate the effect of openings on horizontal forces.

Bradner and Cox (2008) at Oregon State University, conducted the largest experiment to date to examine realistic wave forcing on a highway bridge superstructure. A 1:8 (Froude scale) reinforced concrete highway bridge superstructure specimen of old Escambia Bay bridge was constructed and tested under regular and random wave conditions over a range of water depths that included inundation of the structure. Their unique experimental setup allowed direct control of the stiffness of the horizontal support system to simulate different dynamic properties of the bridge substructure (columns, bent cap and foundation) thereby allowing the first dynamic testing of bridge structures subjected to wave loads. The load cell data collected in this experiment did not exhibit the slamming force suggested by previous research (Cuomo et al. (2009), McConnell et al. (2004)). The impact spike was witnessed in pressure gauge data collected between the girders, but was not seen in the external girders. Bradner and Cox (2008) explained that this lack of a pressure spike in the external girder pressures was because the air was allowed to vent at the external girders, while the air was trapped between the internal girders. Bradner and Cox (2008) attributed the compression of the trapped air to the

sharp increase in pressure. Their theory is consistent with the findings of Cuomo et al. (2009) and AASHTO (2008). Another interesting observation was the lack of an impact spike in the force data. They concluded that the lack of a slamming force was due to the mass of the structure and the experimental setup. They theorized that when wave strikes the bridge, an impact pressure is generated, but this pressure does not manifest itself as reaction forces at the bent cap because the large mass of the bridge superstructure dissipates this impact.

Huang and Xiao (2009) used a numerical wave-load model based on the incompressible Reynolds averaged Navier Stokes equations and $k-\omega$ equations to investigate dynamic wave forces exerted on the bridge deck. The model was first tested against experimental data of uplift wave forces on horizontal plates by French (1970). The validated model was then applied to investigate wave forces acting on the old Escambia Bay Bridge damaged in Hurricane Ivan. Wave forces on three different deck elevations were discussed and numerical results were also compared with available empirical equations. For the uplift force, the result obtained from numerical modeling was 6.3 percent higher than that from Douglass et al. (2006)s empirical method, and 21.1 percent higher than that from Bea et al. (1999)s method. For the horizontal force, the value from numerical modeling was 39.4 percent lower than that from Douglass et al. (2006)s empirical method, and 86.8 percent lower than Bea et al. (1999)s method. Huang and Xiao (2009) did not compare their simulation results of wave bridge interaction to any of available experimental data. They also did not address the issue of air entrapment which was the main cause of failure for several bridges failed during recent hurricanes (Douglass et al. (2006) and Chen et al. (ress)).

Jin and Meng (2011) used two different numerical models to analyze wave-structure interaction and compute wave loads. Computational Fluid Dynamic (CFD) software

Flow-3D was used to analyze the effects of green water loading and superstructure elevation on wave forces and a 2D potential flow model was used for computation of wave loads on bridge superstructure fully submerged in water. They validated the numerical model based on 2D potential flow model, by comparing the simulation results for a condition where the bridge superstructure was submerged to simulation results from Flow-3D. Since potential flow model was not capable of calculating hydrodynamic forces for cases where part of bridge superstructure was outside water, using Flow-3D results, relationships were derived for adjusting both horizontal and vertical forces based on bridge deck elevation. The validated model was then used to calculate hydrodynamic forces applied to the old Escambia Bay Bridge model build in Oregon State University (Bradner and Cox (2008)). The maximum error in horizontal and vertical force calculations was 16 and 18 percent respectively. The validated model was also applied to calculate hydrodynamic forces applied to exposed jetties (Cuomo et al. (2009)). Comparison between simulation and experiment for quasi-static uplift forces showed maximum error of about 5 percent. At the end parametric study was performed for a range of wave height, wave period, water depth, and bridge geometry. Equations for calculating wave loads on bridge superstructure were then developed by regression analysis. These equations were then applied to calculate wave forces on Biloxi Bay Bridge during Hurricane Katrina and the results were compared to the method of McConnell et al. (2004) and AASHTO (2008). The force calculated by McConnell et al. (2004) and AASHTO (2008) were much higher than forces calculated using potential flow theory. Like Huang and Xiao (2009), Jin and Meng (2011) made no reference to the issue of air entrapment under bridge superstructure and the potential flow theory was not able to model the air entrapment under bridge superstructure. Also in their calculations the viscous effects were neglected since their model did not include viscosity and turbulence.

Chapter 3

MATHEMATICAL FORMULATION OF PROBLEM

3.1 Introduction

In present thesis we made use of commercial CFD software STAR-CCM+. Below some principals based on which this software works are briefly explained. First, basic flow equations applicable to wave-bridge interaction problem are explained. Then discretization schemes based on which governing equations are discretized, are explained. At the end of this chapter, the numerical methods used to solve discretized governing equations are briefly explained. More information about these techniques can be found in large body of work by Demirdzic et al. (1993) and Demirdzic and Musaferiya (1995) and comprehensive manual that comes with STAR-CCM+ and the book by Ferziger et al. (2002).

3.2 Governing Equations

In this section, the basic flow equations are presented. Basic flow equation for this problem are integral form of Navier Stokes equations which include continuity (3.1) and momentum equations (3.2). These equations arise from applying Newton's second

law to fluid motion, together with the assumption that the fluid stress is the sum of a diffusing viscous term (proportional to the gradient of velocity) and a pressure term.

$$\frac{d}{dt} \int_V \rho dV + \int_S \rho(\mathbf{v} - \mathbf{v}_b) \cdot d\mathbf{a} = 0 \quad (3.1)$$

$$\frac{d}{dt} \int_V \rho \mathbf{v} dV + \int_S \rho \mathbf{v} \otimes (\mathbf{v} - \mathbf{v}_b) \cdot d\mathbf{a} = \int_S (\mathbf{T} - p\mathbf{I}) \cdot d\mathbf{a} + \int_V \rho \mathbf{b} dV \quad (3.2)$$

In these equations ρ is the fluid density, V is the control volume bounded by closed surface S , \mathbf{v} is fluid velocity vector whose components are u_i , \mathbf{v}_b is the velocity of CV surface, t is time, \mathbf{T} is viscous stress tensor and \mathbf{b} is vector of all body forces. Viscous stress tensor is defined as:

$$\mathbf{T} = \mu_{eff} [\nabla \mathbf{v} + \nabla \mathbf{v}^T - \frac{2}{3} (\nabla \cdot \mathbf{v}) \mathbf{I}] \quad (3.3)$$

Where μ_{eff} is effective dynamic viscosity of the fluid which is the sum of laminar and turbulent viscosities. Above equations are solved using Segregated Flow Model available in STAR-CCM+ software. The Segregated Flow model solves the flow equations (one for each component of velocity, and one for pressure) in a segregated, or uncoupled, manner. The linkage between the momentum and continuity equations is achieved via a predictor-corrector approach which includes a collocated variable arrangement and a Rhie-and-Chow-type pressure-velocity coupling combined with a SIMPLE-type algorithm (CD-adapco (2010)). In STAR-CCM+ software the Segregated Flow solver contains two other solvers: velocity solver and pressure solver. The velocity solver solves the discretized momentum equation to obtain the intermediate velocity field. The pressure solver solves the discrete equation for pressure correction, and updates the pressure field (CD-adapco (2010)).

3.3 Discretization

The equations in previous section are discretized according to Finite Volume method (FVM). In Finite Volume Method the solution domain is subdivided into a finite number of small cells called control volumes (CVs). Usually CVs are defined by a suitable grid and computational node is assigned to the CV center. All variations of FVM share the same discretization principals. They are different in relations between various locations within integration volume. The integral form of Navier Stokes equations are applied to each CV, as well as the solution domain as a whole. Summing all the equations for all CVs we obtain global conservation equation since surface integrals over inner CV faces cancel out. The final result is a set of linear algebraic equations with the total number of unknowns equal to the number of cells in the grid. Figure 3.1 show a typical 2D cartesian control volume.

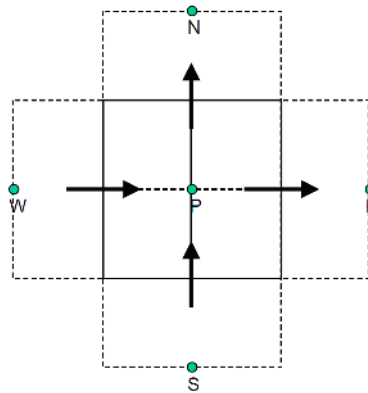


Figure 3.1: A typical CV and the notation used for cartesian 2D grid

For both surface and volume integrals, it is most convenient to use midpoint rule approximations because they result in a simple algebraic expressions that are second-order accurate. Since the values at center of CVs are calculated in each time step this means to simply multiply the CV-center value by the CV-volume V . For the calculation of surface integral, further approximations are necessary since variable are not known

at cell-face centers. Below discretization schemes used to discretize continuity and momentum equations are explained in more detail.

3.3.1 Momentum Equation in Discrete Form

Applying Equation 3.2 to a cell-centered control volume for cell-0, results in the following discrete equation for the transport of velocity (CD-adapco (2010)):

$$\frac{d}{dt}(\rho v V)_0 + \sum_f [v \rho (v - v_g) \cdot a]_f = - \sum_f (p I \cdot a)_f + \sum_f T \cdot a \quad (3.4)$$

The discrete equation for each velocity component may be expressed implicitly as a linear system of equation. The transient terms, body forces and convective flux for each velocity component is discretized based on discretization techniques explained for transport of a simple scalar quantity in Appendix A. To evaluate the stress tensor T , the velocity tensor gradient at the face ∇_{v_f} needs to be calculated in terms of cell velocities according to following formula (CD-adapco (2010)):

$$\nabla_{v_f} = \Delta v \otimes \vec{\alpha} + \bar{\nabla}_{v_f} - (\bar{\nabla}_{v_f} \cdot ds) \otimes \vec{\alpha} \quad (3.5)$$

Where $\Delta v = v_1 - v_0$ and $\bar{\nabla}_{v_f} = \frac{\nabla_{v_0} + \nabla_{v_1}}{2}$. Where ∇_{v_0} and ∇_{v_1} are the velocity gradient tensors at cells 0 and 1. The vector $\vec{\alpha}$ is $\vec{\alpha} = \frac{a}{a \cdot ds}$. For boundary faces depending on the flow regime (turbulent vs laminar) and the type of boundary condition used, STAR-CCM+ uses available information at the boundary to calculate stress tensor at the face (More information can be found in (CD-adapco (2010))).

3.3.2 Continuity Equation in Discrete Form

STAR-CCM+ discretizes continuity equation as follows (CD-adapco (2010)):

$$\sum_f \dot{m}_f = \sum_f (\dot{m}_f^* + \dot{m}'_f) = 0 \quad (3.6)$$

In equation 3.6, \dot{m}_f^* is uncorrected mass flow rate which is computed after the discrete momentum equation have been solved according to following equation (CD-adapco (2010)):

$$\dot{m}_f^* = \rho_f [a_f \cdot (\frac{v_0^* + v_1^*}{2}) - G_f] - \gamma_f \quad (3.7)$$

where v_0^* and v_1^* are the cell velocities after the discrete momentum equations have been solved. $G_f = (a \cdot v_g)_f$ is the grid flux which is zero if velocity of grid v_g is zero. γ_f is the Rhie-and-Chow-type dissipation at the face, given by:

$$\gamma_f = Q_f (p_1^* - p_0^* - \bar{\nabla} p_f^* \cdot ds) \quad (3.8)$$

where:

$$Q_f = \rho_f (\frac{V_0}{\bar{a}_0} + \frac{V_1}{\bar{a}_1}) \bar{\alpha} \cdot a \quad (3.9)$$

V_0 and V_1 are volumes for cell-0 and cell-1, respectively. \bar{a}_0 and \bar{a}_1 are the average of the momentum coefficients for all components of momentum for cell 0 and 1, respectively. p_0^* and p_1^* are the cell pressures from previous iteration. $\bar{\nabla} p_f^*$ is the volume-weighted average of the cell gradients of pressure, ∇p_0^* and ∇p_1^* . The mass flow correction \dot{m}'_f is given by the following equation (CD-adapco (2010)):

$$\dot{m}'_f = Q_f (p'_0 - p'_1) + \frac{\dot{m}_f^*}{\rho_f} (\frac{\partial \rho}{\partial p})_T p'_{upwind} \quad (3.10)$$

where p'_1 and p'_0 are the cell pressure corrections, and p'_{upwind} is given by:

$$p'_{upwind} = \begin{cases} p'_0 & \text{for } \dot{m}_f^* > 0 \\ p'_1 & \text{for } \dot{m}_f^* < 0 \end{cases} \quad (3.11)$$

The discrete pressure correction equation is obtained from Equations 3.6 and 3.10 and is written in coefficient form as:

$$a_p p'_p + \sum_n a_n p'_n = r \quad (3.12)$$

The residual r is simply the net mass flow into the cell:

$$r = - \sum_f \dot{m}_f^* \quad (3.13)$$

On the boundary faces where velocity is specified, such as walls, symmetry and inlet boundaries, the value of \dot{m}_f^* is calculated directly from known velocity v_f^* on boundaries according to the following equation (CD-adapco (2010)).

$$\dot{m}_f^* = \rho_f (a \cdot v_f^* - G_f) \quad (3.14)$$

For pressure correction Neumann condition is used:

$$p'_f = p'_0 \quad (3.15)$$

and the mass flux corrections are zero. For specified-pressure boundary condition, the pressure corrections will not be zero. The uncorrected boundary mass flux is given by following equation (CD-adapco (2010)):

$$\dot{m}_f^* = \rho_f(a.v_f - G_f) - \gamma_f \quad (3.16)$$

where v_f is boundary velocity and γ_f is dissipation coefficient given as:

$$\gamma_f = Q_f(p_f^* - p_0^* - \bar{\nabla} p_0^*.ds) \quad (3.17)$$

for subsonic outflow $p'_f=0$, $p'_{upwind} = p'_0$ and equation 3.10 becomes (CD-adapco (2010)):

$$\dot{m}'_f = [Q_f + v_f.a(\frac{\partial \rho}{\partial p})_T]p'_0 \quad (3.18)$$

for subsonic inflow, $p'_{upwind}=0$. The mass flow correction \dot{m}'_f is given by (CD-adapco (2010)):

$$\dot{m}'_f = \frac{v_f.aQ_f}{v_f.a - Q_f|v_f|^2} \quad (3.19)$$

and:

$$p'_f = \frac{|v_f|^2 Q_f}{Q_f|v_f|^2 - v_f.a} p'_0 \quad (3.20)$$

For supersonic inflow and outflow different formulas are provided which can be found in STAR-CCM+ manual. The discretization schemes provided above are chosen from STAR-CCM+ manual based on relevancy to our specific problem.

3.4 SIMPLE Solver Algorithm

SIMPLE is an acronym for Semi-Implicit Method for Pressure Linked Equations. In computational fluid dynamics (CFD), SIMPLE algorithm is a widely used iterative

numerical procedure to solve the Navier-Stokes equations. This method forms the basics of many commercial CFD packages. Application of SIMPLE algorithm to Navier Stokes equations in STAR-CCM+ includes the following steps (CD-adapco (2010)):

1. Set the boundary conditions.
2. Compute reconstruction gradient of velocity and pressure.
3. Compute velocity and pressure gradients.
4. Solve the discretized momentum equation to create the intermediate velocity field v^* .
5. Compute uncorrected mass fluxes at faces \dot{m}_f^*
6. Solve pressure correction equation to produce cell values of the pressure correction p' .
7. Update pressure field $p^{n+1} = p^n + \omega p'$ where ω is under relaxation factor for pressure.
8. Update boundary pressure correction p'_b
9. Correct face mass fluxes $\dot{m}_f^{n+1} = \dot{m}_f^* + \dot{m}'_f$
10. Correct cell velocities where $\nabla p'$ is gradient of the pressure corrections, a_p^v is vector of central coefficients for discretized linear system representing the velocity equation and V is cell volume.

$$v^{n+1} = v^* - \frac{V \nabla p'}{a_p^v} \quad (3.21)$$

11. Update density due to pressure changes.

12. Free all temporary storage.

STAR-CCM+ uses specific methods to calculate velocity and pressure gradients used in discretized continuity and momentum equations. These methods are explained in appendix A for a simple scalar ϕ .

3.5 Numerical Method for Solving Algebraic Equations

Application of finite volume discretization schemes described in previous sections to Navier Stokes equations will result in the coefficients of linear equation system that needs to be solved implicitly. The algebraic system for transported variable ϕ at a typical point p at iteration k+1 is written as (CD-adapco (2010)):

$$a_p \phi_p^{k+1} + \sum_n a_n \phi_n^{k+1} = b \quad (3.22)$$

where the summation is over all neighbor n of cell p. The right hand side b is evaluated from previous iteration and coefficients a_p and a_n are obtained directly from discretized equations. Allowing ϕ_p^{k+1} to change too much can cause instability, so we implicitly introduce ω to cut out steep oscillations. Equation 3.22 becomes (CD-adapco (2010)):

$$\frac{a_p}{\omega} \phi_p^{k+1} + \sum_n a_n \phi_n^{k+1} = b + \frac{a_p}{\omega} (1 - \omega) \phi_p^k \quad (3.23)$$

where k+1 implies the values after the solution is produced and source term at right hand side is evaluated at the previous iteration k. Rather than solving equation 3.23 for ϕ_p^{k+1} it is more convenient to cast into delta form defining $\Delta \phi_p = \phi_p^{k+1} - \phi_p^k$. System to be solved becomes (CD-adapco (2010)):

$$\frac{a_p}{\omega} \Delta \phi_p + \sum_n a_n \Delta \phi_n = b - a_p \phi_p^k - \sum_n a_n \phi_n^k \quad (3.24)$$

The right hand side $r = b - a_p \phi_p^k - \sum_n a_n \phi_n^k$ is termed the residual, and represents the discretized form of original transport equation at iteration k. The residual will be zero when the discretized equation is satisfied exactly.

System of equations arising from most realistic CFD problems are usually very large and contain several million equations. However these systems are usually sparse (have many zero entries). Any valid procedure can be used to solve these algebraic equations. However even with the latest advances in computer hardware technology, computational resources are still a major constraint. There are two family of solution techniques for linear algebraic equations: direct methods and indirect or iterative methods. Simple examples of direct methods are Cramer's rule matrix inversion and Gaussian elimination. Iterative methods are based on the repeated application of a relatively simple algorithm leading to eventual convergence after a sometimes large number of repetitions. Well known examples are Jacobi and Gauss-Seidel methods. The total number of iterations can not be predicted in advance and the convergence is not guarantee unless the system of equations satisfies fairly exact criteria. Iterative methods are usually far more efficient than direct methods for large equation sets. In addition Jacobi and Gauss-Seidel methods which are general purpose point iterative algorithms are easily implementable. The only problem with these iterative procedures is their convergence rate which can be really slow when the system of equations is large. Recently, multigrid acceleration techniques have been developed that have improved the convergence rate of iterative solvers to such an extent that they are now the method of choice in commercial CFD codes. Moreover, the SIMPLE algorithm for coupling of continuity and momentum equations is itself iterative. Hence, there is no need to obtain a very accurate intermediate solutions as long as the iteration process eventually converges to the true solution.

3.6 Multigrid Concept

As discussed, finite volume discretization of conservation equation on a flow domain results in a linear algebraic equation which in matrix form can be written as:

$$A.x = b \quad (3.25)$$

where vector x is true solution of system 3.25. If we solve this system with iterative method we obtain an intermediate solution y after some unspecified number of iterations. This intermediate solution does not satisfy 3.25 exactly and as before we define the residual as follows:

$$A.y = b - r \quad (3.26)$$

we can also define an error vector e as the difference between the true solution and intermediate solution:

$$e = x - y \quad (3.27)$$

subtracting 3.26 from 3.25 gives the following relationship between the error vector and the residual vector:

$$A.e = r \quad (3.28)$$

The residual vector can be easily calculated using iteration process by substituting solution into 3.26. For this we can write the system in iteration matrix of the following form (Versteeg and Malalasekera (2007)):

$$e^{(k)} = T.e^{(k-1)} + c \quad (3.29)$$

where matrix T depends on chosen iteration method, i.e. the Jacobi method or Gauss-Seidel method without or with relaxation. System 3.29 is important because it shows

how the error propagates from one iteration to the next. It also highlights the crucial role played by the iteration matrix. The properties of iteration matrix T determine the rate of error propagation and hence the rate of convergence. These properties have been studied extensively along with the mathematical properties of the error propagation as a function of iterative technique, mesh size, discretization scheme etc. It has been established that the solution error has components with the range of wave lengths that are multiples of mesh size. Iteration methods cause rapid reduction of error components with short wave lengths up to a few multiples of the mesh size. However long wave length components of error tend to decay very slowly as the iteration count increases (Versteeg and Malalasekera (2007)). Figure 3.2 shows this behavior.

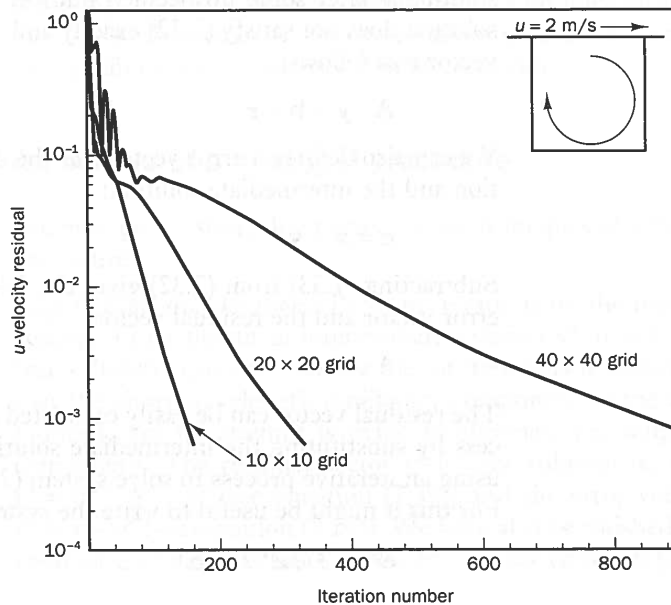


Figure 3.2: Residual reduction pattern by iterative solver for different grid resolutions (adapted from Versteeg and Malalasekera (2007))

For the coarse mesh, the longest possible wavelengths of error components are just within the short wave length range of mesh and hence all error components reduce

rapidly. On the finer meshes, however, the longest error wavelengths can not be eliminated as they fall outside the short-wavelength range for which decay is rapid. Multigrid methods are designed to exploit these inherent differences of the error behavior and use iteration on meshes of different size. The short wavelength errors are effectively reduced on the finest meshes, whereas the long wavelength errors decrease rapidly on the coarsest meshes. Moreover the computational cost of iterations is larger on finer meshes than on coarse meshes, so the extra cost due to iterations on the coarse meshes is offset by the benefit of much improved convergence rate (Versteeg and Malalasekera (2007)).

In general we have two types of Multigrid algorithms: geometric and algebraic. Geometric multigrid uses grid geometry and the discrete equation at the coarse level to arrive at the linear system to be solved on that level. Algebraic multigrid derives a coarse level system without reference to the underlying grid geometry or discrete equations. The coarse-grid equations are derived from arithmetic combinations of the fine-grid coefficients. Multigrid procedure involves the following steps:

- Agglomerate cells to form coarse grid levels.
- Transfer the residual from a fine level to a coarser level (known as restriction).
- Transfer the correction from a coarse level back to a finer level (known as prolongation).

since it is not always easy to get suitable discrete equations on the coarse grid using geometric multigrid techniques, algebraic multigrid (AMG) is clearly at an advantage. Therefore, it is used for the solution of all linear systems in the present thesis. AMG solver in STAR-CCM+ has two cycling strategies: fixed and flexible. Fixed cycling strategy includes recursive application of a single cycle which in STAR-CCM+ software includes the following steps (CD-adapco (2010)):

- (Pre)smooth

- Restrict
- Cycle a new
- Prolongate
- (Post)smooth

These steps are successively applied to sequence of courser grids (in geometric multi-grid) or equation sets (in AMG). In smooth step, relaxation sweeps are applied to the equations iteratively to archive new sets of corrections. Next, in restrict step, residuals are transferred back to the coarsest level where a new cycle is then applied. In prolongate step, the results from previous step are prolonged and transferred back to the fine level where smoothing is again applied. STAR-CCM+ software offers several fixed cycling strategies. More information about these cycling strategies can be found in CD-adapco (2010). Figure 3.3 shows the simplest fixed cycling strategy available in STAR-CCM+ software which is known as V cycle.

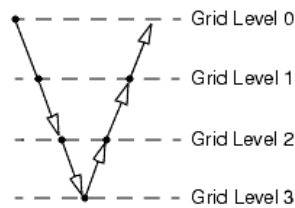


Figure 3.3: V-cycle adapted from CD-adapco (2010)

For systems that are not very stiff, its more economical to use flexible cycles. Instead of following a regular pattern, multigrid cycles are applied based on reduction that is witnessed in residuals. This means in flexible strategy residuals are constantly monitored and if the residuals exceed a given threshold, the solution will continue on a coarser level. On the other hand, if residuals on a given level are reduced more than a specific tolerance, the solution moves to a finer level.

3.7 Multiphase Methods

Multiphase flow refers to interaction of several phases with distinct physical properties and distinct physical interface between different phases. There are three methods to model multiphase flow each having its own advantages and suitable for specific application. These methods include:

1. Lagrangian multiphase model: This model is well suited for problems in which the interaction of the discrete phase with physical boundary is important. This is applicable to systems which are made of a single continuous phase carrying a relatively small volume of particles.
2. Eulerian multiphase model: This model can be used for systems consisting of two or more phases that are miscible or immiscible, and in any state of matter. In this method, separate conservation equation is solved for each phase and includes phase interaction model which defines how each phase influences other phase through interfacial area between phases.
3. Volume Of Fluid (VOF) multiphase model: This model is applicable to systems consisting of two or more immiscible fluid phases in which each phase occupies large domain within that system. This method has wide application in modeling free surface flow and fluid-structure interaction.

VOF multiphase model is a relevant model to wave-bridge interaction problem. VOF is a multiphase model which is well suited for simulation of flows where each phase constitutes a large structure, with relatively small total contact area between phases. The great advantage of VOF model is that it does not need to model inter-phase interactions therefore, it is computationally very efficient. However, it assumes that all phases within a partially filled cell, share the same velocity and pressure. For example if we

have water and air in one cell, both are assumed to have the same pressure and velocity. A good example of application of this method is in sloshing tanks. If the tank movement becomes very violent which result in breaking waves, large number of air bubbles and water droplets in the air, still VOF can be applied but needs very fine mesh in order to produce small modeling errors. VOF model is very sensitive to the grid used in simulation domain. Figure 3.4 shows proper and improper grid resolution that can be used to model air bubbles depending on their size in conjunction with VOF model.

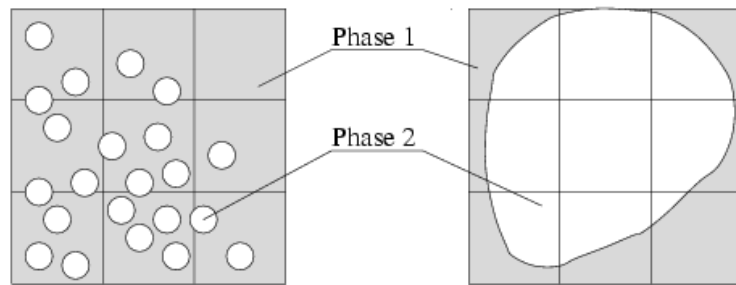


Figure 3.4: Illustration of grids that are suitable (right) and unsuitable (left) for two phase flows using VOF model adapted from CD-adapco (2010)

In VOF model spatial distribution of each phase at a given time is defined in terms of a variable called volume fraction α . Both fluids are treated as a single effective fluid whose properties vary in space according to the volume fraction of each phase, i.e.:

$$\rho = \sum_i \rho_i \alpha_i \quad (3.30)$$

$$\mu = \sum_i \mu_i \alpha_i \quad (3.31)$$

where $\alpha_i = \frac{V_i}{V}$ is the volume fraction and ρ_i and μ_i are the density, and molecular viscosity of the i th phase. For the case of two fluid mixture such as air and water mixture which is what we are dealing in this thesis we will have:

$$\rho = \rho_1\alpha_1 + \rho_2\alpha_2 = \rho_1\alpha_1 + \rho_2(1 - \alpha_1) \quad (3.32)$$

$$\mu = \mu_1\alpha_1 + \mu_2\alpha_2 = \mu_1\alpha_1 + \mu_2(1 - \alpha_1) \quad (3.33)$$

The transport of volume fraction α_i is described by the following conservation equation:

$$\frac{d}{dt} \int_V \alpha_i dV + \int_S \alpha_i (\mathbf{v} - \mathbf{v}_b) \cdot d\mathbf{a} = 0 \quad (3.34)$$

The discretization of transport equation 3.34 for α_i requires special care because α_i must be bound between zero and unity and the regions with partially filled cells should be as small as possible (Mozaferija and Peric (1998)). Equation 3.34 contains only convective fluxes and unsteady term. For time integration either fully implicit Euler method (for steady solution) or Crank-Nicolson (for unsteady solution) can be used. Discretization of convective term in Equation 3.34 is more critical. First order upwind scheme smears the interface too much and introduces artificial mixing of two fluids. Also since α must obey the bounds $0 < \alpha < 1$ one has to ensure that the scheme does not generate overshoots or undershoots. In addition, we have to ensure that convective flux out of one CV does not transport more of one fluid that is available in the donor cell. Also we have to take into account the interface orientation and local Courant number (Mozaferija and Peric (1998)). The sharpness between immiscible fluids is achieved by limiting the cell-face value to fall within shaded area of Normalized Variable Diagram (NVD) originally proposed by Leonard (1997) and shown in figure 3.5.

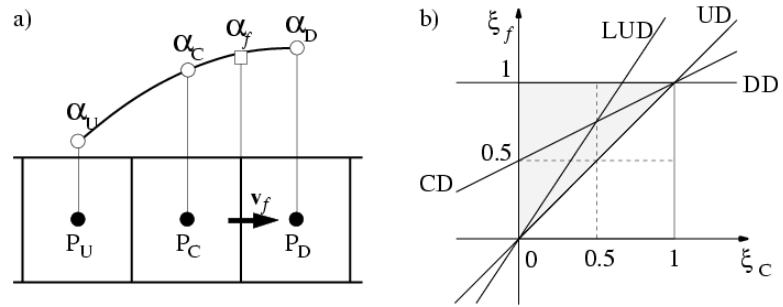


Figure 3.5: Upwind, downwind and central cells used in the analysis (left) and convection boundedness criterion in the NVD diagram (right) adapted from CD-adapco (2010)

More details about these methods can be found in (Mozaferija and Peric (1998)) and (CD-adapco (2010)). Figure 3.6 shows how free surface is constructed from volume fraction α using VOF multiphase model.

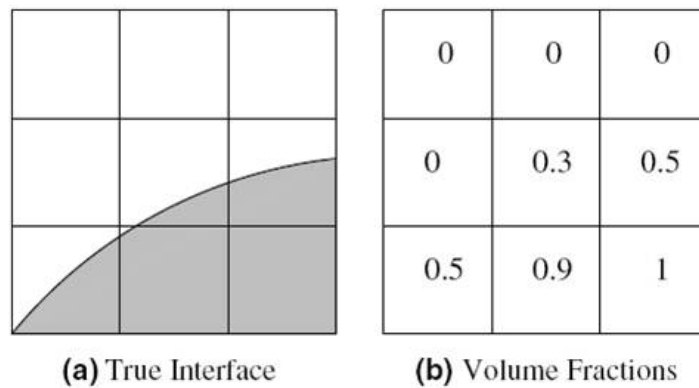


Figure 3.6: a) True interface b) Volume Fraction

Chapter 4

MODEL VALIDATION FOR UPLIFT FORCES ON FLAT PLATE

4.1 Solitary Wave

Before applying CFD software STAR-CCM+ to the wave-bridge interaction problem, the software is validated for the problem of a solitary wave interacting with a simple flat plate. Solitary wave is a relevant model of an ocean wave in shoal water. John Scott Russell in 1834 was the first to report on the wave, while conducting experiments to determine the most efficient design for canal boats. That is why, in fluid dynamics the wave is now called a Scott Russell solitary wave or soliton (Wikipedia (2012)).

There are several theoretical solutions of the solitary wave equations which are often referred to in literature. Boussinesq (1872) obtained an analytical solution for wave profile, wave propagation speed, and the water particle velocities. McCowan (1891) carried out the solution to the first order approximation and determined the wave profile, wave speed, fluid particle velocities, and an estimate of the limiting height of wave. Laitone (1963) obtained a solution similar to that of Boussinesq, but his solution contained higher order terms. Grimshaw (1970) proposed a third order solitary wave theory through a series expansions in terms of the relative wave amplitude. Fenton (1972) obtained a ninth order solution for the solitary wave. In his analysis, a form of solution was first assumed and then, coefficients were obtained numerically. Although Laitone (1963), Grimshaw (1970), and Fenton (1972) solitary wave theories are derived from

higher order approximation, the Boussinesq's solution has been found to agree better with experimental data Iradjpanah (1983). According to Boussinesq (1872) solitary wave height at different instances, wave speed, and fluid particle velocities are calculated as follows:

1. Wave profile

$$h(x, t) = H[\operatorname{sech}(\sqrt{\frac{3H}{4d}} \frac{X}{d})]^2 \quad (4.1)$$

where $X = x - ct$

2. Wave speed

$$c = \sqrt{g(d + H)} \quad (4.2)$$

3. Fluid particle velocities

$$\frac{u}{\sqrt{gd}} = \frac{h}{d} \left\{ 1 - \frac{h}{4d} + \frac{d}{3} \left(\frac{d}{h} \right) \left[1 - \frac{3}{2} \left(\frac{y}{d} \right)^2 \right] \frac{d^2 h}{dx^2} \right\} \quad (4.3)$$

$$\frac{v}{\sqrt{gd}} = -\frac{y}{d} \left\{ \left(1 - \frac{1}{2} \frac{h}{d} \right) \frac{dh}{dx} + \frac{d^2}{3} \left(1 - \frac{1}{2} \frac{y^2}{d^2} \right) \frac{d^3 h}{dx^3} \right\} \quad (4.4)$$

where H is the maximum wave height, d is the water depth and u and v are horizontal and vertical water particle velocities. Based on the theoretical expressions summarized above, a solitary wave is completely defined for a given water depth, d and its crest amplitude H . Experimental results by French (1970) also confirm that no theoretical profile fits the experimental data better than that of Boussinesq in the region of the wave crest. Since the region near the crest of the wave is the most important for examining the wave impact on platform which are located above the still water, great accuracy far from the crest is not as important. Thus Boussinesq profile is considered a proper model for this study.

4.2 Interaction of Solitary Wave with Platform over Horizontal Bottom

French (1970) conducted extensive laboratory experiments to analyze the wave uplift forces acting on coastal bridge decks by a solitary wave. The segregated flow model described in previous sections is used to simulate the wave uplift forces for the same experiment setup used by French (1970) and simulation results are compared with observed data as given by French (1970). The viscous effects are neglected in all simulation cases. The experimental setup is shown in figure 4.1. The mesh used in the simulation is shown in 4.2. As we see in 4.2 the mesh is refined in the regions occupied by water which includes the wave crest. The mesh size used in this region was $\Delta x = \Delta z = 0.003m$. The time step size of $\Delta t = 0.001s$ was used to ensure simulation accuracy.

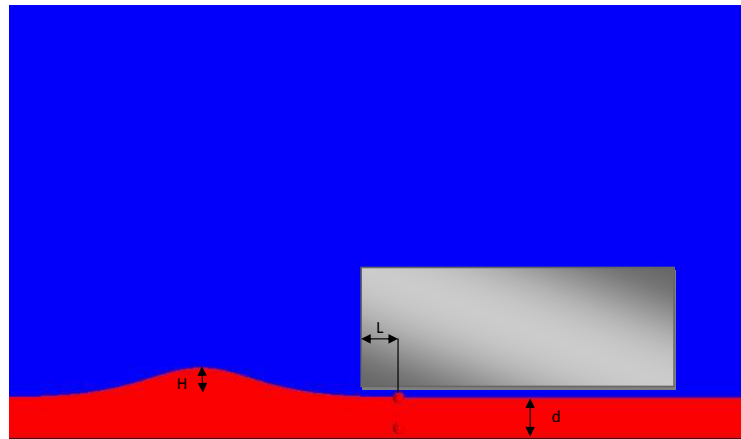


Figure 4.1: Experimental setup (French 1969) for numerical model validation

Figure 4.3 and 4.4 present the normalized horizontal velocities u/\sqrt{gd} as a function of non dimensional time $t\sqrt{g/d}$, at location $L = 2$ inch from the front edge of platform and vertical positions of $y/d = 0.0$ and $y/d = -0.5$, respectively for a platform with

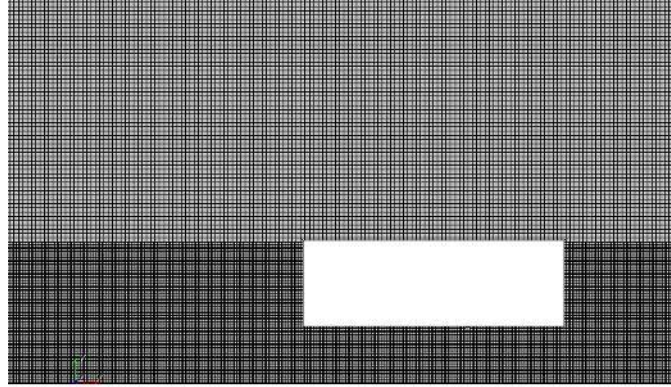


Figure 4.2: Mesh used in the simulation

relative soffit clearance of $s/d = 0.1$. The initial wave height generated was $H = 1.8$ inch and still water depth d was 12 in. In each figure, the experimental water particle velocity obtained by French (1970) is presented along with the particle velocity time-history obtained from present numerical simulations. In these figures, y is measured upward from still water surface and L is measured from the leading edge of platform. In general, the agreement between numerical results and experimental data is reasonably good for horizontal water particle velocities under the platform.

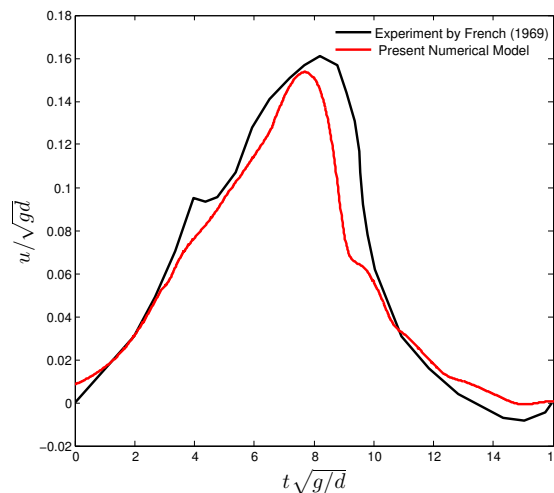


Figure 4.3: Horizontal water particle velocities $H/d=0.15, s/d=0.1, y/d=0.0, d=12'', L=2''$

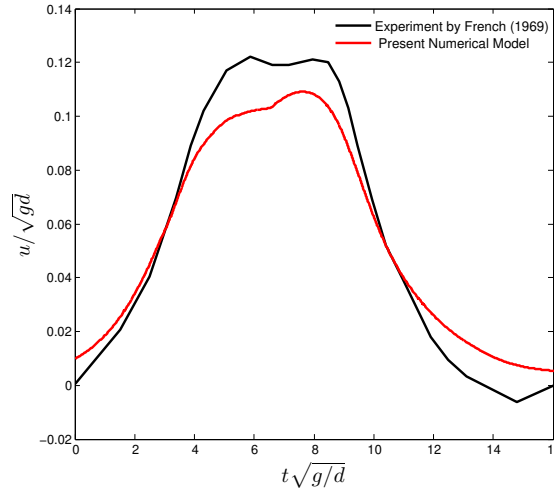


Figure 4.4: Horizontal water particle velocities $H/d=0.15, s/d=0.1, y/d=-0.5, d=12'', L=2''$

The Time history of the total hydrodynamic force per unit width of the platform is shown in Figure 4.5 through 4.7 for different relative wave heights; $H/d=0.24, 0.32$ and 0.4 respectively. The total hydrodynamic force per unit width is defined as the sum of the products of the computed uplift pressure and length of influence. In these figures, the total hydrodynamic force computed based on the present numerical model is normalized with respect to F_s , the total hydrostatic force due to undisturbed wave of height H less the soffit clearance s (this would be equivalent to the weight of water in the region above platform). The experimental result of French (1970) are also presented for comparison. In addition, simulation results for hydrodynamic forces, are compared with the results of two other numerical codes based on Finite Element Method (FEM) previously developed by Iradjpanah (1983) and Lai (1986). The results of present numerical simulations seems to be in better agreement with French (1970) experiments for all simulation cases.

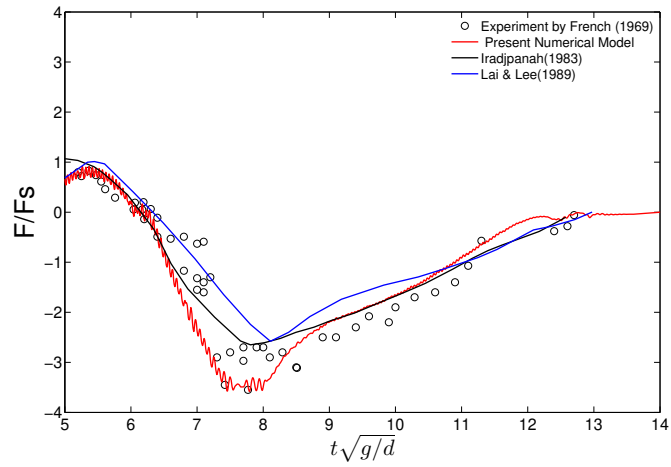


Figure 4.5: Normalized total hydrodynamic force per unit width $H/d=0.24$, $s/d=0.2$, $L/d=4$, $d=15''$

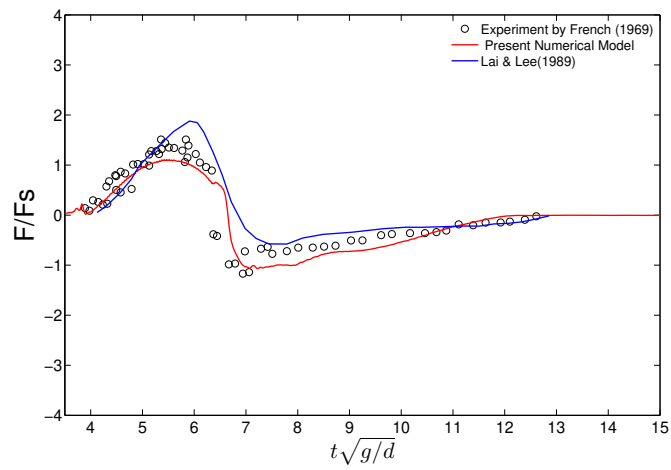


Figure 4.6: Normalized total hydrodynamic force per unit width $H/d=0.32$, $s/d=0.2$, $L/d=4$, $d=15''$

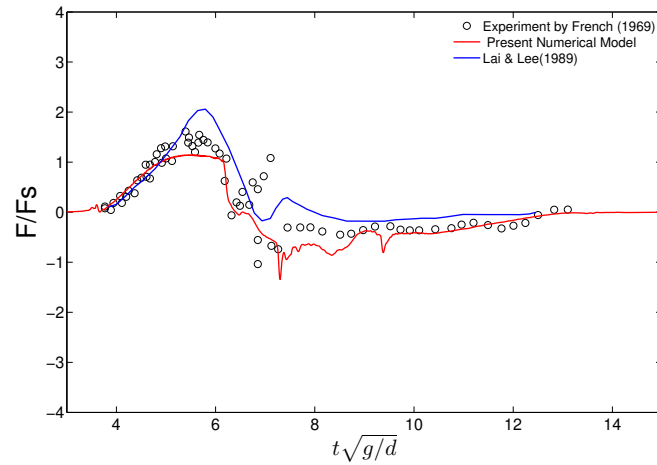


Figure 4.7: Normalized total hydrodynamic force per unit width $H/d=0.4$, $s/d=0.2$, $L/d=4$, $d=15''$

Time dependent total hydrodynamic force is very important for design of hydraulic structures. Dynamic analysis of the structure can make use of total hydrodynamic forces in the equations of motion to calculate structural response, structural displacements, and structural loadings, which include stresses and bending moments. Hydrodynamic forces calculated in this chapter agree well with experimental results of French (1970). This means STAR-CCM+ can confidently be used for calculating hydrodynamic forces applied to other hydraulic structures such as highway bridge structures. Application of STAR-CCM+ to highway bridge structure is presented in Chapter 5.

Chapter 5

EXPERIMENTAL SETUP AND NUMERICAL METHODOLOGY

Researchers at Hinsdale Wave Research Laboratory at Oregon State University Conducted the largest wave-on-bridge experiment to date. The bridge dimensions used in experiment was based on prototype dimensions taken from Florida Department of Transportation drawings of the old I-10 Bridge over Escambia Bay. A cross section of typical prototype bridge is shown in figure 5.1.

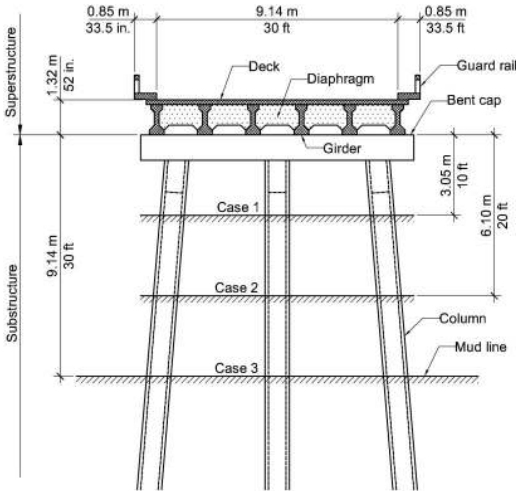


Figure 5.1: Elevation view of typical prototype bridge (courtesy of Thomas Schumacher, Oregon State University.)

In experiment, only the bridge superstructure was modeled because the prevailing mode of failure for most of the coastal bridge structures was due to damage to bridge

superstructure (Douglass et al. (2006)). In this research, we compared our numerical simulation results to experimental data available from Oregon State University. In the following sections, the experimental setup is explained in more detail.

5.1 Experimental Setup

At Hinsdale Wave Research Laboratory a 1:5 scale reinforced bridge superstructure specimen was constructed and tested under regular and random wave conditions over a range of water depths which include bridge inundation. Figure 5.2 shows the bathymetry of the large wave flume which consisted of impermeable 1:12 slope, followed by horizontal section approximately 30m in length and another 1:12 slope, to dissipate waves and minimize reflection off the beach. The wave maker used was a flap-type model capable of producing waves with maximum height of 1.6m at wave period of 3.5s.

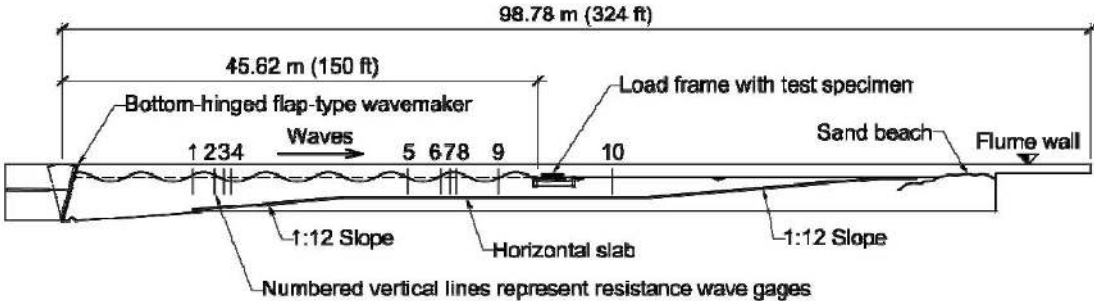


Figure 5.2: Elevation view of wave flume with experimental setup (courtesy of Thomas Schumacher, Oregon State University).

The test specimen consisting of six scaled AASHTO type III girders including the full complex cross-sectional geometry were constructed and connected with two steel rods through four diaphragms spaced along the span. All the seams between the girders and deck were sealed airtight with silicone. Figure 5.3 shows pre-cast bridge specimen

prior to attachment of deck. Overall dimensions and weight of bridge specimen and corresponding prototype is given in table 5.1.



Figure 5.3: Pre-cast bridge specimen prior to attachment of deck (Bradner and Cox (2008)).

| Parameter | Model (1:5) | | Prototype(1:1) | |
|---|-----------------------------|---------|----------------|----------|
| | Total span length, S | 3.45 m | 136 in | 17.27 m |
| Width ,W | 1.94 m | 76.4 in | 16.64 m | 54.6 ft |
| Girder height | 0.23 m | 9.0 in | 1.14 m | 45 ft |
| Girder spacing (CL to CL) | 0.37 m | 14.4 in | 1.83 m | 6.0 in |
| Deck thickness | 0.05 m | 2.0 in | 0.25 m | 10 in |
| Overall height, h_d | 0.28 m | 11.0 in | 1.40 m | 55 in |
| Span weight | 19.0 KN | 4270 lb | 2375 KN | 534 kips |
| Span mass | 1940 Kg | | 242 Ton | |

Table 5.1: Properties of model test specimen and corresponding prototype bridge (Bradner and Cox (2008))

To model substructure flexibility a pair of elastic springs whose stiffness were determined from finite element modeling of sub structure components were used. Columns and bent caps were modeled and the fundamental period T was calculated and converted to model scale using Froude Criteria. Assuming rigid connection between column and bent cap and pinned connection between bridge column and foundation, the period for

the prototype bridge (old I-10 bridge over Escambia Bay) was calculated to be 1.01 s, which is kinematically similar to 0.45 s for the scaled model. Based on this period, a spring is chosen to realistically model the bridge substructure (it is shown in figure 5.4).



Figure 5.4: Test setup installed in Large Wave Flume (Bradner and Cox (2008))

The bridge superstructure was heavily instrumented by load cells, pressure transducers, and strain gages. There were total of 2 horizontal load cells, 4 vertical load cells, 13 pressure transducers, and 11 strain gages used in experimental setup. Horizontal load cells were located between bent cap and end anchorage block and vertical load cells located between bent cap and linear guide rail system. Pressure transducers and strain gages were located at test specimen deck and girders. Load cells and pressure sensors are shown in figure 5.5 and 5.6 respectively. To measure water surface elevation, 10 surface piercing resistance wave gauges (WG) were placed along the length of flume (shown in figure 5.2). WG9 was placed approximately 4 m offshore of the specimen to measure water surface elevation in the vicinity of the specimen and WG10 was located 6 m onshore of the specimen. The sensors used for this experiments were 150 KHz resonant and were commonly used for steel structures (Bradner and Cox (2008)).

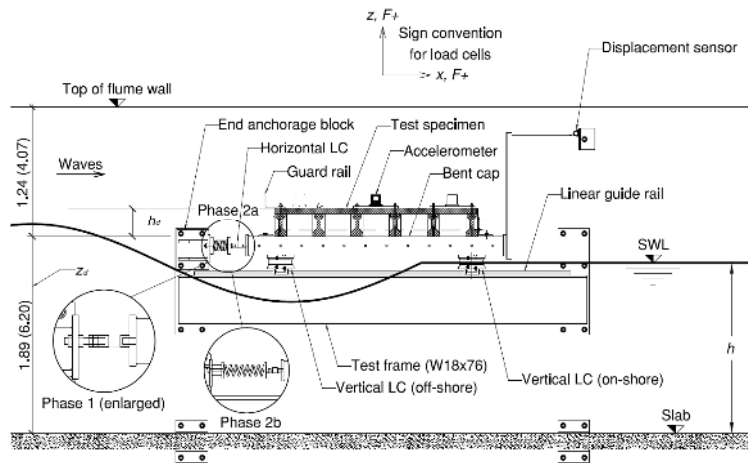


Figure 5.5: Elevation view (side) of test specimen and reaction frame along with horizontal and vertical load cells (Bradner and Cox (2008))

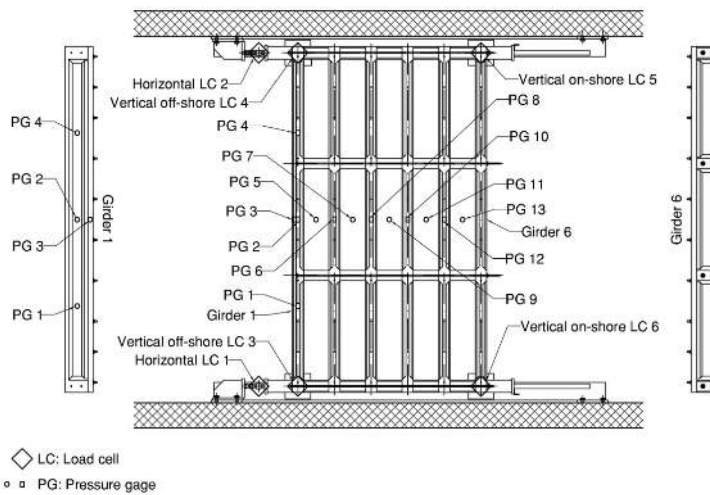


Figure 5.6: Instrumentation plan for pressure gages and load cells; plan view (Bradner and Cox (2008)).

All data were recorded using National Instruments 64-channel PXI-based real-time data acquisition system with minimum sampling rate of 250 Hz which was chosen after

finding little variation in the data among test trials which were sampled at higher rates (Bradner and Cox (2008)).

Wave heights and corresponding forces used in the analysis were taken from a window of time between the first wave striking the specimen and the observation of re-reflected waves in the incident wave data. The length of this window varied with wave celerity, and had an average of approximately 27 seconds. The number of waves and corresponding forces within this window ranged between 5 and 16 with an average of 8.3. Wave heights for different trials were calculated by taking the mean of the wave heights within this window. A photo of the tank condition during a typical wave trial is shown in figure 5.7.



Figure 5.7: Photo of the bridge specimen during wave trial (Bradner and Cox (2008)).

Forces are measured using six load cells (LCs) shown in figure 5.5. Total vertical force is calculated by adding data from load cells 3, 4, 5, and 6 (LC3, LC4, LC5, LC6). Horizontal forces are calculated by adding data from load cells 1 and 2 (LC1, LC2). Load cell data was zeroed out at the beginning of each trial, and as a result buoyancy forces due to a change of SWL are eliminated from load cell measurement. Figure 5.8 and 5.9 shows time series of total horizontal and vertical forces applied to bridge superstructure for wave trial of 1325 with wave height of $H = 0.5\text{m}$ and wave period of

$T = 2.5\text{s}$. Markers indicate data points used to calculate mean positive and negative peak forces.

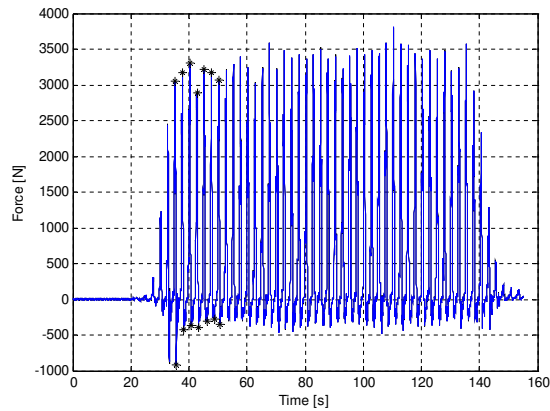


Figure 5.8: Time series of total horizontal force (LC1+LC2) for wave trial 1325. Markers indicate data points used to compute mean positive and negative peak forces (Bradner and Cox (2008)).

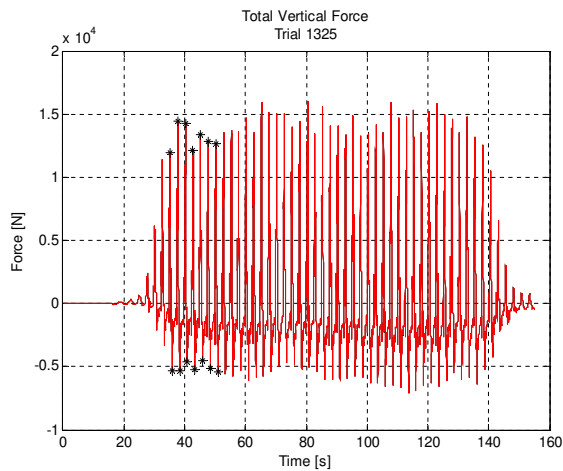


Figure 5.9: Time series of total vertical force (LC3+LC4+LC5+LC6) for wave trial 1325. Markers indicate data points used to compute mean positive and negative peak forces (Bradner and Cox (2008)).

There are two versions of experimental results available from Oregon State University. One by Bradner and Cox (2008) and another one by Schumacher et al. (2008). The results presented in Schumacher et al. (2008) were slightly different from those in Bradner and Cox (2008). In present research, We used the test results of OSU study by Schumacher et al. (2008). Because the superstructure was treated as fixed boundary in our analytical model, we selected test results of rigid setup for comparison. These experimental data are shown in figure 5.10.

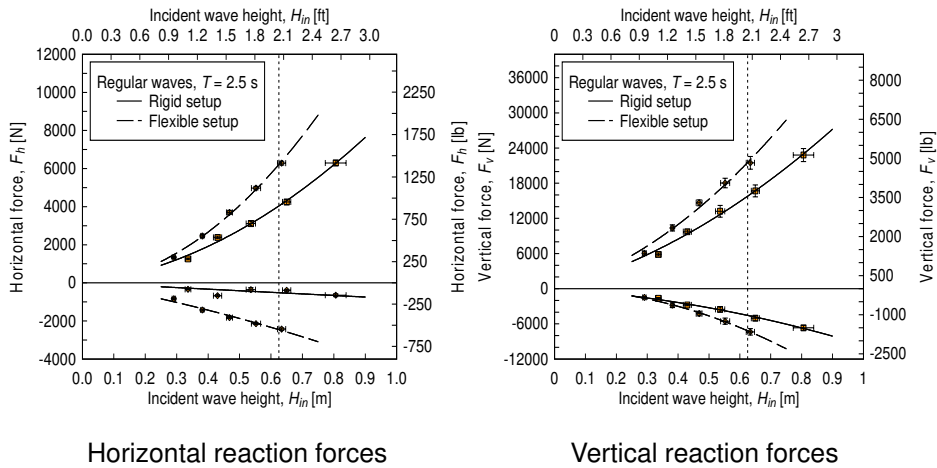


Figure 5.10: Horizontal and vertical reaction forces for various wave heights for $T=2.5$ s (Schumacher et al. (2008)).

5.2 Computation on High Performance Computing and Communications Center (HPCC) at USC

The computationally intensive CFD modeling programs such as the one used in present research requires enormous computing power. All the simulations in this research are done on High Performance Computing and Communication center (HPCC) at University of Southern California (figure 5.11). HPCC comprises a diverse mix of computing

and data resources. Two Linux clusters constitute the principal computing resource. In addition, HPCC has a central facility that provides more than 400 terabyte of combined disk storage and potential access to nearly a petabyte of tape storage, as well as a Condor cluster that uses spare cycles on UNIX workstations in USC's general-access computing rooms (source HPCC web site).



Figure 5.11: HPCC at USC.

HPCC has two Linux clusters: a 896 quad-core/dual-processor node on a 10-gigabit Myrinet backbone and a 1,795 dual-processor node of which nearly half are dual-core AMD Opteron processors on a 2-gigabit Myrinet network. For each cluster, the bidirectional, low-latency Myrinet fiber network interconnects the nodes, allowing for the development of massive production jobs that require high-speed communications among computational elements.

Parallel computing uses multiple processors to run simulation and thus allows solution of a large CFD problem in less physical time. It is highly desirable to compute CFD solutions in parallel because of the computationally intensive work required to acquire converged solutions. STAR-CCM+ can be run in parallel mode providing a scalable solution to solving problems faster and to attempting larger problems. The core of this functionality is based upon a data parallelism paradigm in which the mesh is distributed

across a number of processes. Each process applies numerical methods identical to those used in a serial solution. Communication between the processes ensures consistency with a serial solution. The parallel server is composed of N processes that each compute an equal share of the computational workload. The client only ever communicates with the first process in the parallel server which is referred to as the master process. This master process participates equally in the computational workload. Processes communicate with each other by passing messages. These messages conform to a programming standard known as the Message Passing Interface (MPI). STAR-CCM+ is designed to work with different implementations of MPI, such as HP MPI, Microsoft MPI and MPICH2. The relationship between client and parallel server is shown in figure 5.12.

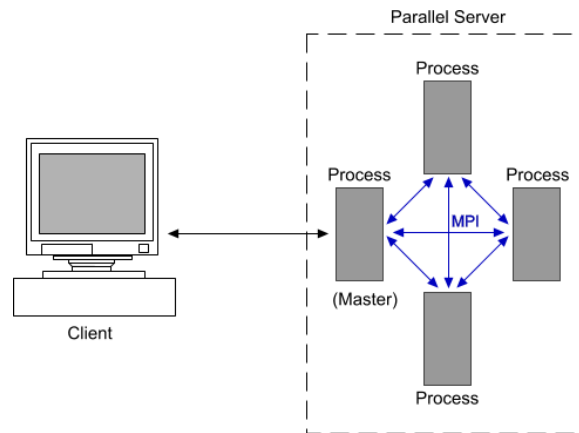


Figure 5.12: Relationship between client and parallel server adapted from (CD-adapco (2010))

Ideally a problem of a certain size ran on a four processors should take a fourth of the time required to converge when the code was run on one processor. However after doing few tests on HPCC it was verified that the maximum speed for simulation is achieved when around 200 CPUs are used. After this point as it is shown in figure 5.15 there is no gain in computational speed. In addition, it is possible to request up to 8

CPUs per node (each node contains up to 8 CPUs) However as it is seen in figure 5.14, its best to use 2 CPU per node instead of maximum of 8 CPUs per node because using 2 CPU per node configuration is almost 3 times faster than 8 CPU per node. This is important to note that these benchmarks are specific to the software used along with the size of the problem (number of mesh used in simulation domain), a modeling approach and many other parameters. This means for other problems with different mesh sizes or different modeling techniques we will have different benchmarks. In order to submit the simulation file to HPC cluster head node we have to use a pbs script as shown bellow:

```
#!/bin/tcsh

**** The "#PBS" lines must come before any non-blank non-comment lines
****
# be aware that 2 ##'s will comment out a #PBS directive

# the following line requests specific resources, 100 Dell pe1950 nodes
with 2 processors each
# this was to run the program on one thread for each physical socket
#PBS -l walltime=24:00:00,nodes=100:pe1950:myri:ppn=2

# following joins the stderr/stdout streams
#PBS -j oe

# All lines that begin with 'echo' are for informative purposes
# and will be saved in the JOBID-PBS-output.log file
echo
echo "Starting job on `date`."
echo "Running on the following nodes:"
echo `cat $PBS_NODEFILE | sort -u`

# set the number of processors based on the PBS_NODEFILE
set NP=`wc -l $PBS_NODEFILE|awk '{print $1}'`

set mycommand="/auto/rcf-proj/jj1/bozorgni/newbest/STAR-CCM+
7.04.011/star/bin/starccm+"
# arguments for $mycommand
set myargs="-mpi myrinet-mx -rsh /usr/bin/ssh -power -np $NP -
machinefile $PBS_NODEFILE -batch H=0.84-3D.sim"

# change to our working directory (where you submitted the job from)
cd "$PBS_O_WORKDIR" || exit 1

# run the command with the specified arguments, save output to 'logfile-
DATE'
$mycommand $myargs >& logfile-128cpus-`date +%Y%m%d%H%M`
# set your return code (0 = no errors, anything larger then 0 is an
error code)
set ret=$?

echo "The command ($mycommand $myargs) produced the following return
code: $ret"

echo "Job complete at: `date`"
echo
exit $ret
```

Figure 5.13: Script used for submitting the CFD job to HPC Linux cluster

In the above script we are requesting 100 pe1950 nodes with 2 CPU's per each node for 24 hours. Where pe1950 nodes are Dual Quadcore Intel Xeon with 2.33 GHz CPU speed and 12GB of memory.

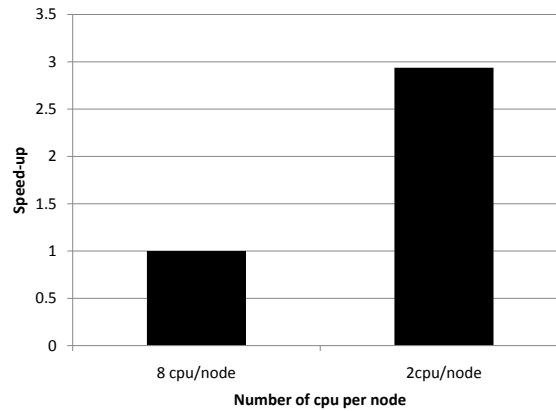


Figure 5.14: Number of CPU per node vs speed-up

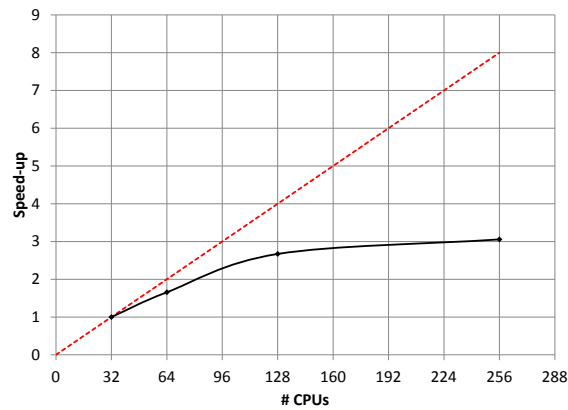


Figure 5.15: Total number of CPU vs speed-up

5.3 Numerical Methodology and Solver Parameters

STAR-CCM+ was configured to model the forces on the bridge deck in simulations. Building the CFD model involves selecting mesh resolution, simulation algorithm, boundary condition including air-water interface properties and turbulent model if required. In addition to testing the ability of numerical model to replicate the experimental data, the CFD simulation had secondary objective of determining best model setup to achieve most accurate simulation results. Several 2D and 3D models with different mesh sizes and time steps are tested. The CFD simulation were conducted with an eye on the efficiency of computational time. Even with HPC facility, the high computational intensity of CFD modeling demands an efficient model setup to ensure manageable run time. The 2D and 3D simulations were solved as isothermal (the temperature in the simulation domain was kept constant). The governing equation for 2D and 3D models first solved as inviscid. Inviscid simulation are the Euler equations described in chapter 3. Solving Euler equation will generate the local pressure and velocity components of fluid. STAR-CCM+'s multiphase segregated flow model is used to separate governing equation for both the water and air. The Segregated Flow solver controls the solution update for the Segregated Flow model according to the SIMPLE algorithm Ferziger et al. (2002). It controls two additional solvers: velocity solver and pressure solver. The velocity solver controls the under-relaxation factor and algebraic multigrid parameters for the momentum equations. More specifically, it solves the discretized momentum equation to obtain the intermediate velocity field. The pressure solver controls the under-relaxation factor and algebraic multigrid parameters for the pressure correction equation. More specifically, it solves the discrete equation for pressure correction, and updates the pressure field (CD-adapco (2010)). Water is modeled as incompressible fluid with density of $\rho = 997.561 \text{ kg/m}^3$ while air is modeled as a compressible ideal

gas. This model requires an extra equation, the equation of state to solve for compressible air density. The volume of Fluid (VOF) model in STAR-CCM+ (explained in chapter 3) is used to model air and water free surface interactions. The VOF model is used to setup the multiphase domain. The domain is initialized into water and air section with free surface set to lower bridge girder elevation in experiment. STAR-CCM+ currently allows for defining three types of waves: flat, first order, and fifth order wave. This model automatically sets up functions to be used for boundary conditions that will update with progression of waves. For VOF solver second order discretization scheme is used to discretize convection equation described in chapter 3. For temporal discretization solver the second order implicit scheme is used. With this model solutions are found at time steps and marched through time. The number of internal iteration For these simulations is chosen based on convergence. It is important to ensure convergence at each times step before going to the next time step. Convergence criteria used is explained in section 5.7. Table 5.2 shows the main solvers which are used to get the solution at each time step along with the corresponding parameters used to setup these solvers.

| Solver | Parameter | Value/scheme |
|-------------------|----------------------------------|--------------|
| Implicit Unsteady | Temporal Discretization | 2nd-order |
| Segregated Flow | Velocity Under Relaxation Factor | 0.6 |
| | Pressure Under Relaxation Factor | 0.2 |
| Segregated VOF | VOF Under Relaxation Factor | 0.9 |

Table 5.2: Solver settings used in all simulations

5.4 Choice of Wave Profile

For initial condition fifth order stokes wave was chosen to simulate wave conditions that were used in experiment. A fifth order wave is given by a fifth order approximation

to the Stokes theory of waves. This wave more closely resembles a real wave than one generated by the first order method. The wave profile and the wave phase velocity depend on water depth, wave height and current. This wave theory is only valid for Ursell numbers less than 30. Where Ursell number is given by equation (5.1). In this equation, H is the wave height λ is the wavelength and d is depth of water. There are also some guidelines in literature about applicability ranges of various wave theories figure 5.16 shows one of these guidelines which gives the appropriate wave order in terms of wave height, water depth and wave period. The detail formulation of fifth order waves can be found in Fenton (1972). In all the simulations water depth d is kept constant at $d=1.89\text{m}$, wave period T is also kept constant at $T=2.5\text{s}$ and wave height H varied between 0.34m to 0.84m .

$$U_R = \frac{H\lambda^2}{d^3} \quad (5.1)$$

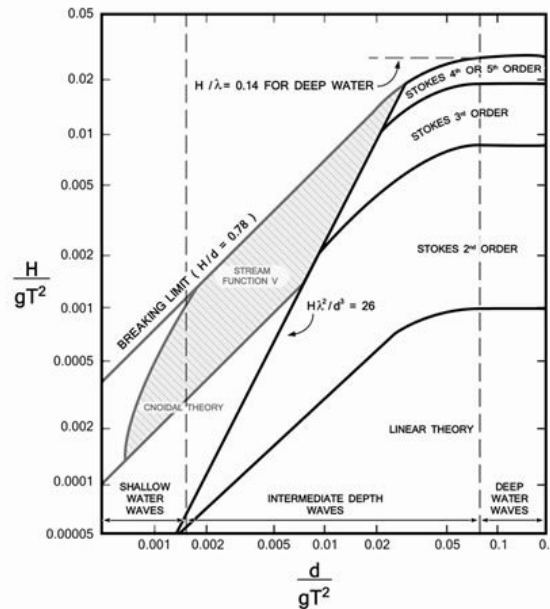


Figure 5.16: Applicability ranges of various wave theories (after Mhaut et al. (1968)).
 d : mean water depth; H : wave height; T : wave period; g : gravitational acceleration.

Figure 5.17 shows the wave generated using Stokes fifth order theory propagating from left to right in simulation domain for wave amplitude $H=0.5\text{m}$ and wave period $T=2.5\text{s}$.

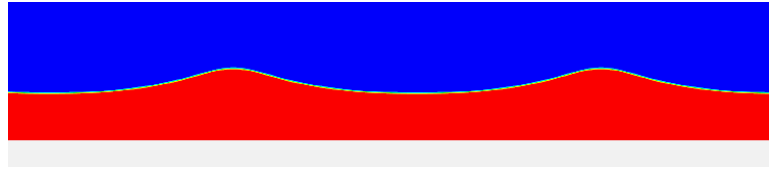


Figure 5.17: Incident wave generated using stokes fifth order theory for $H=0.5\text{m}$ and $T=2.5\text{ s}$

5.5 Choice of Boundary Conditions

Choice of boundary conditions is very important because it directly influences the simulation results. Following boundary conditions are used in the wave-bridge interaction simulations and are explained in detail:

- Wall
- Velocity Inlet
- Pressure Outlet
- Symmetry Plane

A wall boundary represents an impermeable surface. An impenetrable boundary for inviscid flows an impenetrable, no-slip boundary for viscous flow simulations. A pressure outlet boundary is a flow outlet boundary at which the pressure is specified. A velocity inlet boundary represents the inlet of a duct at which the flow velocity is known. For the wall boundary condition, the normal velocity is explicitly set to zero. The boundary face pressure is extrapolated from the adjacent cell using reconstruction gradients.

This boundary condition is used for bridge superstructure and for top and bottom of the simulation domain. For the velocity inlet boundary condition, the inlet face velocity vector is specified directly. The boundary face pressure is extrapolated from the adjacent cell using reconstruction gradients. At the velocity inlet the velocity is specified according to the fifth order wave approximation. For the pressure outlet, the boundary face velocity is extrapolated from the interior using reconstruction gradients and the boundary pressure is specified. For the symmetry plane shear stress at a symmetry boundary is zero the face value of velocity is computed by extrapolating the parallel component of velocity in the adjacent cell using reconstruction gradients. The boundary face pressure is extrapolated from the adjacent cell using reconstruction gradients. These boundary conditions are shown in figure 5.18.

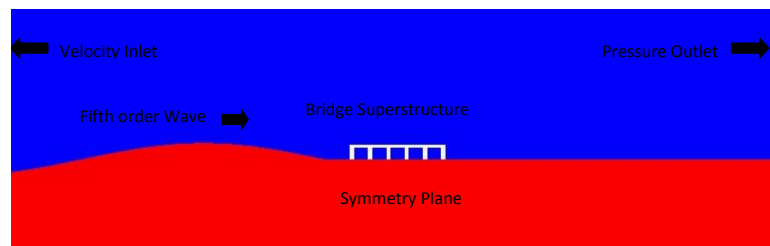


Figure 5.18: Boundary Conditions used in 2D simulation cases

5.6 Choice of Mesh Size and Time Step

The volume mesh in a simulation is the mathematical description of the space (or geometry) of the problem being solved. The mesh type and quality is an important factor in CFD simulations with implications on the model size, computational requirements, accuracy and convergence rate of solution. As the fluid flow is solved in two and three dimensions a 2D and 3D hexahedral grid is implemented. The cells are arranged fully orthogonal. Unstructured grid generation is used to save computational time with very

fine mesh around the bridge superstructure and coarse mesh in deep water and in air region. The grid around the bridge deck is generated more densely because flow pattern is more complex. These regions are shown in figure 5.19. In addition, 8m passed the bridge structure the mesh is coarsened to save the number of mesh used in simulation domain and also because this region is not of our interest. overall dimensions of meshed simulation domain is shown in figure 5.20. Special care need to be used in coarsening mesh in free surface to prevent wave reflection which may happen as a result of sudden increase in mesh size. Mesh sizes and time steps investigated are shown in table 5.3.

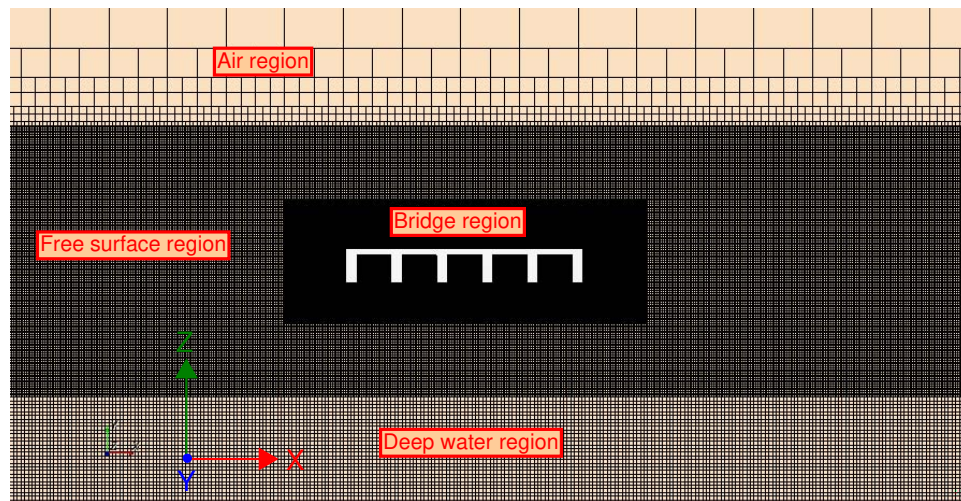


Figure 5.19: Mesh regions

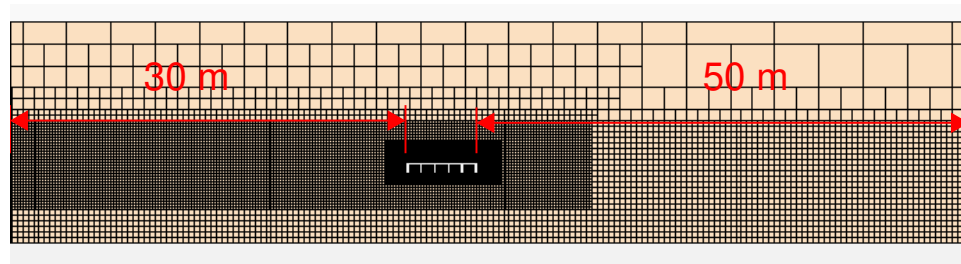


Figure 5.20: Simulation domain dimension

| Test | Model | $\Delta t(s)$ | Mesh size (cm) | | | | | | Total number of cells |
|------|-------|---------------|----------------|------------|--------------|------------|------------|------------|-----------------------|
| | | | Bridge | | Free surface | | Deep water | | |
| | | | Δx | Δy | Δx | Δy | Δx | Δy | |
| 1 | 2D | 0.02 | 0.72 | N/A | 2.4 | N/A | 4.8 | N/A | 733,537 |
| 2 | 2D | 0.004 | 1.44 | N/A | 2.4 | N/A | 4.8 | N/A | 358,659 |
| 3 | 2D | 0.02 | 1.44 | N/A | 2.4 | N/A | 4.8 | N/A | 358,659 |
| 4 | 3D | 0.02 | 1.44 | 5.76 | 4.8 | 11.52 | 9.6 | 23.04 | 2,834,678 |
| 5 | 3D | 0.004 | 1.44 | 5.76 | 4.8 | 11.52 | 9.6 | 23.04 | 2,834,678 |
| 6 | 3D | 0.004 | 0.72 | 2.88 | 2.4 | 11.52 | 9.6 | 23.04 | 11,483,096 |

Table 5.3: Mesh sizes and time steps investigated

For large problems such as wave bridge interaction its appropriate to divide the simulation domain into 4 regions:

- Air region: This region is located on top of free surface region. It is better to coarsen the mesh near the top boundary (pressure outlet) to avoid air recirculation. The mesh size in this region is not as critical as other regions.
- Free surface region: This is the region that contains both air and water. It should cover the whole wave height. The usage of appropriate mesh size in this region is critical. Using a very coarse mesh in this region causes wave breaking or dissipation. Using an extremely fine mesh in this area is a waste of computing resources.
- Deep water region: This region is located under the free surface region and only contains water. The mesh size in this region depend on the water depth and wave height. One way to find out about importance of this region is to look at the velocity magnitude at the bottom of the wave tank. If the the velocity magnitude is small compared to velocity magnitude in free surface, it means the mesh can be coarsened up in this region. In any case its best to avoid any abrupt transition from very fine mesh to very coarse mesh.

- Bridge region: This region overlaps with free surface region. It includes both water and air. The mesh size in this region is very critical because it greatly influences the simulation results. As it will be shown in next chapter the mesh size in this region is important in all three dimensions.

It is appropriate to show mesh size and time step as a fraction of wave length λ and wave period T_p . In these experiments the biggest wave had the wave height of $H=0.84\text{m}$ and wave length of $\lambda = 9.4\text{m}$. This means mesh sizes tried in bridge region ranged from $\lambda/1300$ to $\lambda/652$ and mesh sizes tried in free surface region ranged from $\lambda/390$ to $\lambda/195$. The total number of mesh used in simulation domain ranged from 358,659 cells for 2D model to 11,483,096 in 3D model.

Time step also greatly influences simulation results. The effect of time step on simulation results is shown in figure 5.21 and 5.22 for $H=0.84\text{m}$, $T_p=2.5\text{s}$. Time steps tried are $dt=0.02\text{s}$ and $dt=0.004\text{s}$ which are used with mesh configuration in Test #2 shown in table 5.3. They are equivalent to $T_p/250$, and $T_p/625$ respectively. As it is clear from these figures, time step size has significant effect on force time history for both horizontal and vertical forces. Using a big time step not only cause difference in peak magnitude of forces but also causes phase lag. As it is seen in simulation results for $dt=0.02\text{s}$, the force time history period changes after few interaction between bridge superstructure and upcoming waves. In addition looking into figure 5.21 for horizontal force, it is evident that when $dt=0.02\text{s}$ is used the wave loses its energy as it interacts with the bridge superstructure. This is because of excessive damping and dissipation that happens in the bridge region because the time step used in simulation is not sufficiently small. In addition simulation results for $dt=0.004\text{s}$ contain more high frequency content than simulation results for $dt=0.02\text{s}$ for both horizontal and vertical forces.

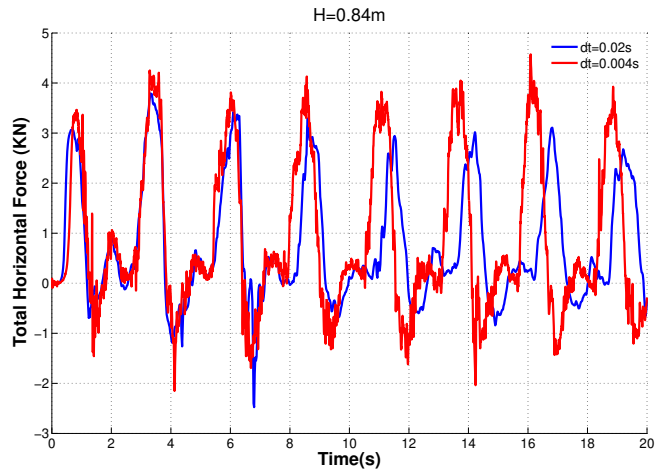


Figure 5.21: Effect of time step choice on total horizontal wave forces for $dt=0.02s$ and $dt=0.004s$

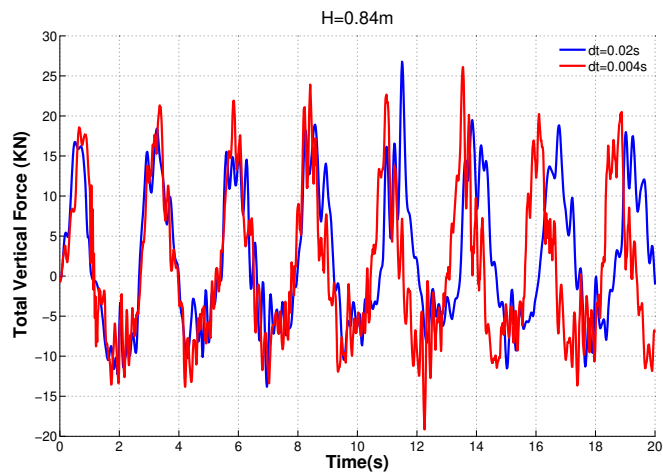


Figure 5.22: Effect of time step choice on total vertical wave forces for $dt=0.02s$ and $dt=0.004s$

Combined effect of mesh size and time step can be seen in Courant number. In all the simulations Courant number at free surface is monitored. While implicit schemes are not as sensitive to Courant number as explicit schemes, High Resolution Surface

Capturing Scheme (HRIC) which is used to capture free surface is sensitive to Courant number value. Therefore The surface average of convective courant number on free surface in most simulations is kept bellow 0.4. Figure 5.23 shows the Courant number for wave height $H=0.84\text{m}$ in Test #6.

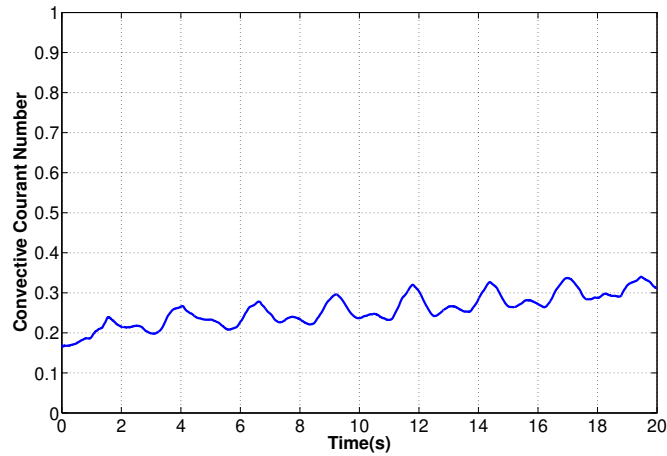


Figure 5.23: Convective Courant Number for Test #6

In addition, as a general rule in experiment, In order to resolve the measured data signals, the sampling on all instrumentation needed to be at least twice the highest expected forcing frequency of interest, in this case slamming frequency. The sampling frequency used in experiments conducted in wave loading on bridge deck experiment conducted at Oregon State University was 250 Hz, which was capable of resolving frequencies up to 125 Hz. As a results to somehow match the experiment sensitivity, time step size required to capture slamming force correctly needs to be smaller equal or smaller than $dt=0.004\text{s}$ or $T_p/625$ which is what was used in Test #2, Test #5 and Test #6.

5.7 Solution Convergence

The numerical method explained in chapter 3, requires an iterative process in order to obtain a solution. After each iteration, residuals are produced that indicate how well the governing equations for each solver quantity are being satisfied numerically. Residuals are used as one of the means to judge solution convergence. In STAR-CCM+ they are created automatically. While its true that residuals tend to decrease to a small number when solution is converged, the residual monitor alone, can not be relied on as the only measure of convergence because the amount of decrease in residual depends on the simulation. For example initial guess strongly influences the amount that residuals decrease. If the initial guess satisfies the discretized equations perfectly, the residuals will not drop at all. Also, residual plot in STAR-CCM+ is for the whole simulation domain. In some cases because of poor mesh quality, dispersive errors may result in oscillation in small number of cells which is out side the domain of our interest. In this case the residual plot will show that the solution is not converged while the quantities of interest inside our domain of interest is fully converged. Finally, residuals do not necessarily relate to quantities of engineering interest in the simulation such as integrated forces (CD-adapco (2010)).

As a result in addition to the default residual plots in STAR-CCM+, we define two additional engineering monitors for horizontal and vertical forces for each iteration. Figure 5.24 shows an example of residual plot for the whole simulation domain for continuity and momentum equation.

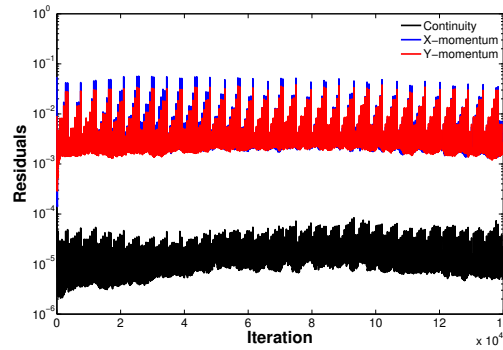


Figure 5.24: Residuals for continuity and momentum equations

In STAR-CCM+ it is possible to create stopping criteria based on existing monitors. This lets us use more meaningful criteria to judge convergence. These monitor-based stopping criteria could include a reduction in a residual, or could be based upon some physical quantity that we are interested in obtaining from the solution. In these simulation two stopping criteria is used. A stopping criteria is used to make sure the residuals for momentum in major directions are reduced at least 2 orders of magnitude. In addition asymptotic criteria is used to make sure forces reached asymptotic limit at each time step before going to next time step. To achieve this we have to prescribe the maximum change in the force that we consider is sufficient for convergence within certain number of iteration. This limit is determined by calculating the smallest force possible to calculate in simulation. This limit in this simulation is equal to the smallest buoyancy force which is applied to the bridge superstructure and is calculated as follows:

$$\text{Asymptotic limit} = \gamma_w(\text{volume of bridge submerged} \times \text{one cell thickness}) \quad (5.2)$$

$$\begin{aligned} \text{Asymptotic limit} = & (9.8 \text{ kN/m}^3) \times (6 \text{ Girder}) \times \left(\underbrace{0.09\text{m}}_{\text{Girder length}} \right) \times \\ & \left(\underbrace{3.45\text{m}}_{\text{Girder width}} \right) \times \left(\underbrace{0.0072\text{m}}_{\text{One cell thickness}} \right) = 0.131 \text{ kN} \end{aligned}$$

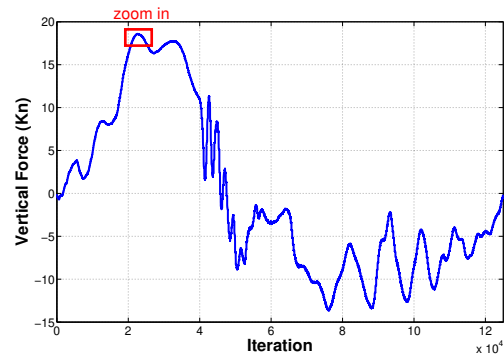


Figure 5.25: Convergence in several time steps

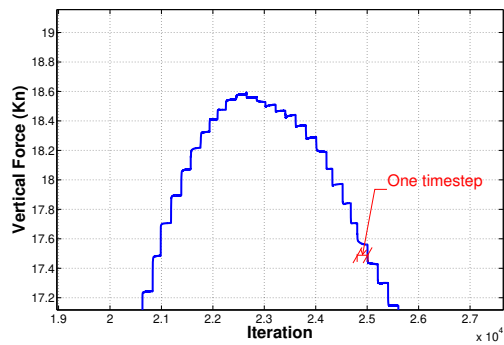


Figure 5.26: Convergence in one time step

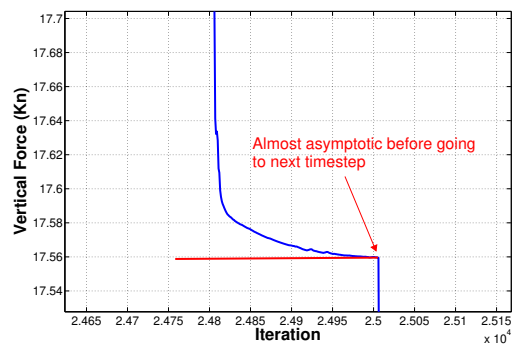


Figure 5.27: Vertical force reaching asymptotic limit in one time step before going to next time step

Figure 5.24 shows vertical force time history in respect to the number of iterations. Figure 5.25 shows how the solution converges at each time step before going to the next time step. Figure 5.26 shows that vertical force time history becomes almost asymptotic in one time step before going to the next time step.

5.8 Spectral Analysis

For all simulations and all test cases, power spectra were computed for total vertical and horizontal forces. In all cases the frequency with the highest power content was that of the wave frequency. There is some energy present in the harmonic multiples of the wave frequency. This is consistent with the experimental results from wave loading on bridge decks (Sheppard and Marin (2009)) and large scale laboratory observations of wave forces on highway bridge superstructure (Bradner and Cox (2008)). Figure 5.28 and 5.29 show the power spectra for $H=0.84\text{m}$ in Test #6 for the total horizontal and vertical force time history respectively.

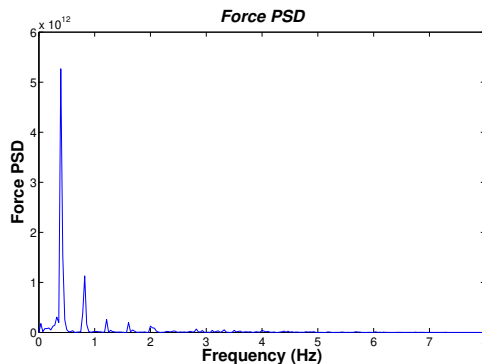


Figure 5.28: Horizontal force power spectral density

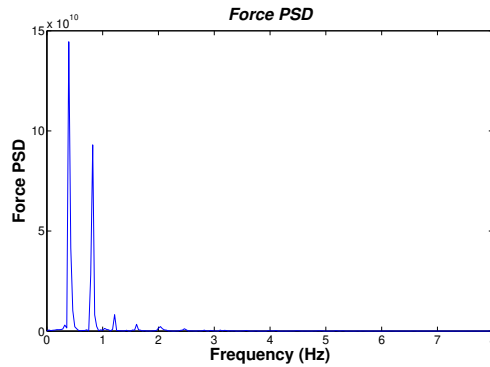


Figure 5.29: Vertical force power spectral density

5.9 Slamming Force and Structural Response

The cavities under bridge superstructure trap air and cause slamming oscillations as seen in experimental data from University of Florida(Sheppard and Marin (2009)). According to observations in experiments conducted at University of Florida (Sheppard and Marin (2009)) The number of slamming oscillations in the total vertical force time history is the number of air cavities under bridge superstructure (number of girders minus one) as shown in the sketch in Figure 5.30

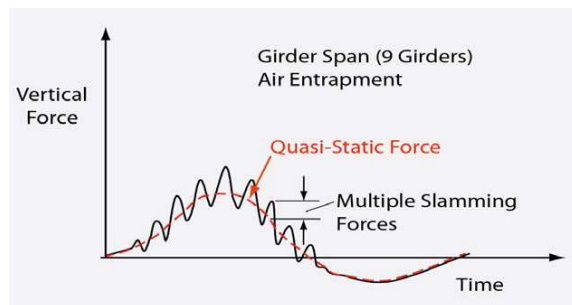


Figure 5.30: Typical vertical wave force versus time plot for a subaerial structure with girders adapted from (FDOT (2008)).

Slamming oscillations existed in experimental data from University of Florida but were not present in experimental data from Oregon State University. As it will be shown in chapter 6, the existence of slamming force and its magnitude is directly related to the amount of entrapped air under the bridge and the sensitiveness of experimental setup for capturing high frequency slamming oscillations in vertical force time histories. In experiments conducted at Oregon State University, what load sensors registered was related to structural response. However, what CFD calculates as total force is the integration of pressure around the boundary of the bridge superstructure. While these two are closely related, they are not exactly the same. Consider the spring, mass, dashpot system shown in figure 5.31. The response of this simple, one degree of freedom system is described by the differential equation 5.3, where z is the displacement, m is the object mass, c is the damping coefficient, k is the spring constant, and $F(t)$ is the time dependent forcing.

$$F(t) = m \frac{d^2 z}{dt^2} + cm \frac{dz}{dt} + kz \quad (5.3)$$

The response of system depends on three important frequencies: forcing frequency ω , natural frequency ω_n and the systems damped frequency ω_d . The expressions for natural frequency and damped frequency are shown in equations 5.4 and 5.5.

$$\omega_n = \sqrt{\frac{k}{m}} \quad (5.4)$$

$$\omega_d = \omega_n \sqrt{1 - \left(\frac{c}{2m\omega_n}\right)^2} \quad (5.5)$$

The structure's response as a function of damping magnitude and ratio of forcing to natural frequency is shown in figure 5.32. From this figure, it is evident that the structure only responds to frequencies close to its natural frequency. As a result, simulation results containing frequencies much higher than experimental setup's natural frequency are not

directly comparable to experimental data available from Oregon State University since the bridge structure, because of its heavy mass did not respond to the high frequency excitation which was caused by some wave heights as a result of air entrapment. Hence, in order to remove high frequency content from simulation results, the simulation results are filtered with 8th order low pass butter filter with a cutoff frequency of 7 Hz. The 7 Hz frequency is chosen based on the highest frequency witnessed in load cell experimental data available from Oregon State University (Bradner and Cox (2008)). In addition according to Bradner and Cox (2008) the model bridge superstructure which was built in Oregon State University had natural frequency of 2.22 Hz which gives the ratio of forcing frequency to natural frequency of $7/2.2=3.15$. Looking into figure 5.32 we see that it is highly unlikely for the bridge superstructure to respond to frequency ratios over 3.

The filtered simulation result is called quasi-steady force. The slamming force is determined by subtracting filtered force from original (raw force) time history simulation results. Figure 5.31 shows an example of filtered force signal for one of the simulation test cases showing quasi-steady and slamming forces.

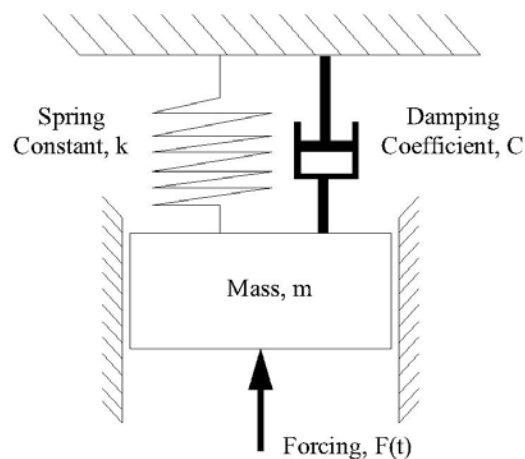


Figure 5.31: Spring-mass-dashpot system

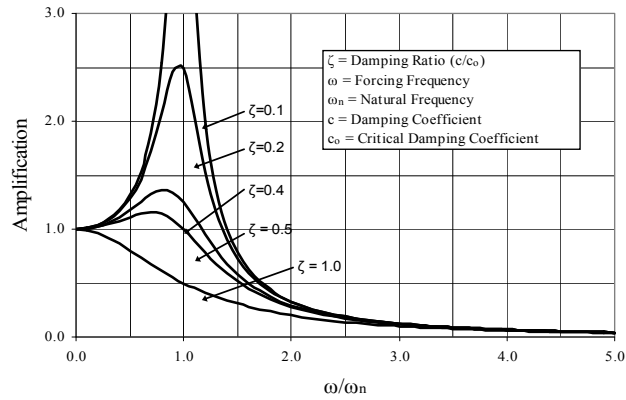


Figure 5.32: Amplitude amplification as a function of forcing frequency and damping

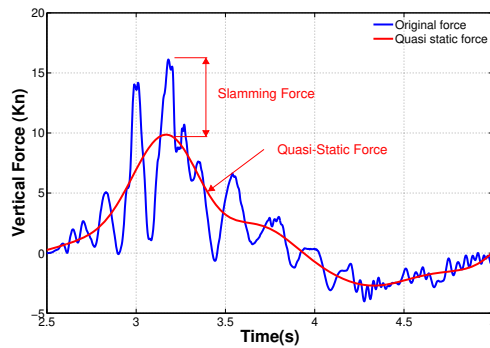


Figure 5.33: Example of filtered and unfiltered vertical force for a subaerial slab.

In all test cases in chapter 6, where comparison to experimental data is made, both horizontal and vertical forces are filtered. In general filtering did not influence horizontal force time histories in any of the test cases because in none of the test cases mentioned in table 5.3 the horizontal force time history contained frequencies over 7 Hz. This is consistent with observations in experimental data from Oregon State University. As it is seen in figure 5.35 the low pass filter influenced vertical force time histories of certain wave heights such as $H=0.34\text{m}$ and $H=0.43\text{m}$. These are the time histories which contain frequencies over 7Hz. Other wave heights simulated did not show much slamming

oscillation. Filtered and unfiltered horizontal and vertical force time histories for Test #6 are shown in figure 5.34 and 5.35.

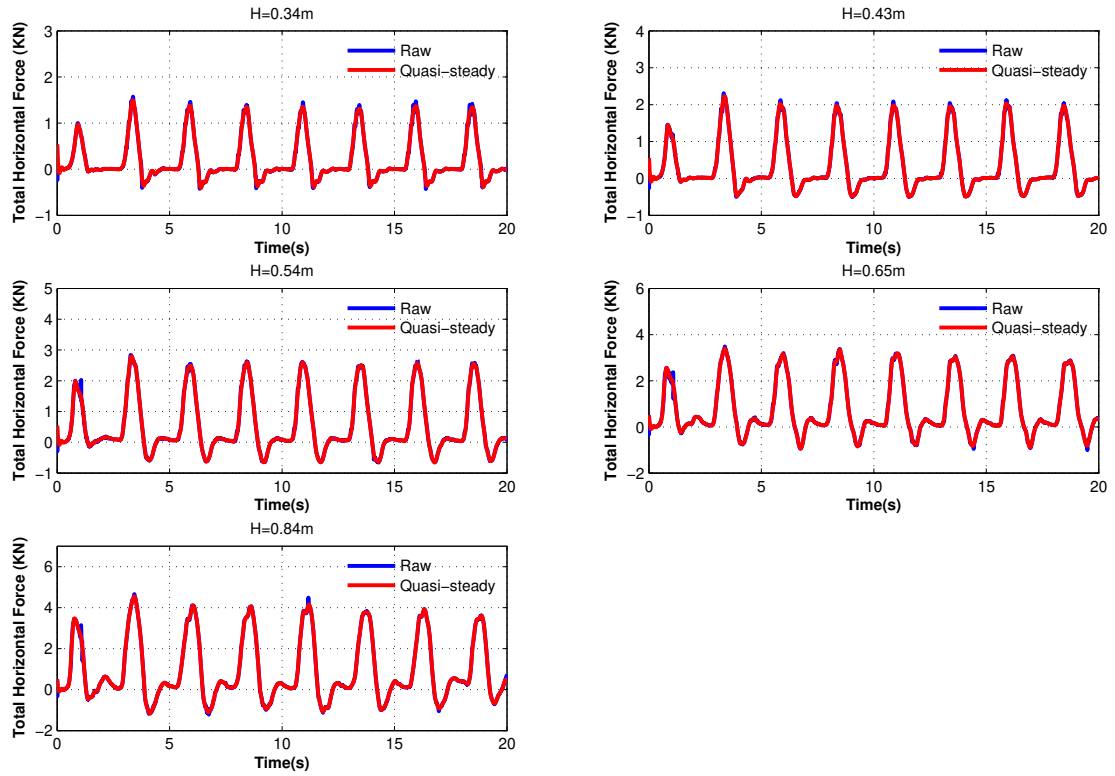


Figure 5.34: Quasi steady vs. raw horizontal wave forces

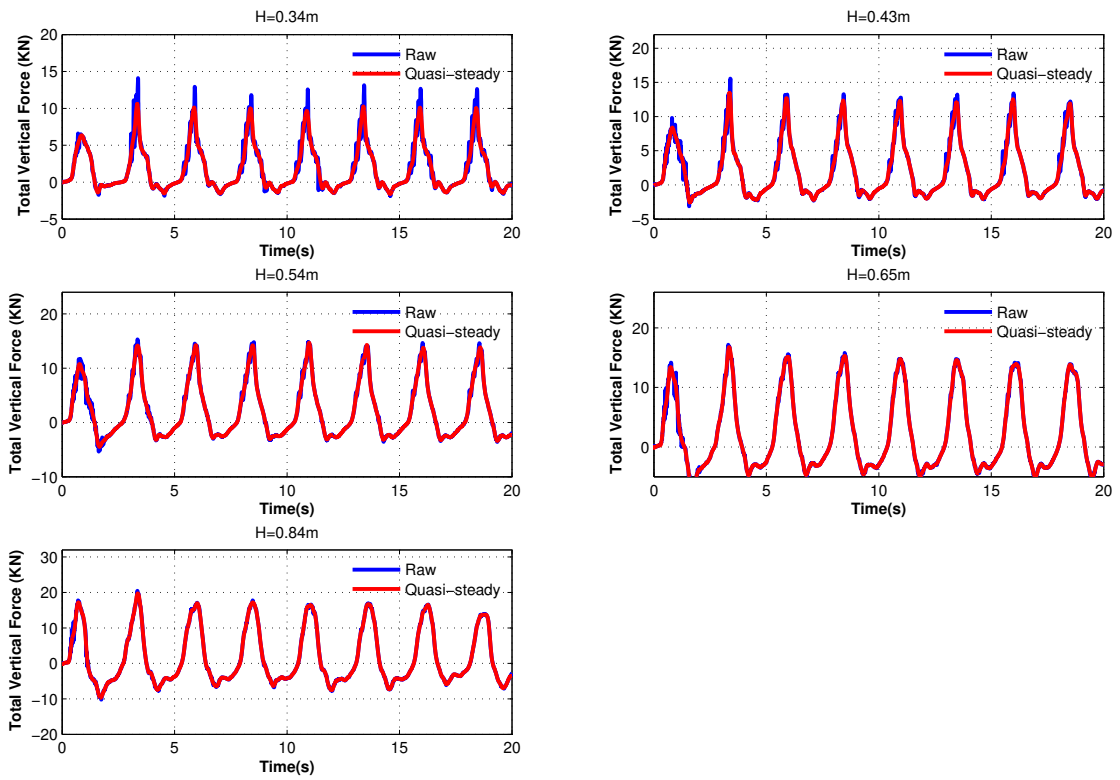


Figure 5.35: Quasi steady vs. raw vertical wave forces

Chapter 6

NUMERICAL RESULTS FOR LARGE SCALE WAVE BRIDGE INTERACTION

In this section 2D and 3D model simulation results are compared with experimental data available from Oregon State University. The experimental setup, mesh configuration, and modeling physics used in these simulations are discussed in chapter 5.

6.1 2D Model

Three 2D test cases are investigated for waves ranging from $H=0.34\text{m}$ to $H=0.84\text{m}$ with wave period of $T=2.5\text{s}$ and water depth at $d=1.89\text{m}$ was kept constant at all simulations. Investigated mesh sizes and time steps are presented in table 6.1. Since the full time history of wave bridge interaction was not available from Oregon State University as explained in chapter 5, the average of the peak of the forces in simulation were compared to the average of peak of the forces in experiment for 20s of wave-bridge interaction. From this point onward when we talk about horizontal and vertical forces we mean the average of the peak of the total horizontal and vertical forces applied to bridge superstructure. In 2D model the mesh used in horizontal and vertical direction (x and z direction) are the same size (the main directions are shown in figure (5.19)). In table 6.1 the size of mesh used in x and z direction is shown by Δx . In CFD modeling

| Test | Model | $\Delta t(s)$ | Mesh size (cm) | | | | | | Total # of cells |
|------|----------------------|---------------|----------------|------------|--------------|------------|------------|------------|------------------|
| | | | Bridge | | Free surface | | Deep water | | |
| | | | Δx | Δy | Δx | Δy | Δx | Δy | |
| 1 | 2D | 0.02 | 0.72 | N/A | 2.4 | N/A | 4.8 | N/A | 733,537 |
| 2 | 2D | 0.004 | 1.44 | N/A | 2.4 | N/A | 4.8 | N/A | 358,659 |
| 3 | 2D (pressure outlet) | 0.02 | 1.44 | N/A | 2.4 | N/A | 4.8 | N/A | 358,659 |

Table 6.1: Different mesh sizes and time steps investigated in 2D model

of wave propagation, it is possible to use a different size mesh in x and z direction. In general since z direction is more critical in free surface wave modeling, the mesh in z direction can be refined to lessen excessive wave energy dissipation and save on computational time. However in problem of wave interacting with bridge superstructure, we noticed abnormal elongation of wave as it hit the bridge when the bigger mesh size was used in x direction. To avoid this problem, In all simulation cases the mesh used in x and z direction are the same size and they are simply shown by Δx .

6.1.1 Simulation Results for Test #1

In Test #1 the time step used is $dt=0.02s$ which is equivalent to $T_p/125$. Horizontal force time history for $H=0.34m$ to $H=0.84m$ is shown in Figure 6.1. In Figure 6.1 the blue graph is simulated horizontal force time history, the discrete blue horizontal line is the average of peak of the forces in simulation, and the discrete black horizontal line is the average of peak of the forces in experiment. As it is seen in figure 6.1, for all wave heights, simulation under predicts the horizontal force. As the wave height increase, the magnitude of error also increase. The maximum error in horizontal force predictions happens for wave height of $H=0.84m$ and is 48 percent. The vertical force time history is shown in figure 6.2. As it is seen in figure 6.2 simulation over predicts the magnitude of vertical forces for $H=0.34m$, $H=0.43m$ and $H=0.54m$ and under predicts the magnitude of vertical forces for $H=0.65$ and $H=0.84m$. For $H=0.34m$, simulation

over predicts the magnitude of vertical forces by 20 percent. For $H=0.84\text{m}$, the simulation under predicts the magnitude of vertical forces by 18 percent. Figure 6.3 shows the comparison between the average of peak of the forces in experiment and average of the peak of the forces in simulation for both horizontal and vertical forces applied to bridge superstructure.

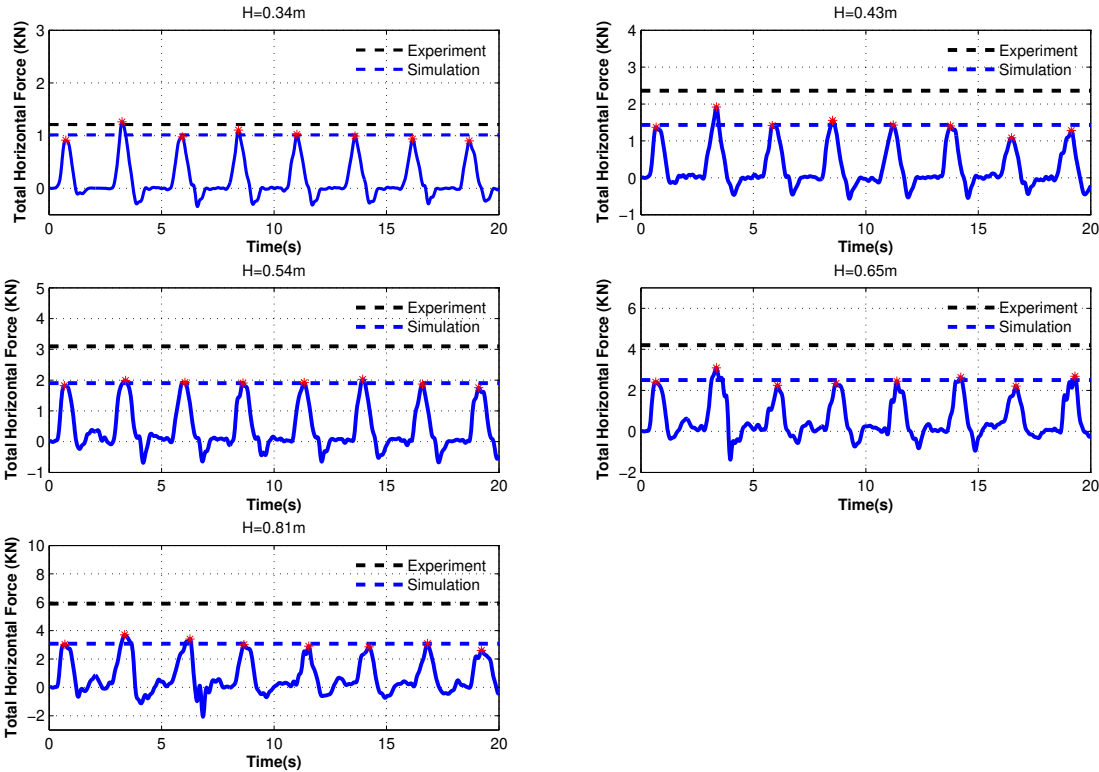


Figure 6.1: Horizontal force simulation results for Test #1

In this figure, hollow spheres are experimental data and the solid spheres are simulation results. In figure 6.3 the horizontal error bar is the range of wave heights produced by the wave maker. The vertical error bar represents the range of forces measured by load sensor for the range of wave heights measured. The behavior of simulation force time history is different in horizontal and vertical force time histories.

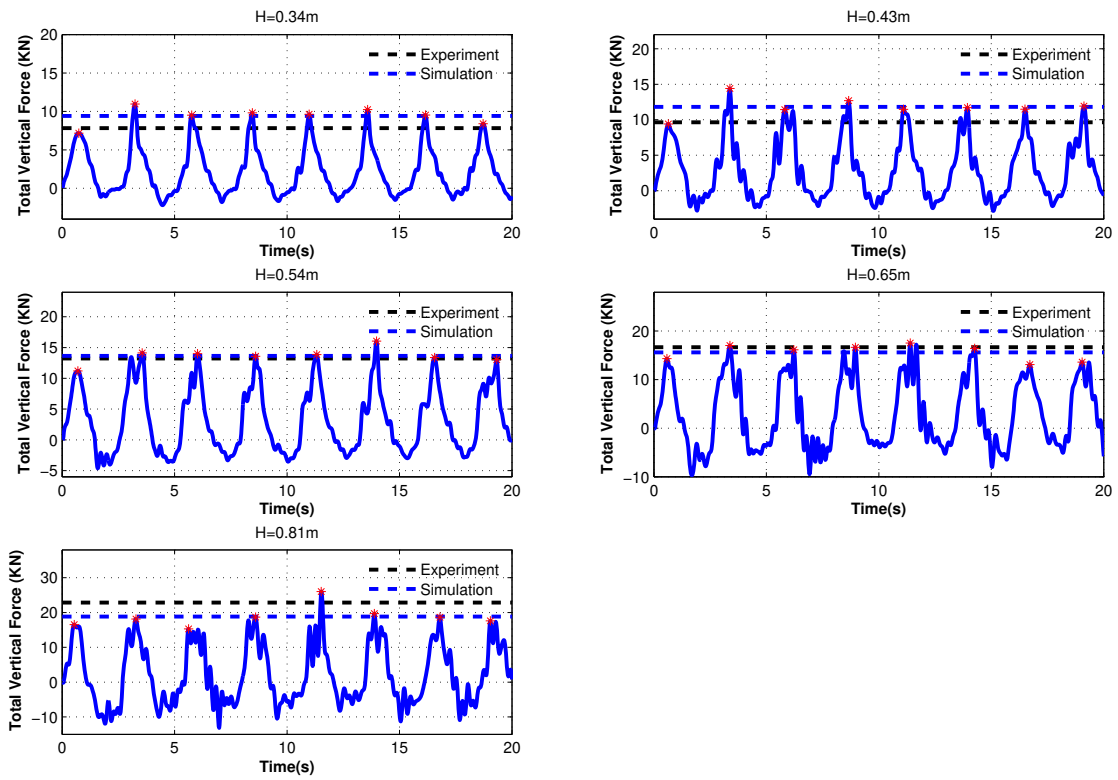


Figure 6.2: Vertical force simulation results for Test #1

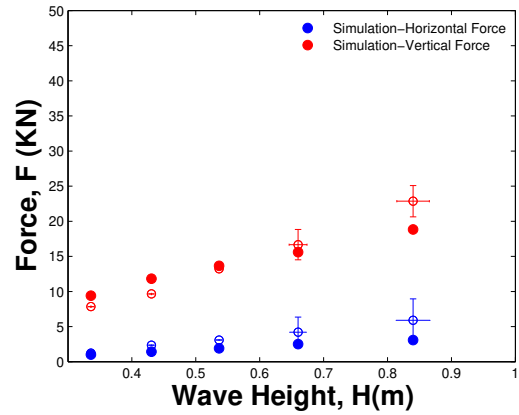


Figure 6.3: Comparison of horizontal and vertical simulation wave forces for Test #1 to experimental data

The horizontal simulation force time history is smooth with minimal oscillation. The vertical force time history shows some oscillation as the wave height increase.

6.1.2 Simulation Results for Test #2

In Test #2 in order to improve the simulation accuracy, time step size is reduced to $dt=0.004s$ which is equivalent to $T_p/625$ and mesh size in bridge region increased to twice the value that was used in Test #1 (to save computational time). Horizontal force time history for $H=0.34m$ to $H=0.84m$ is shown in Figure 6.4.

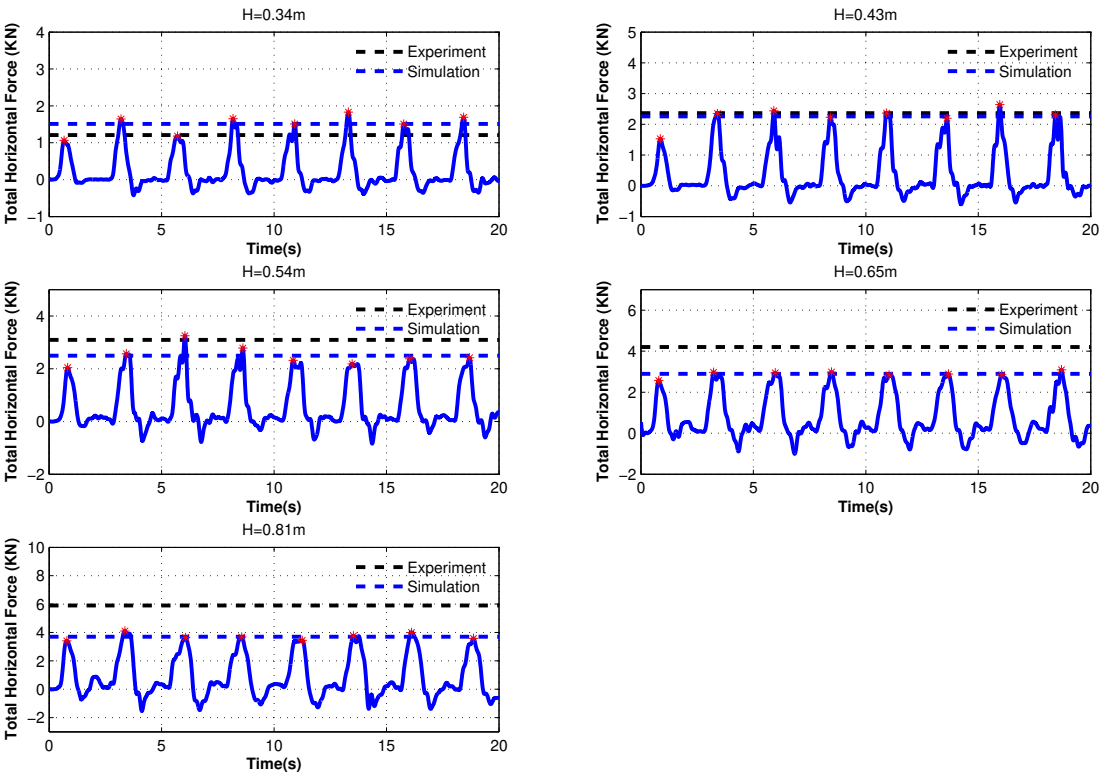


Figure 6.4: Horizontal force simulation results for Test #2

The simulation over predicts the average of the peak of the horizontal forces for $H=0.34\text{m}$ while it under predicts the average of the peak of horizontal forces for the rest of wave heights. The maximum error in horizontal force again happens for the biggest wave height $H=0.84\text{m}$ which is 37 percent. Comparing to Test #1, the maximum error in horizontal wave forces reduced by 11 percent. The vertical wave force time history for Test #2 is shown in figure 6.5. Comparing to Test #1 vertical forces, vertical force time history in Test #2 shows a highly oscillatory behavior that is not seen in Test #1. As the wave height increase, the oscillatory behavior in vertical force time history decrease. Vertical force time history in Test #2 does not compare well with experimental data. Highly oscillatory behavior that is seen in wave heights of $H=0.34\text{m}$, $H=0.43\text{m}$ and $H=0.54\text{m}$ cause large errors in vertical force predictions. Simulation over predicts the magnitude of vertical force for $H=0.34\text{m}$ by as much as 93 percent. Test #2 simulation under predicts the magnitude of vertical force for $H=0.84\text{m}$ by 6 percent. This means even though comparing to Test #1, the maximum error in horizontal forces reduced by 11 percent, the maximum error in vertical force predictions increased from 23 percent to 93 percent.

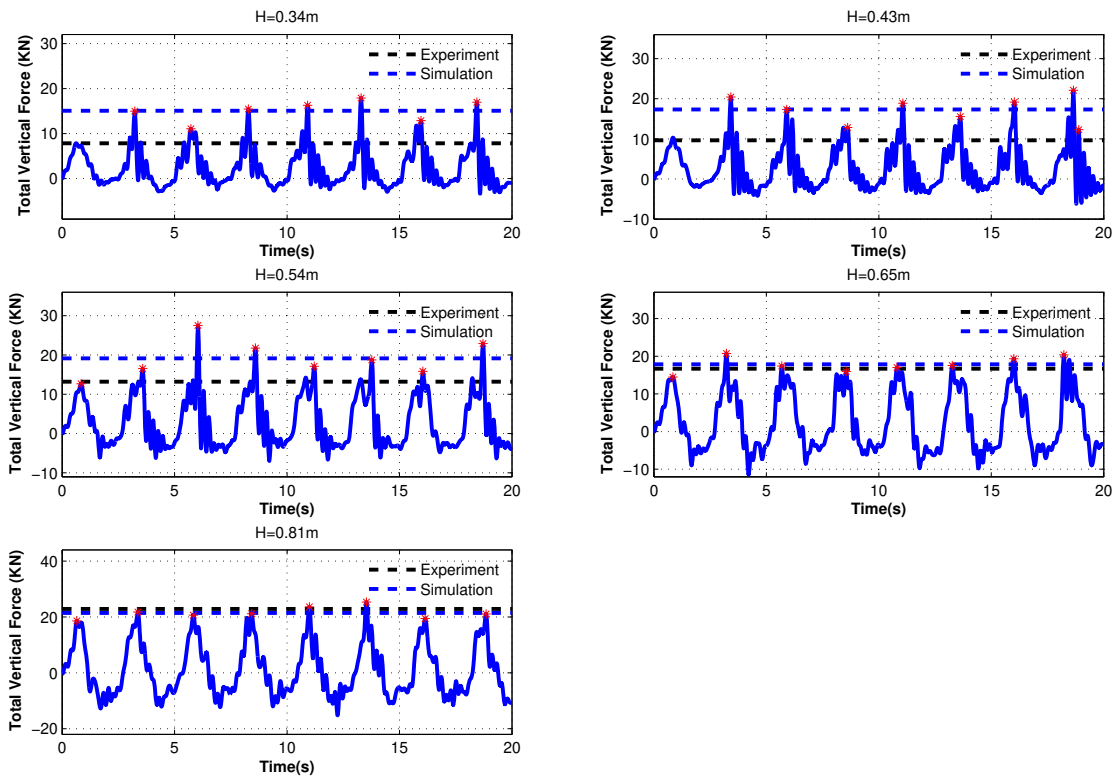


Figure 6.5: Vertical force simulation results for Test #2

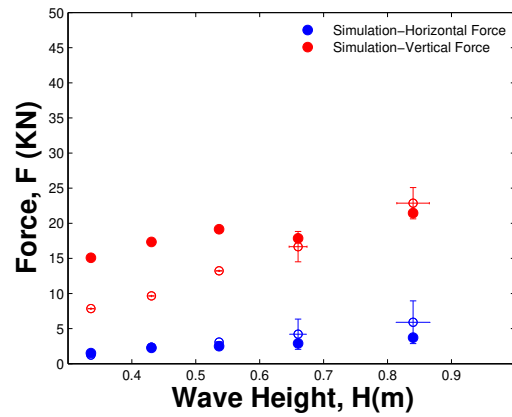


Figure 6.6: Comparison of horizontal and vertical simulation wave forces for Test #2 to experimental data

Some simulation scenes showing wave interacting with bridge deck for Test #2 is shown for $H=0.84\text{m}$ in figures 6.7 to 6.11. In the following figures: figure 6.7 shows volume of fluid scene. In this figure red represents water and blue represents air and all the colors in between represent mixture of air and water. Figure 6.7 shows that as wave hits the bridge overtops it and part of it reflects back from the bridge and mixes up with the upcoming wave. It is also evident in figure 6.7 that significant amount of air gets trapped under the bridge deck inside the space between bridge girders because as we see the water does not progress into the cavities under the bridge superstructure. This is mainly due to the symmetry boundary used on the side of 2D simulation domain which does not allow any air to exit from side of simulation domain. Figure 6.8 shows the pressure distribution inside simulation domain. In majority of simulation domain the pressure at the bottom of simulation domain is hydrostatic pressure. As the wave move from left to right the pressure at the bottom of simulation domain directly under the wave increase because of added pressure due to increase in water elevation and also because of added dynamic pressure due to increase in vertical water particle velocity. In Figure 6.9 velocity vectors are shown inside simulation domain. As it is seen the magnitude of velocity vector is maximum around the wave crest and is minimum around bottom of simulation domain. That is why the mesh need to be fine in free surface region and can be coarsened up close to bottom of simulation domain. Also because the interaction of wave-bridge is very complex, extra refinement is required around bridge region. This is evident by looking at figure 6.9. Figure 6.10 and 6.11 show horizontal and vertical velocity magnitude contours. Before wave hits the bridge figure 6.10 shows that the maximum horizontal velocity happens in wave crest while figure 6.11 shows that maximum vertical velocity (positive and negative) happens around bridge trough. As the simulation go on the reflected wave from bridge interacts with the wave coming from the inlet and the effect of reflected wave propagates upstream toward the inlet

boundary inside simulation domain. The distance between bridge and inlet and outlet boundary need to be sufficiently large so that the reflected wave and the wave that has passed the bridge do not reach these two boundaries during 20s of simulation time.

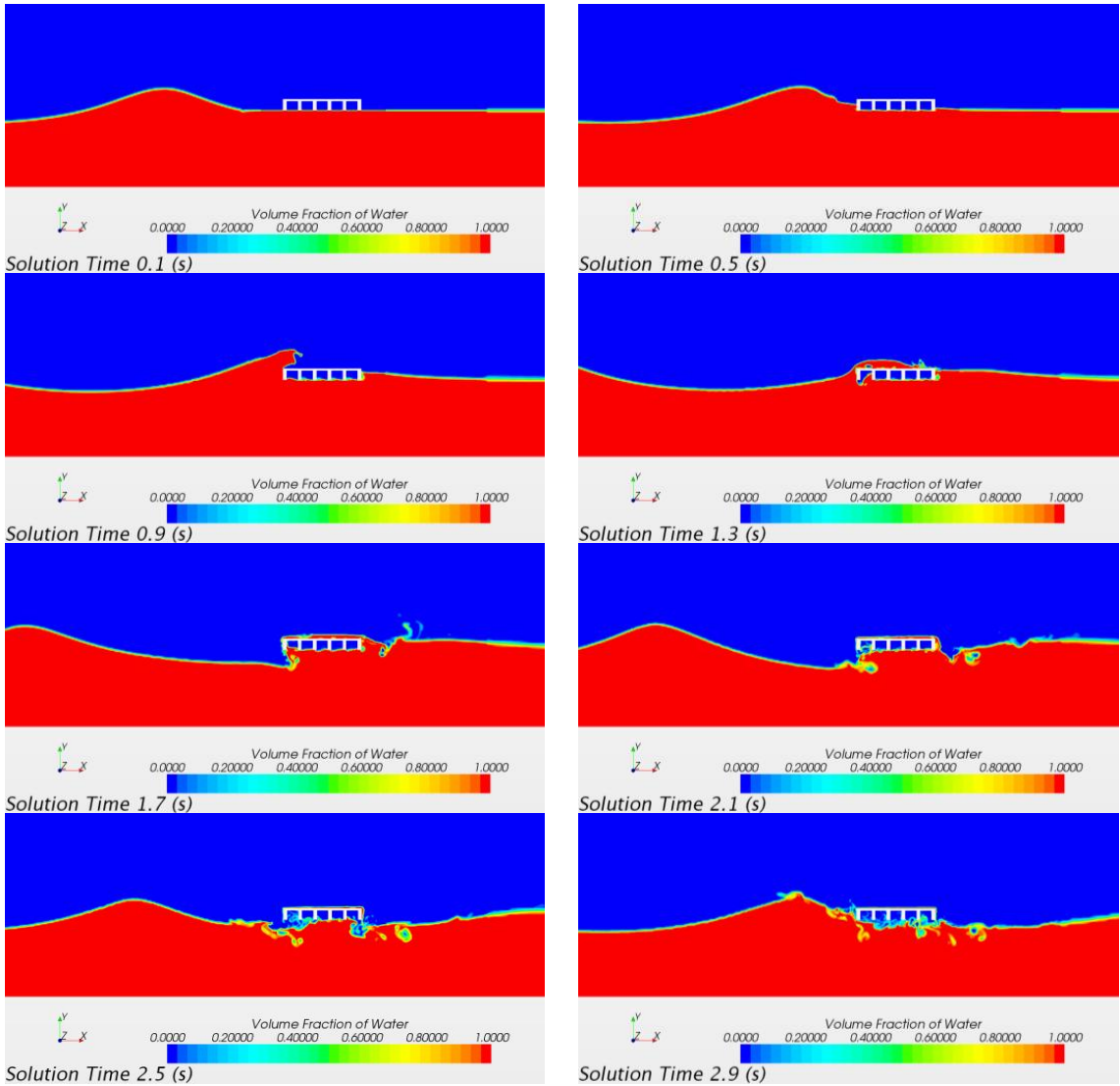


Figure 6.7: Volume of fluid (VOF) scene for $H=0.84\text{m}$ (Test #2)

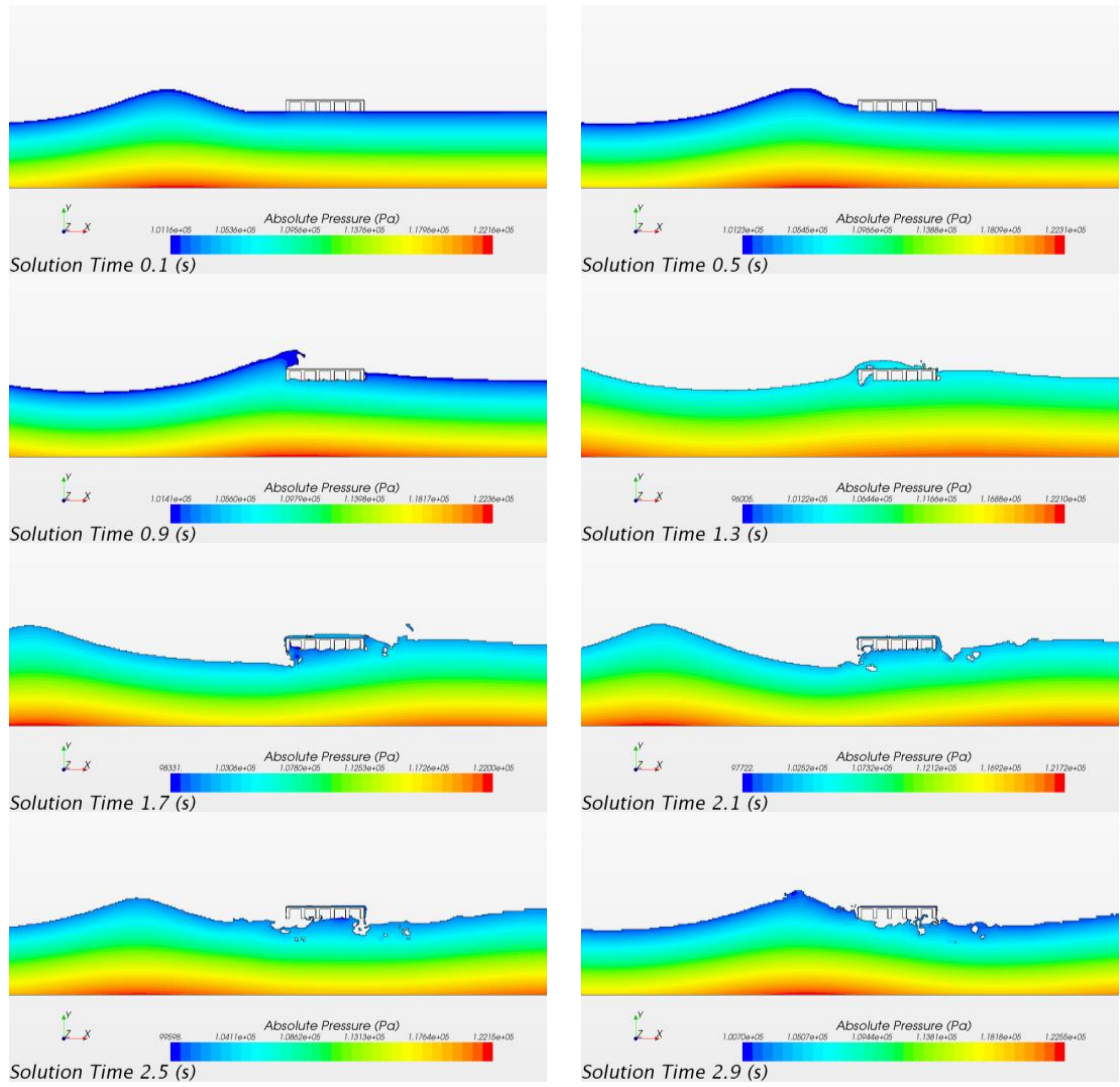


Figure 6.8: Absolute pressure scene for $H=0.84\text{m}$ (Test #2)

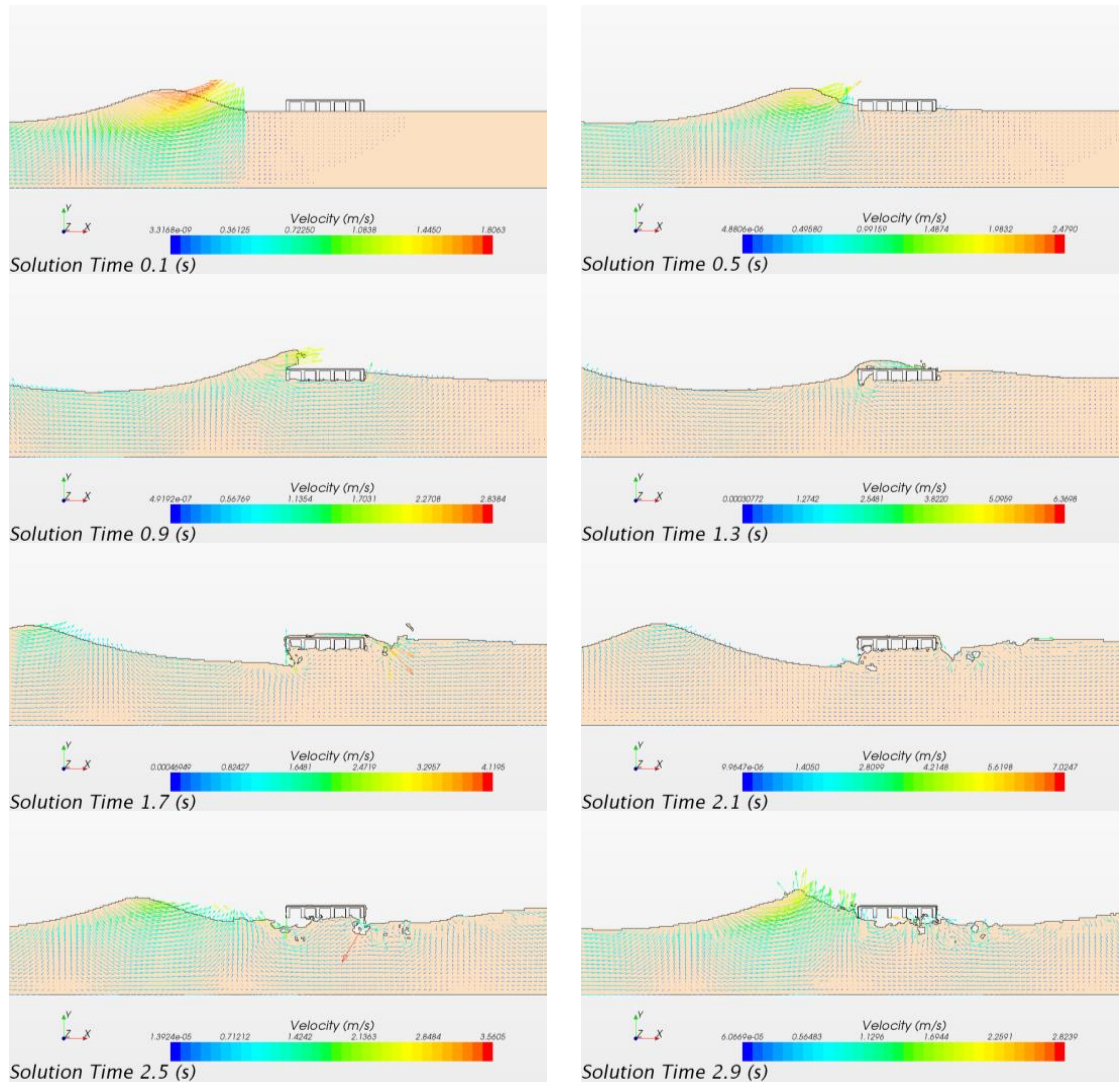


Figure 6.9: Velocity vector scene for H=0.84m (Test #2)

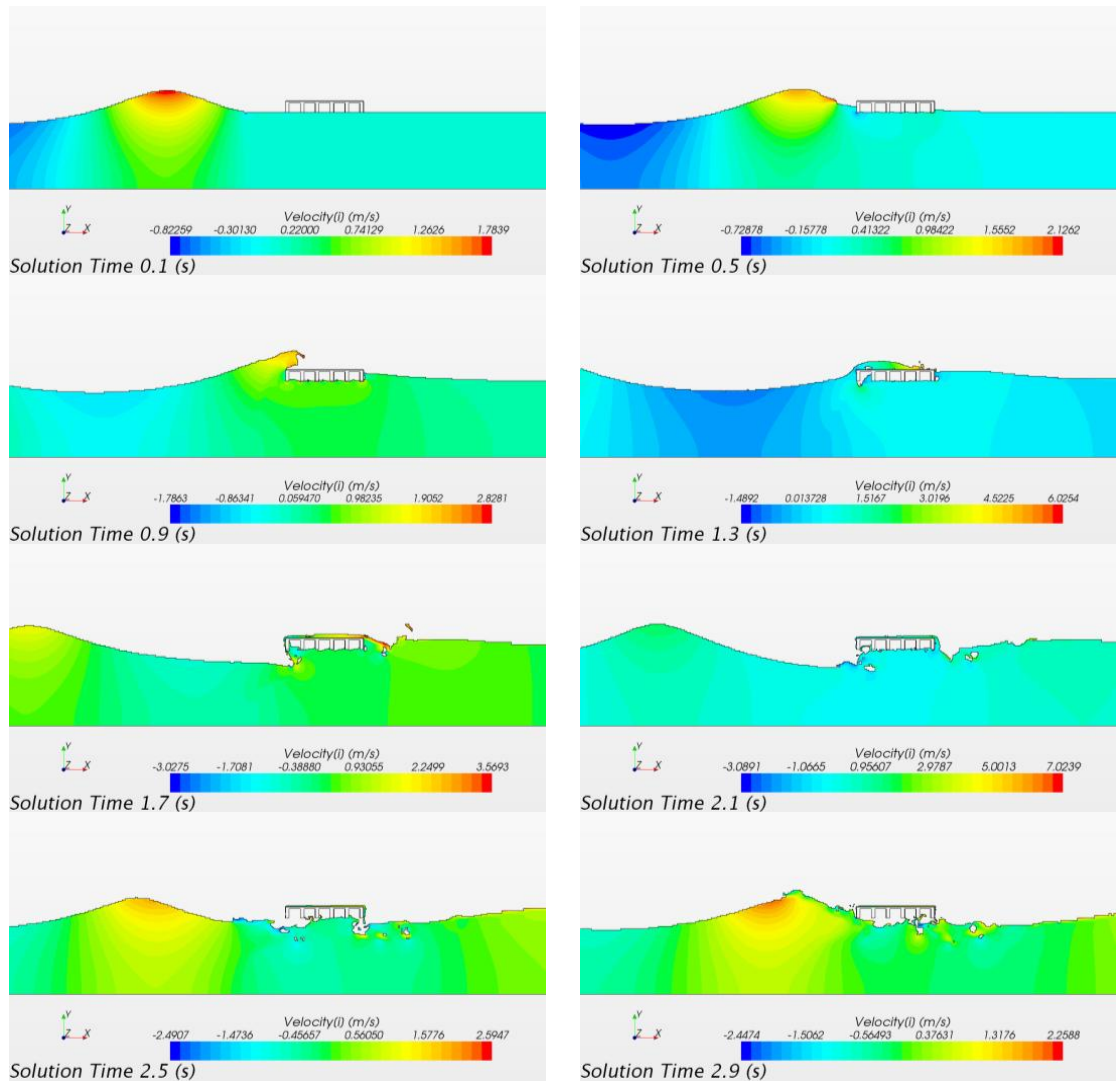


Figure 6.10: Velocity magnitude in horizontal direction for $H=0.84\text{m}$ (Test #2)

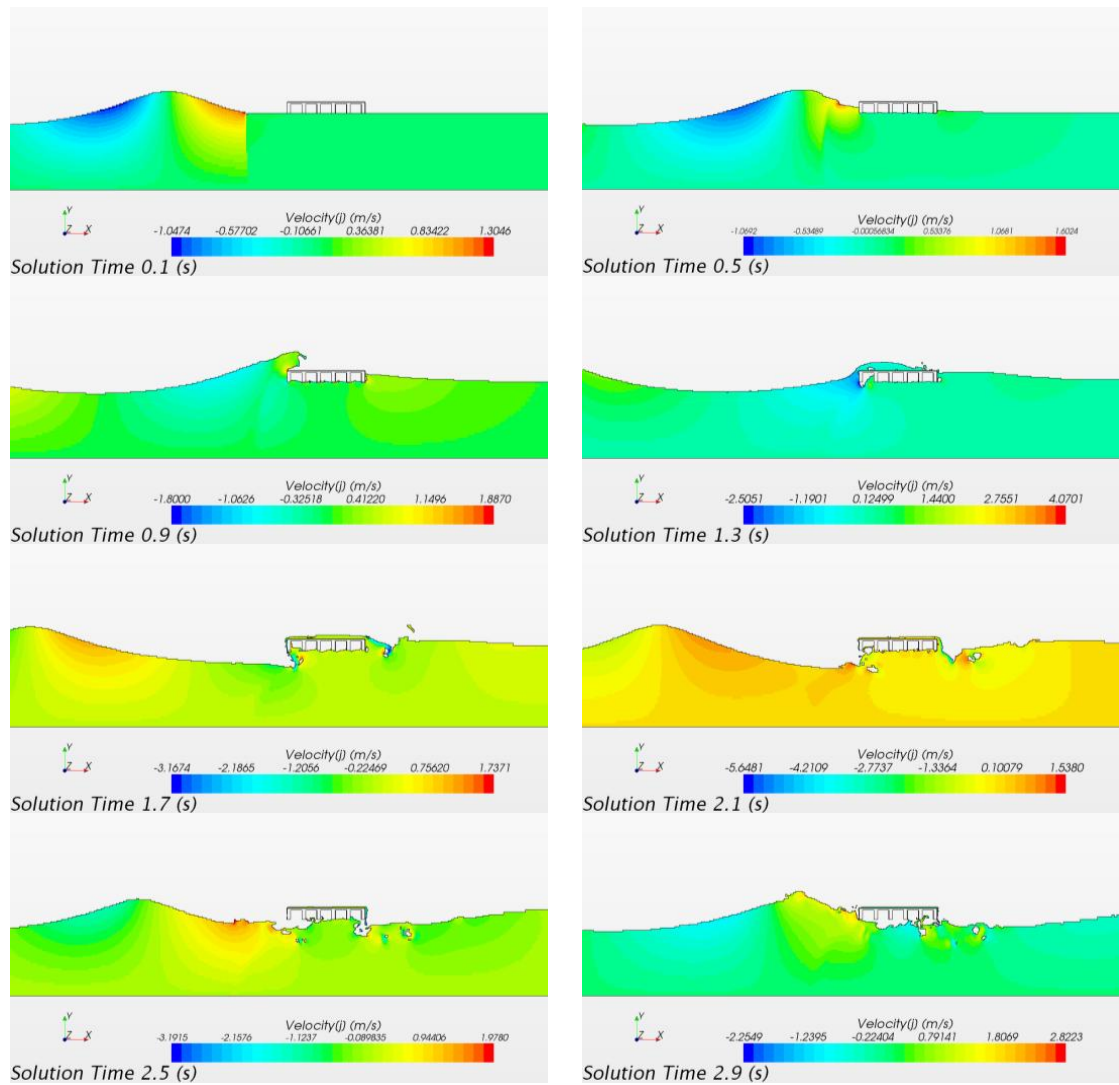


Figure 6.11: Velocity magnitude in vertical direction for $H=0.84\text{m}$ (Test #2)

6.1.3 Simulation Results for Test #3

In Test #2 it was shown that reducing time step from $dt=0.02\text{s}$ to $dt=0.004\text{s}$ caused a highly oscillatory behavior in vertical force time history for some wave heights. Test #3 is designed to investigate the reason behind the oscillatory behavior that was seen in

vertical force time history as time step was reduced. According to the report from university of Florida, air entrapment between bridge girders and diaphragms cause oscillatory behavior (Sheppard and Marin (2009)). How ever this was not verified because the experimented bridge was made airtight and no experiment was conducted to validate the theory of air entrapment causing oscillatory behavior in vertical force time histories. The oscillatory behavior was seen in simulation time histories of vertical forces of Test #1 but it was amplified as time step reduced to $T_p/625$ in Test #2.

To confirm this theory, in Test #3, the symmetry plane boundary condition at the side of simulation domain is replaced by pressure outlet. Pressure outlet boundary will allow both air and water to exit from the side of simulation domain. This is not a realistic boundary condition how ever it will allow us to investigate how entrapment of air influence the shape of both horizontal and vertical force time histories. Simulation results are plotted in figures 6.12, 6.13, and 6.14. As it is seen both horizontal and vertical force time history for Test #3 do not show any oscillatory behavior. In addition since the water and the air both can exit from simulation domain from the side, there is not that much wave reflection from bridge because the water simply exists the side of simulation domain instead of reflecting back from bridge. This is shown in figure 6.15. Comparing to Test #1 which had the same time step as Test #3, it is interesting to note that allowing both the air and water to move out of simulation domain from the side, does not seem to increase error in horizontal force predictions. In fact, the maximum error in horizontal force prediction reduced from 48 percent in Test #1 to 19 percent in Test #3. This shows that horizontal wave force time histories are not influenced by air entrapment. It also shows that in Test #1 and Test #2 models excessive air entrapment happens because when the air is allowed to fully vent out from the side of simulation domain, horizontal force prediction accuracy became better.

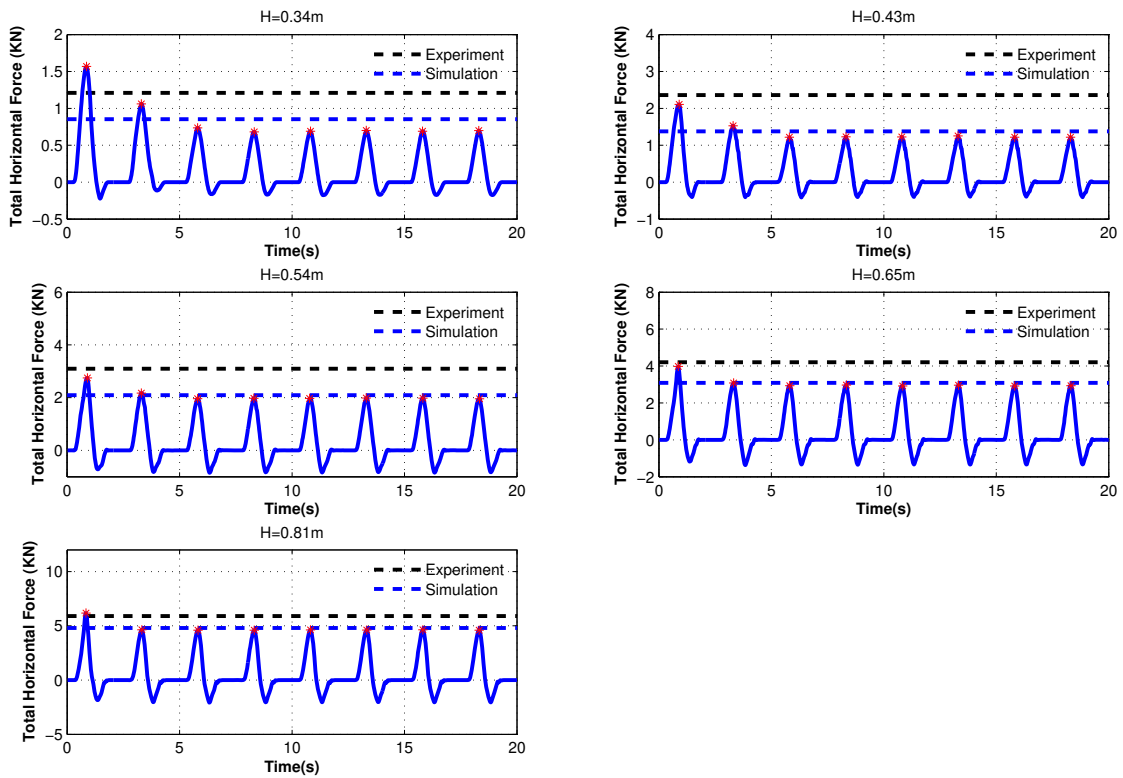


Figure 6.12: Horizontal force simulation results for Test #3

In Test #3 vertical forces are significantly under predicted. This happens because Test #3 does not consider the air entrapment under the bridge superstructure and also allows the water to move out of simulation domain from the side. In reality only air is able to rapidly move out of simulation domain from sides of bridge superstructure and water is confined between sides of wave flume. This means all models that do not consider the effect of air entrapment will probably do a good job of predicting horizontal wave forces while they significantly under predicts magnitude of vertical forces because they do not consider the air phase.

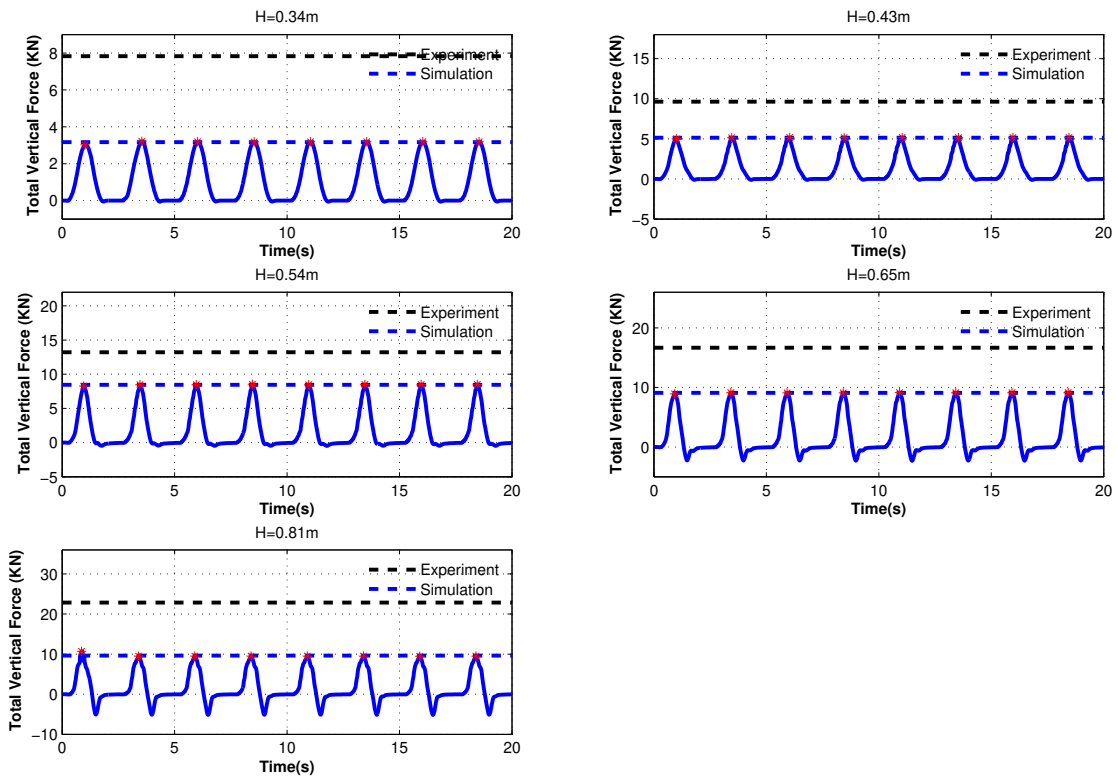


Figure 6.13: Vertical force simulation results for Test #3

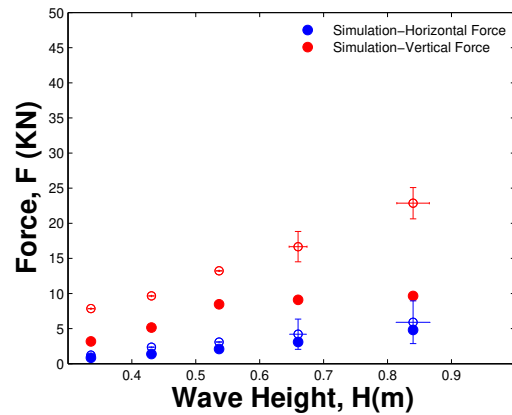


Figure 6.14: Comparison of horizontal and vertical simulation wave forces for Test #3 to experimental data

Simulation results of Test #3 proves that the accurate modeling of air movement under bridge superstructure is crucial to accurate prediction of hydrodynamic forces applied to bridge superstructure specially vertical forces. In order to more realistically model the movement of air under bridge superstructure in the next section, a 3D model is set up.

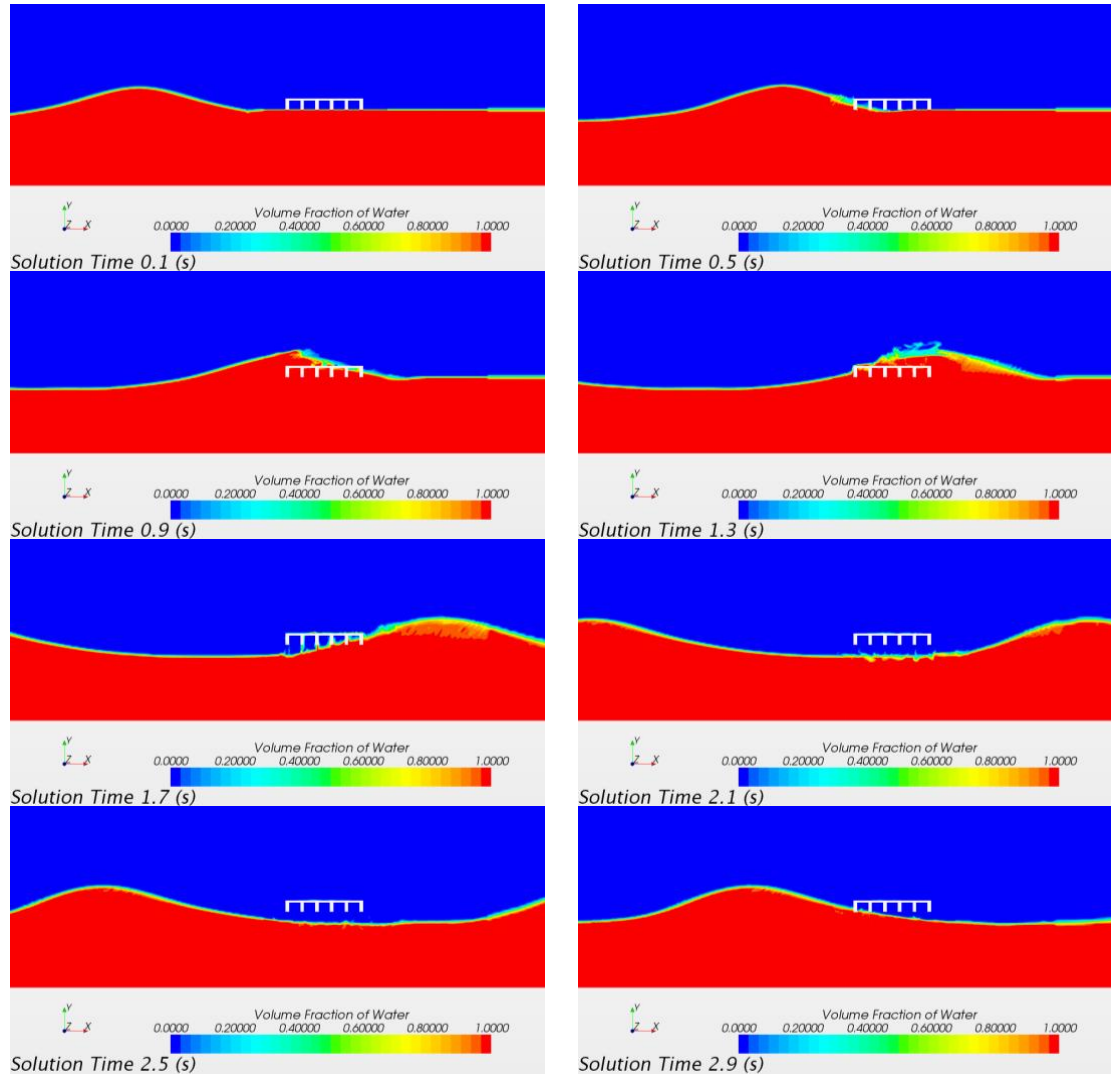


Figure 6.15: Volume of fluid (VOF) scene for $H=0.84\text{m}$, $dt=0.02$ (Test #3)

6.2 3D Model

3D model requires significantly bigger number of mesh cells compared to 2D model therefore requires more memory and computational time. In order to reduce the number of mesh cells used in the simulation and at the same time benefit from a full 3D simulation, symmetry plane is used at the center of bridge superstructure. The meshed bridge superstructure is shown in figure 6.16. The location of symmetry plane at the center of bridge is shown in figure 6.17

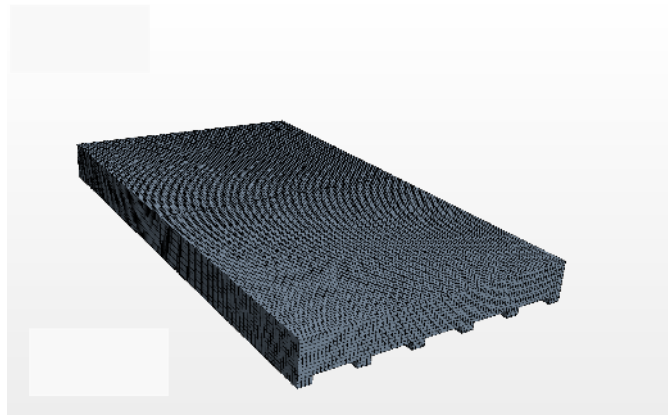


Figure 6.16: Meshed bridge in full 3D model

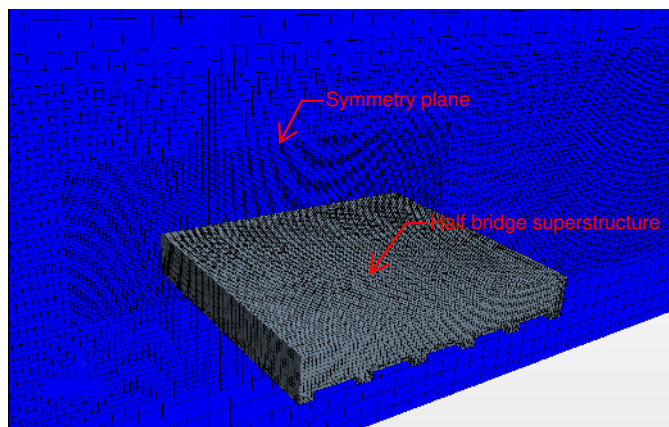


Figure 6.17: Meshed bridge in 3D model with symmetry plane

In order to verify whether the model with symmetry plane is equivalent to the full 3D model, the force time history of the full 3D model is compared with the force time history of the model with symmetry plane. The mesh and time step used are similar to mesh and time step used in Test #4 shown in table 6.2. The simulation result for total horizontal and vertical force on bridge superstructure is shown in Figure 6.18 and 6.19.

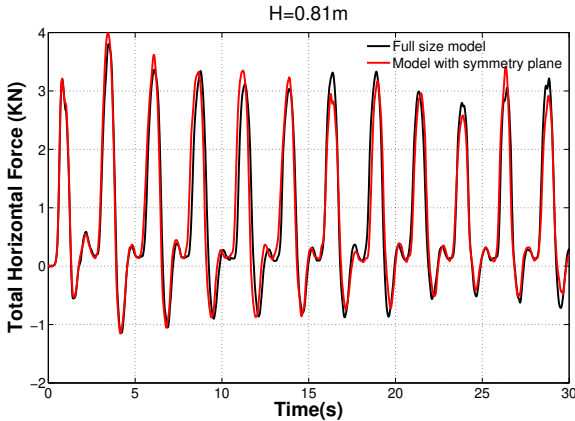


Figure 6.18: Comparison of total horizontal force in the full bridge superstructure model to the bridge superstructure model with symmetry plane

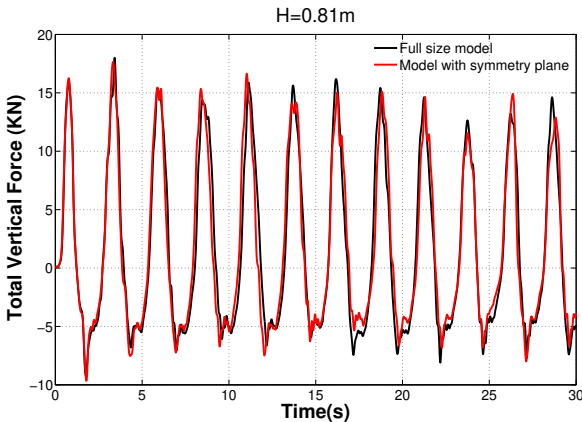


Figure 6.19: Comparison of total vertical force in the full bridge superstructure model to the bridge superstructure model with symmetry plane

As it is seen in these figures the horizontal and vertical force time histories are almost identical for full 3D bridge and bridge with a symmetry plane. As a result in all 3D modelings we use symmetry plane in the center of bridge because it helps us cutting the mesh needed in simulation domain into half. Table 6.2 shows the range of mesh sizes and time steps investigated in the 3D model. 3D model requires the size of mesh to be specified in transverse direction (y direction) as well. Since mesh aspect ratio (ratio of the sides of mesh in respect to each other) influence the solution accuracy and behavior, in all 3D simulation cases we attempted to keep this ratio as small as possible. The maximum mesh aspect ratio was used in free surface region in Test #6 and was 4.8.

| Test | Model | $\Delta t(s)$ | Mesh size (cm) | | | | | | Total # of cells |
|------|-------|---------------|----------------|------------|--------------|------------|------------|------------|------------------|
| | | | Bridge | | Free surface | | Deep water | | |
| | | | Δx | Δy | Δx | Δy | Δx | Δy | |
| 4 | 3D | 0.02 | 1.44 | 5.76 | 4.8 | 11.52 | 9.6 | 23.04 | 2,834,678 |
| 5 | 3D | 0.004 | 1.44 | 5.76 | 4.8 | 11.52 | 9.6 | 23.04 | 2,834,678 |
| 6 | 3D | 0.004 | 0.72 | 2.88 | 2.4 | 11.52 | 9.6 | 23.04 | 11,483,096 |

Table 6.2: Different mesh sizes and time steps investigated in 3D model

6.2.1 Simulation Results for Test #4

In Test #4 the time step used is $dt=0.02s$ which is equivalent to $T_p/125$. Horizontal force time history for $H=0.34m$ to $H=0.84m$ is shown in Figure 6.20. As it is seen in simulation force time history of horizontal forces, for all cases, simulation under predicts the horizontal forces. As the height of wave increase, the magnitude of error also increase. The maximum error happens for wave height of $H=0.84m$ and is about 44 percent which is slightly better than Test #1 which had the same time step but finer mesh in x and z direction.

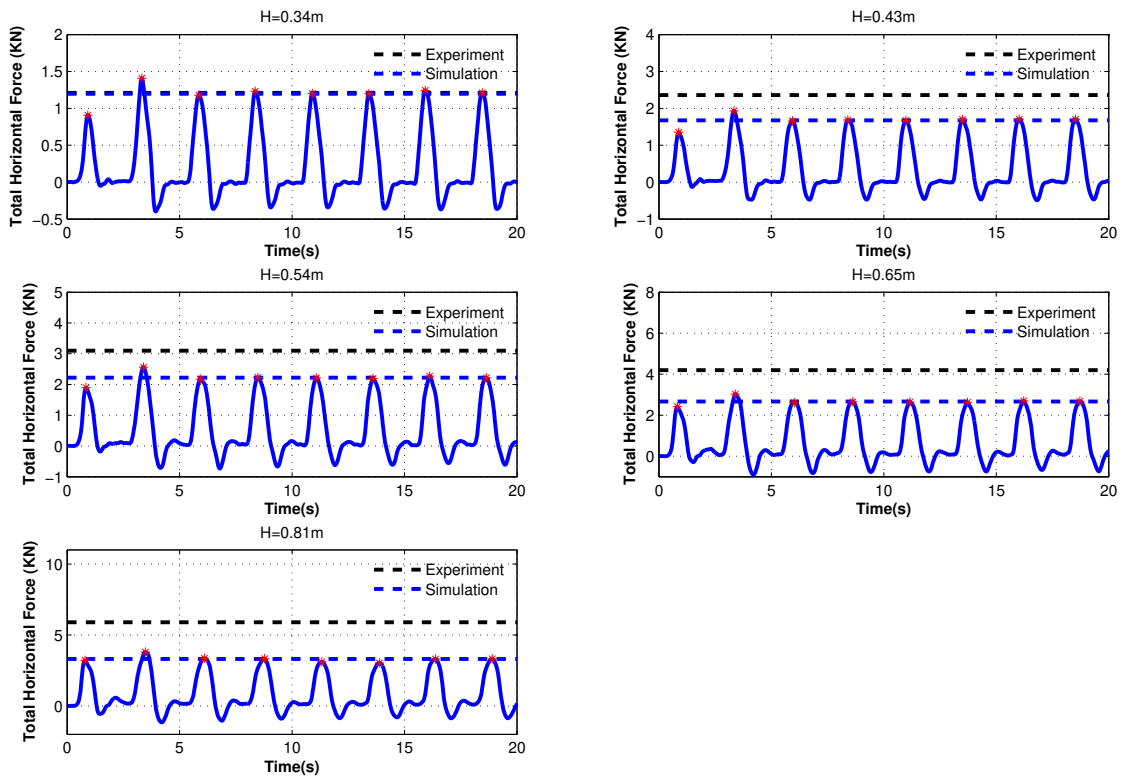


Figure 6.20: Horizontal force simulation results for Test #4

The vertical force time history for Test #4 is shown in figure 6.21. As it is seen in figure 6.21 and 6.22 simulation over predicts the magnitude of vertical forces for $H=0.34\text{m}$, $H=0.43\text{m}$ and under predicts vertical forces for $H=0.54\text{m}$, $H=0.66\text{m}$ and $H=0.84\text{m}$. For $H=0.34\text{m}$, simulation over predicts the magnitude of vertical forces by 17 percent. For $H=0.84\text{m}$, the simulation under predicts the magnitude of vertical forces by 31 percent. Comparing to Test #1, the maximum error in vertical force in Test#4 increased by 8 percent.

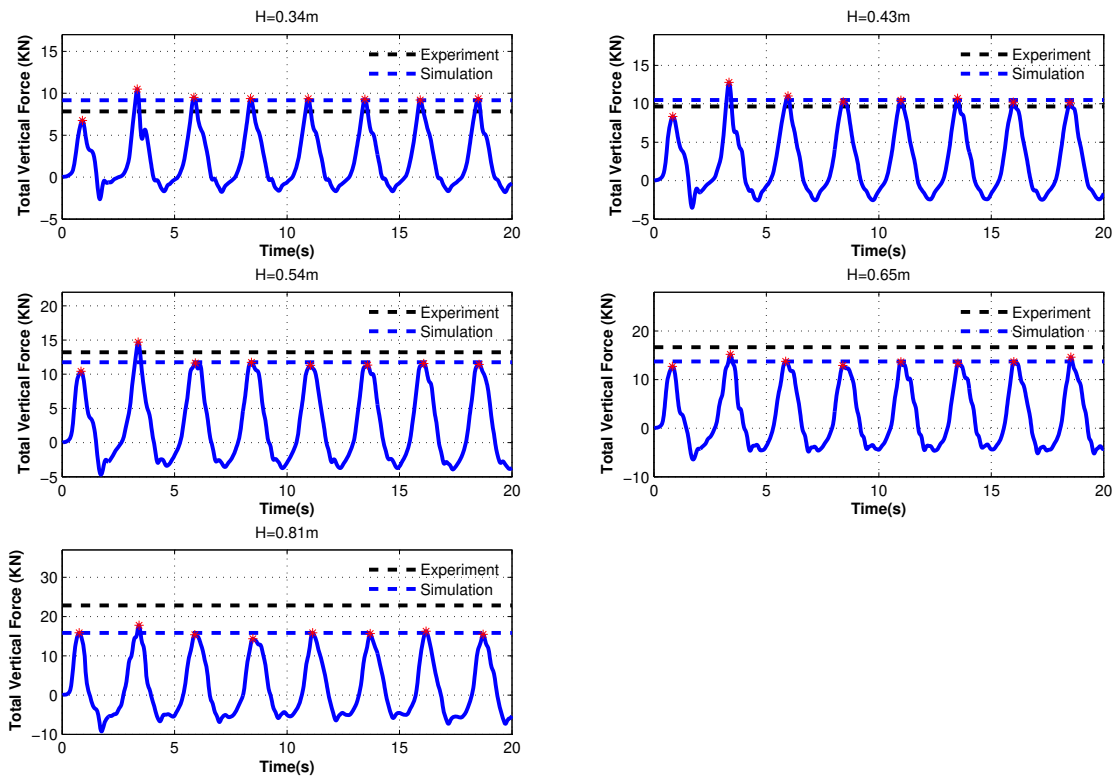


Figure 6.21: Vertical force simulation results for Test #4

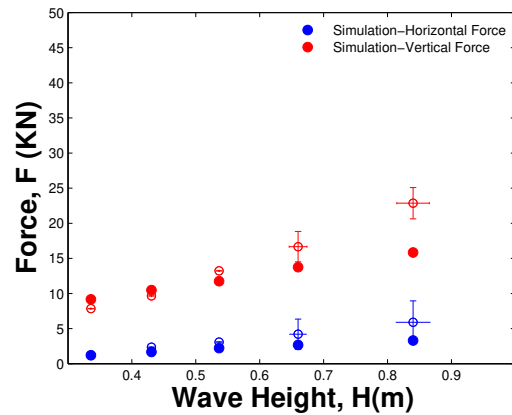


Figure 6.22: Comparison of horizontal and vertical simulation wave forces for Test #4 to experimental data

6.2.2 Simulation Results for Test #5

In Test #5 the time step is reduced to $dt=0.004s$ which is equivalent to $T_p/625$. This is done because in 2D model it was shown that reduction of time step improved the accuracy of horizontal force predictions. Mesh that is used in Test #5 is exactly the same as mesh used in Test #4. Horizontal force time history for $H=0.34m$ to $H=0.84m$ is shown in Figure 6.23. As the height of wave increase, the magnitude of error also increase. The maximum error happens for wave height of $H=0.84m$ and is about 27 percent which is better than Test #4 which had maximum error of 44 percent. The vertical force time history is shown in figure 6.24. As it is seen in figure 6.24 and 6.25 simulation over predicts the magnitude of vertical forces for $H=0.34m$, $H=0.43m$, $H=0.54m$, and $H=0.66m$ and under predicts the magnitude of vertical force for $H=0.84m$. For $H=0.34m$, simulation over predicts the magnitude vertical force by 60 percent. For $H=0.84m$, the simulation under predicts the magnitude of vertical force by 17 percent. Comparing to Test #4 vertical force time history results, Test #5 model does a better job of predicting vertical wave forces for $H=0.84m$. The error in prediction of wave forces for $H=0.34m$ increased from 17 percent to 60 percent. Comparing to Test #2 which had the same time step size, Test #5 predicts both horizontal and vertical forces with better accuracy. Compared to Test #2, the error in horizontal force prediction reduced by 10 percent and the error in vertical force prediction reduced by 33 percent. Looking into behavior of vertical force time history for $H=0.34m$, $H=0.43m$ and $H=0.54m$ we witness some oscillatory behavior similar to Test #2 results. Test #3 simulations showed that the oscillatory behavior in vertical force time history is the result of air entrapment between bridge girders and diaphragms. Test #5 time histories for $H=0.34m$, $H=0.43m$ and $H=0.54m$ show a similar behavior to Test #2 except for Test #5 oscillations having smaller amplitude than Test #2.

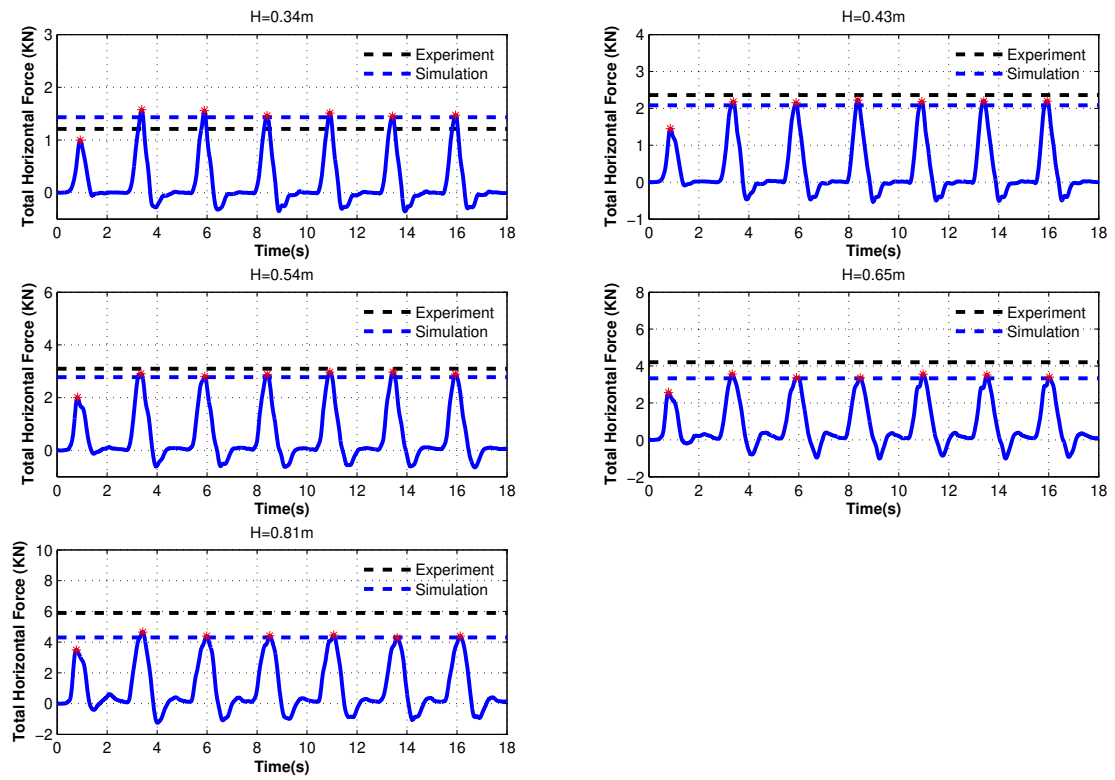


Figure 6.23: Horizontal force simulation results for Test #5

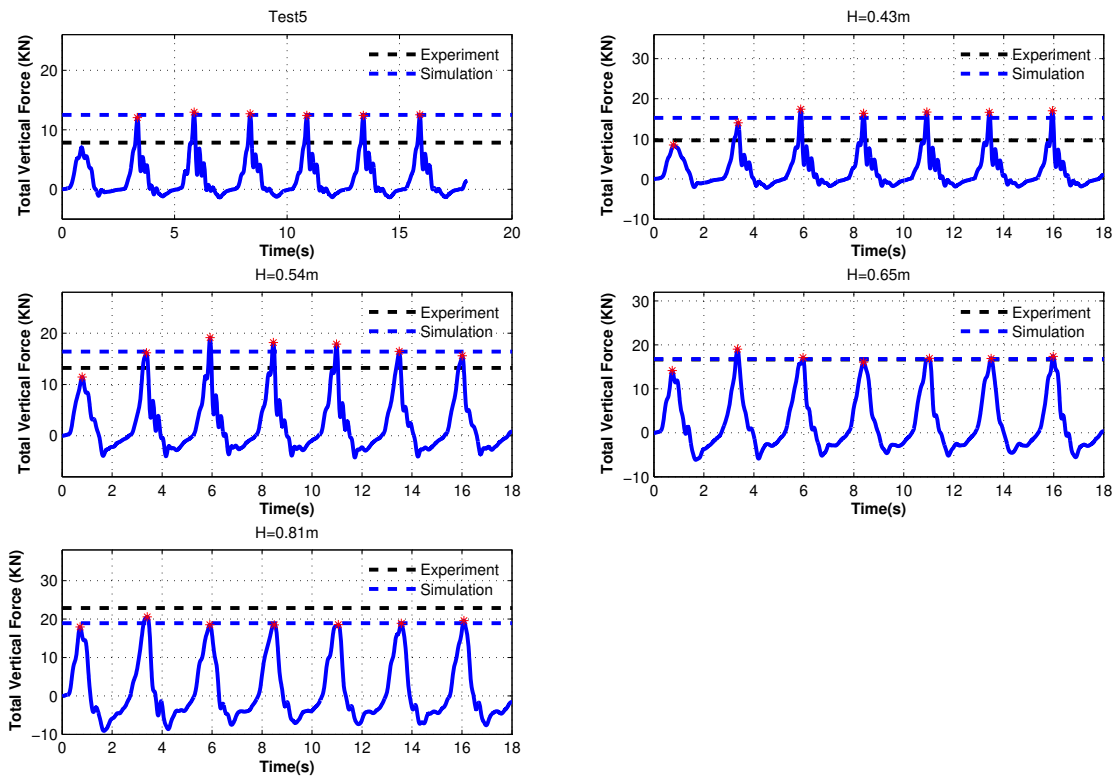


Figure 6.24: Vertical force simulation results for Test #5

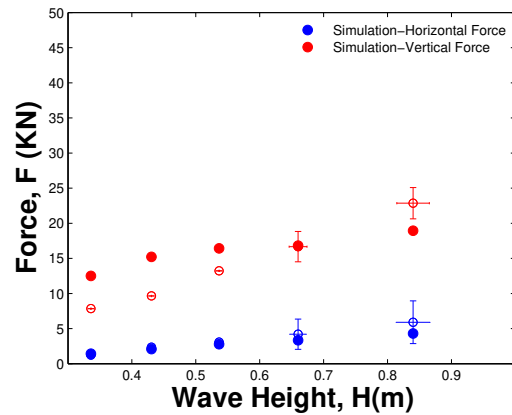


Figure 6.25: Comparison of horizontal and vertical simulation wave forces for Test #5 to experimental data

6.2.3 Simulation Results for Test #6

In Test #6 the time step used was $dt=0.004s$ which is equivalent to $T_p/625$. This is similar to Test #5. In respect to Test #5, in bridge region the size of mesh in all 3 directions is cut into half. This was done to more accurately model the movement of air between bridge girders and diaphragms as it was shown that the vertical force time history was sensitive to accurate modeling of air movement under bridge superstructure. Compared to Test #5 mesh in free surface is also refined in x and z direction but kept the same in y direction as it is assumed that x and z directions were more important than y direction and also because limited memory of computer resources did not allow for mesh refinement in y direction in free surface region. Horizontal force time history for $H=0.34m$ to $H=0.84m$ is shown in Figure 6.26. As it is seen, except for $H=0.34m$, for all wave heights, simulation under predicts the horizontal forces. For $H=0.34m$, Test #6 simulation over predicts the magnitude of horizontal force by 15 percent. As the height of wave increase, the magnitude of error also increase. The maximum error happens for wave height of $H=0.84m$ and is about 32 percent. Compared to Test #5 the magnitude of error increased by 5 percent.

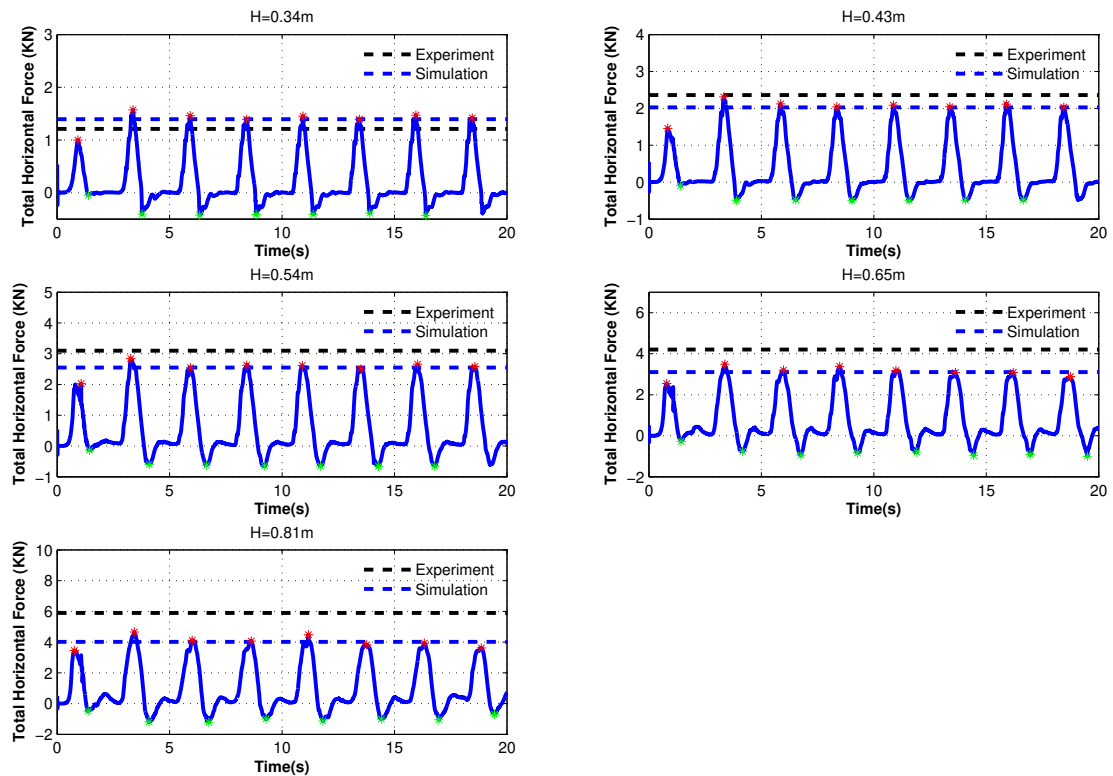


Figure 6.26: Horizontal force simulation results for Test #6

The vertical force time history is shown in figure 6.27. As it is seen in figure 6.27 and 6.28, simulation over predicts the magnitude of vertical forces for $H=0.34\text{m}$, $H=0.43\text{m}$, and $H=0.54\text{m}$, and under predicts the magnitude of vertical forces for $H=0.66\text{m}$ and $H=0.84\text{m}$. For $H=0.34\text{m}$, simulation over predicts the magnitude of vertical forces by 23 percent. For $H=0.84\text{m}$, the simulation under predicts the magnitude of vertical forces by 26 percent. Comparing to Test #5 vertical force time history results, Test #6 model does a better job of predicting vertical wave forces for $H=0.34\text{m}$ (for $H=0.34\text{m}$ error reduced from 60 percent to 23 percent). However the error in vertical force prediction for $H=0.84\text{m}$ increased from 17 percent to 26 percent.

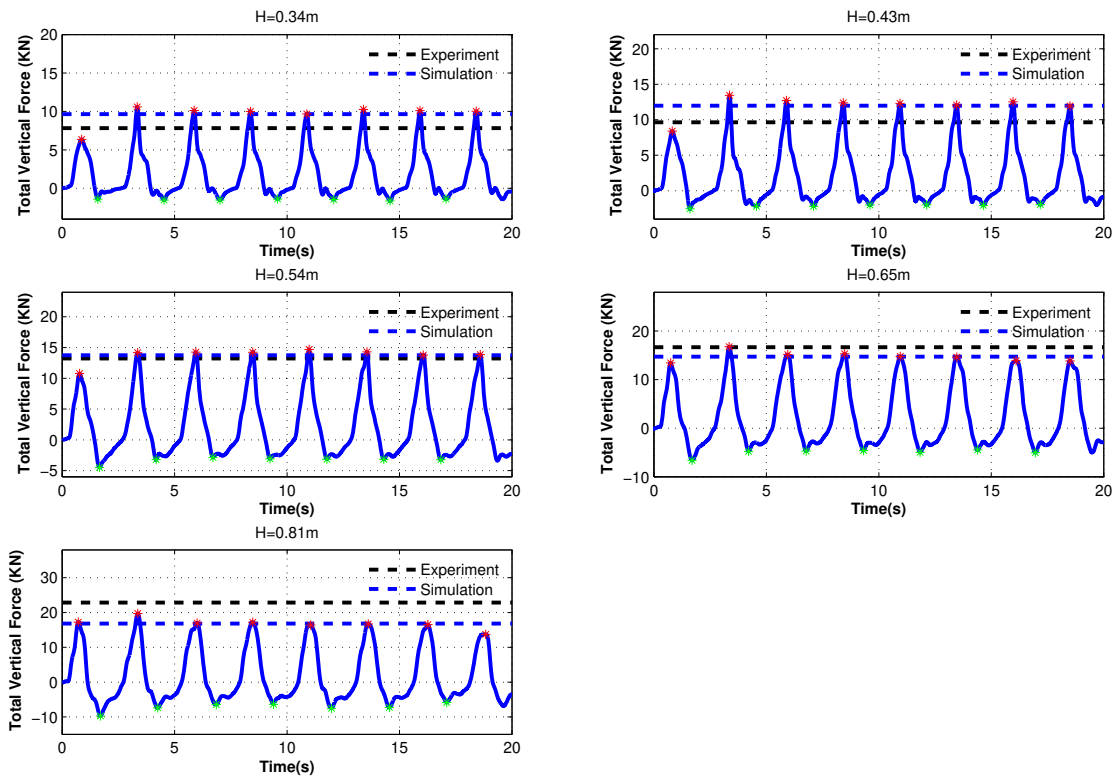


Figure 6.27: Vertical force simulation results for Test #6

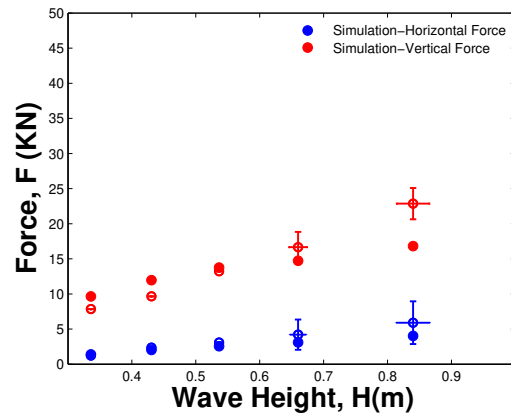


Figure 6.28: Comparison of horizontal and vertical simulation wave forces to experimental data for Test #6

For Test #6 we can also compare the negative horizontal and vertical forces in simulations to experimental data from Oregon State University. For horizontal forces negative means in the direction opposite to the direction of wave propagation. For vertical forces, negative means downward direction. The comparison of positive and negative horizontal forces and experimental data is shown in figure 6.29. As it is evident in this figure, negative horizontal forces are in excellent agreement with experimental data. Positive and negative vertical forces for Test #6 are shown in figure 6.30. As it is evident in this figure, negative vertical forces are also in a very good agreement with experimental data.

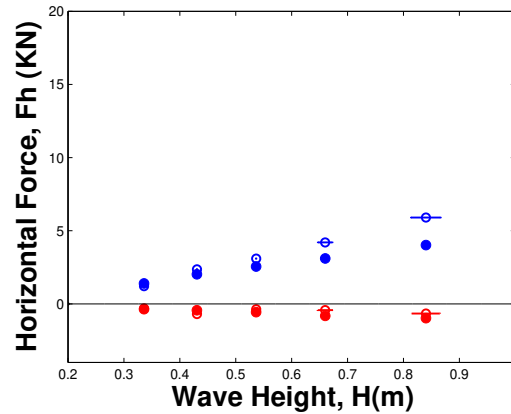


Figure 6.29: Comparison of positive and negative horizontal forces to experimental data

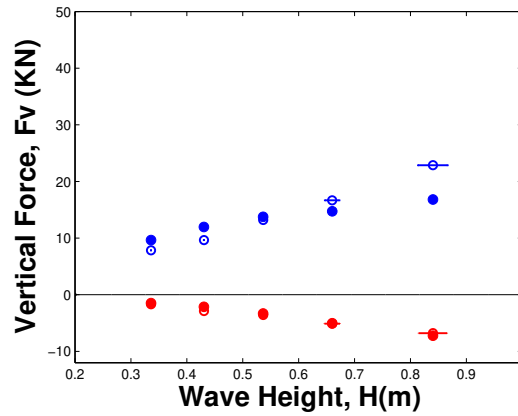


Figure 6.30: Comparison of positive and negative vertical forces to experimental data

Figure 6.31 shows error distribution of horizontal forces for Test #6. As it is seen in this figure, for all wave heights except $H=0.34\text{m}$ simulation under predicts the magnitude of total horizontal force applied to bridge superstructure. The maximum error happens for $H=0.84\text{m}$ and is about 32 percent.

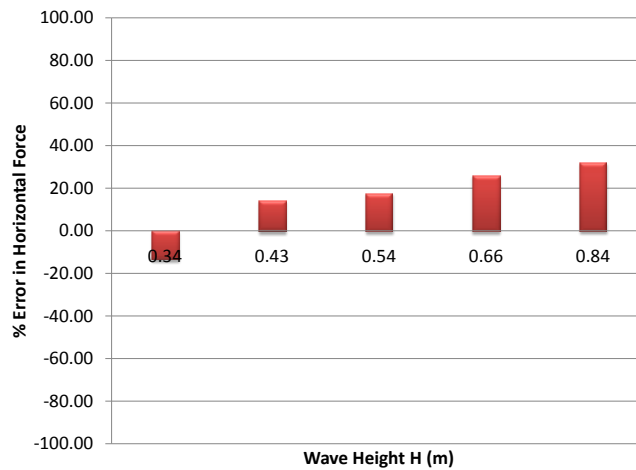


Figure 6.31: Error distribution for quasi-steady horizontal wave forces for Test #6

Figure 6.32 shows error distribution of vertical forces for Test #6. Simulation over predicts the magnitude of vertical force for H=0.34m and H=0.43m and H=0.54m and under predicts the magnitude of vertical force for H=0.66m, and H=0.84m. The maximum error happens for H=0.84m and is about 26 percent.

Figures 6.33 to 6.38 show some snap shots from Test #6 simulations. It is meaningful to compare 3D simulation snapshots to 2D simulation snapshots. Figure 6.7 and 6.33 show VOF scene of interaction of one wave with bridge superstructure for 2D Test #2 and 3D Test #6 respectively. VOF snapshots look very similar at the start of simulation but they start to differ after 1.3s. The wave interacts faster with bridge superstructure in 3D model compared to 2D model.

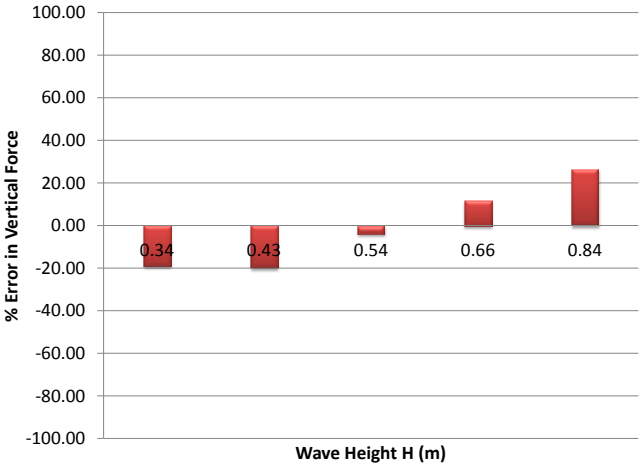


Figure 6.32: Error distribution for quasi-steady vertical wave forces for Test #6

At 2.5s in 2D model the wave is still touching the bridge superstructure while in 3D model wave almost separated from bridge superstructure. The pattern of air entrainment signified with yellow color, also seems to be different in 2D and 3D model.

Comparison of 3D velocity vector scene to 2D velocity vector scene shows that in different instances maximum velocities are very close to each other. Velocities in 3D model are within 18 percent of maximum velocities in 2D model in all instances except for $t=2.1s$ where the difference between maximum velocity in 2D and 3D model is about 46 percent.

Comparison of 3D maximum horizontal velocity magnitude to 2D maximum horizontal velocity magnitude (in the direction of wave propagation) shows that at different instances, in general horizontal velocities in 2D and 3D model are close, However as simulation time progress the maximum horizontal velocities in 2D and 3D model tend to not agree very well with the difference of maximum velocities reaching about 60 percent at $t=2.1s$.

Comparison of 3D maximum vertical velocity magnitude to 2D maximum vertical velocity magnitude (in upward direction) shows that at different instances, in general vertical velocities in 2D and 3D model are close, However as simulation time progress the maximum vertical velocities in 2D and 3D model tend to not agree very well with the difference of maximum velocities reaching about 70 percent for $t=1.7s$.

Even though maximum velocities do not match very well in 2D and 3D model for some instances, overall velocity contours are close to each other. In 3D model wave looks to interact with bridge in a shorter period of time while in 2D model the wave looks to stick to bridge superstructure for longer time. As simulation time progress, the difference between 2D and 3D snapshots becomes more pronounced.

Figure 6.38 shows the 3D iso surface scene of one wave interacting with bridge superstructure. Visual Comparison of complex free surface profile captured in simulation to videos available from Oregon State University shows that simulation did a good job of capturing most of the important features of wave-bridge interaction.

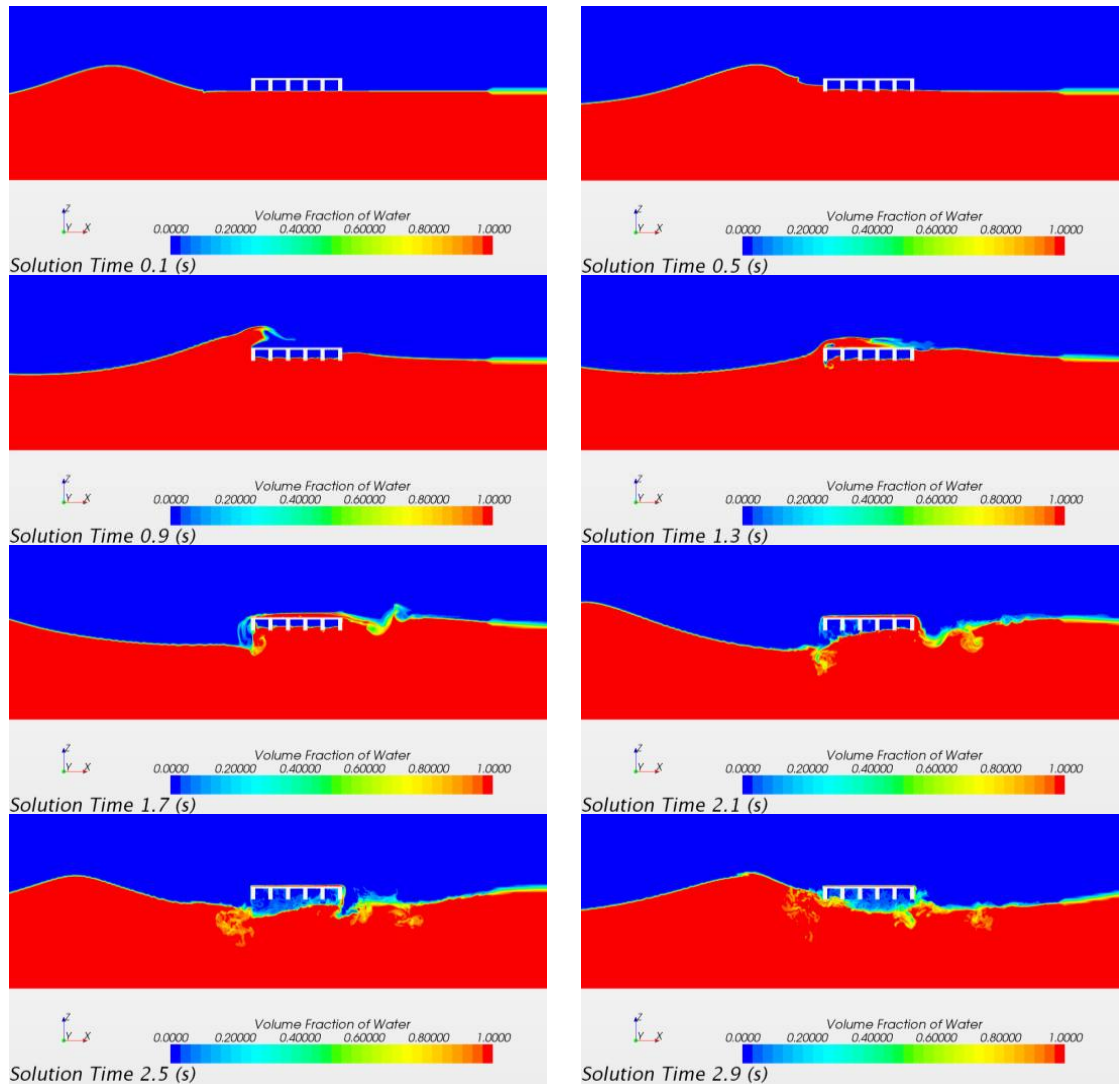


Figure 6.33: Volume of fluid (VOF) scene for $H=0.84\text{m}$ (Test #6)

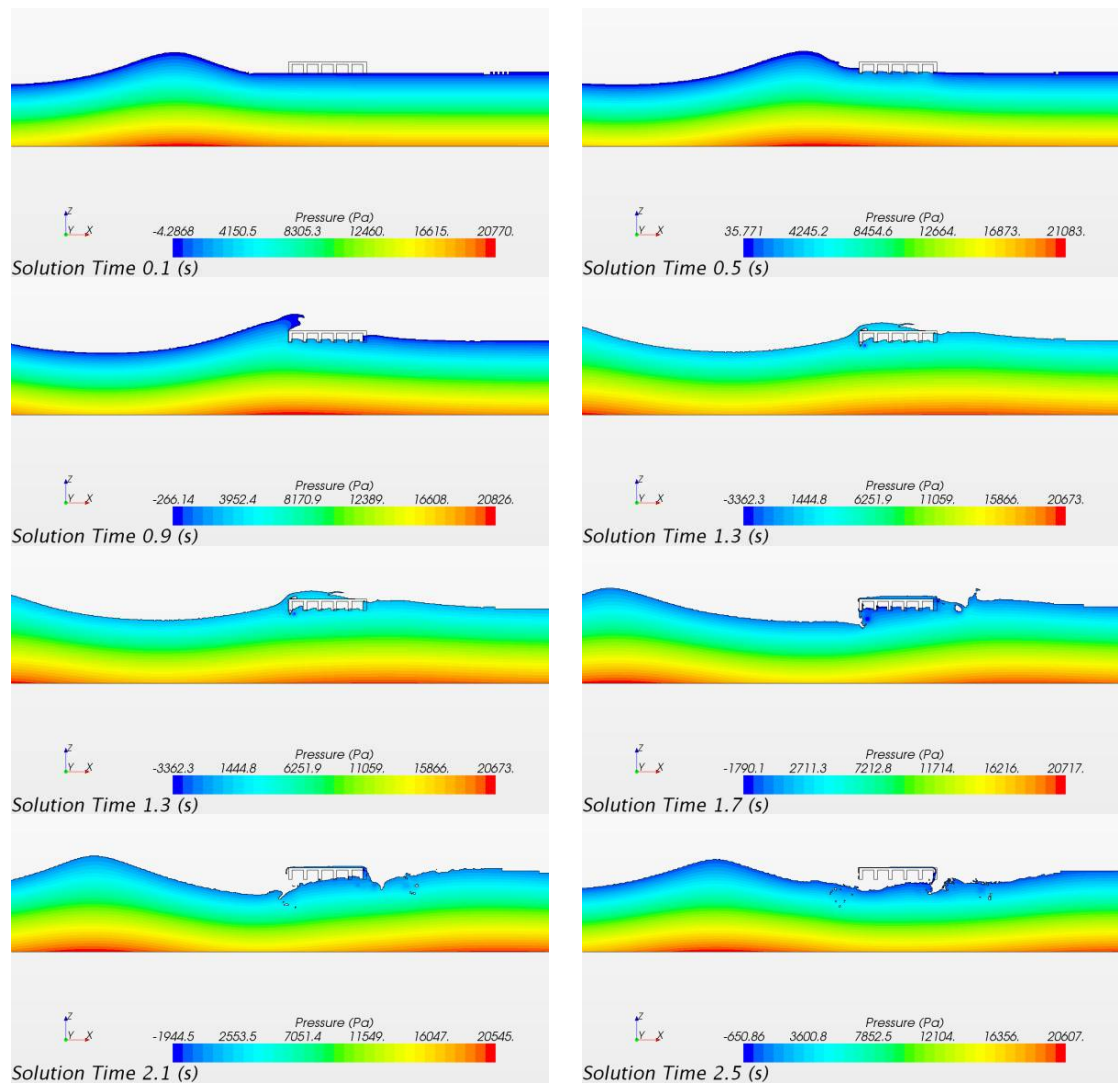


Figure 6.34: Pressure scene for $H=0.84\text{m}$ (Test #6)

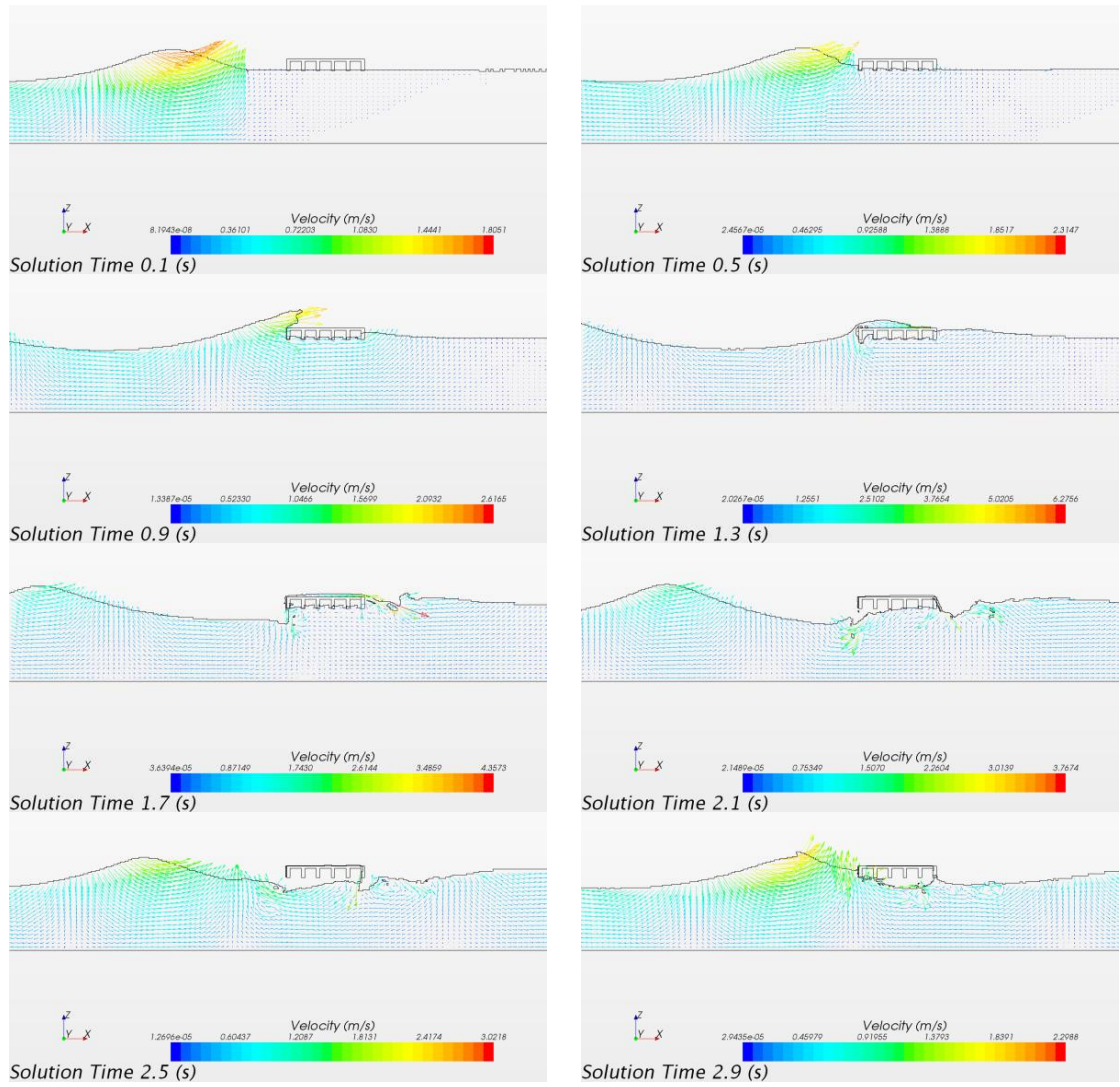


Figure 6.35: Velocity vector scene for $H=0.84\text{m}$ (Test #6)

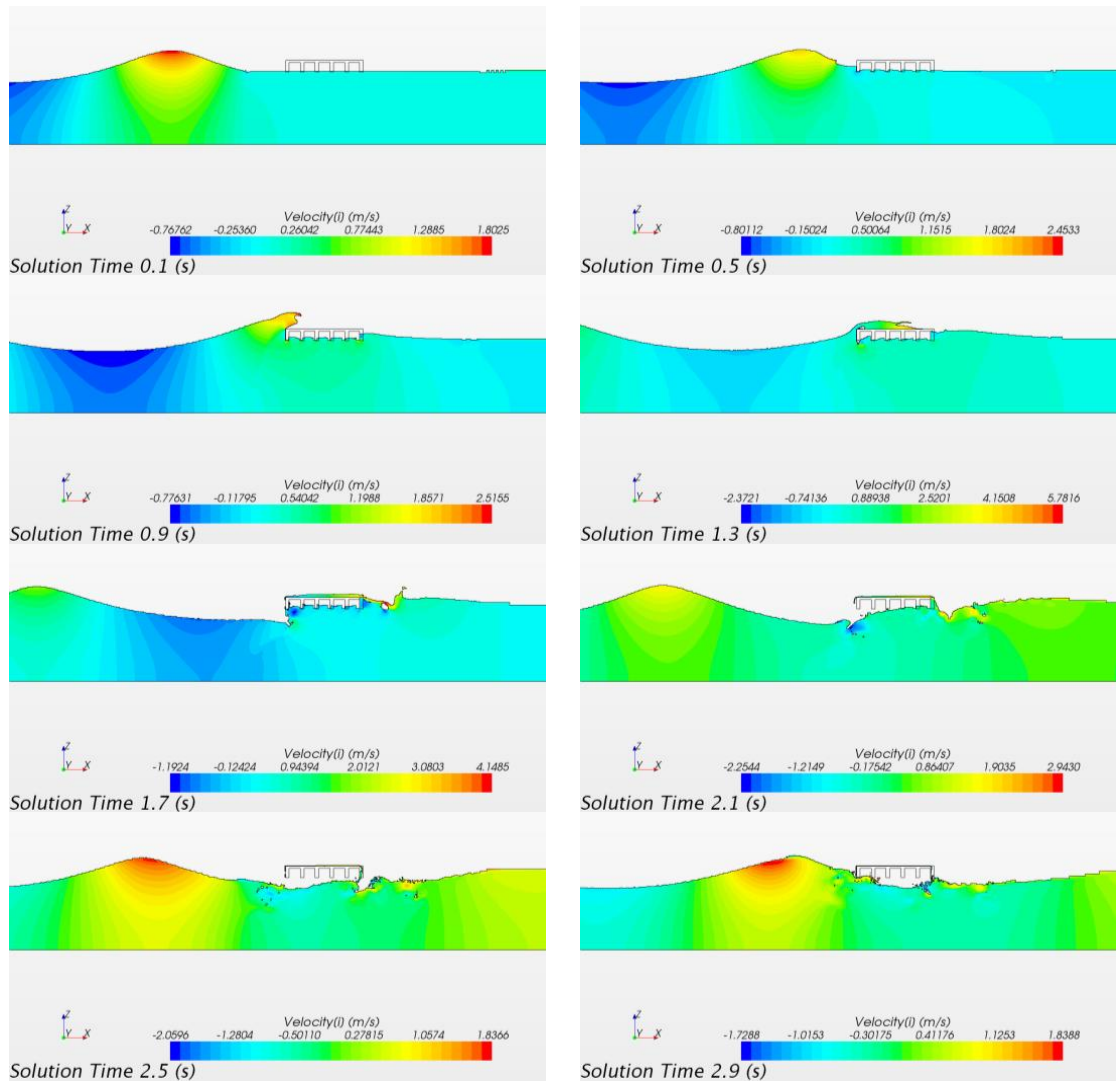


Figure 6.36: Velocity magnitude in horizontal direction for $H=0.84\text{m}$ (Test #6)

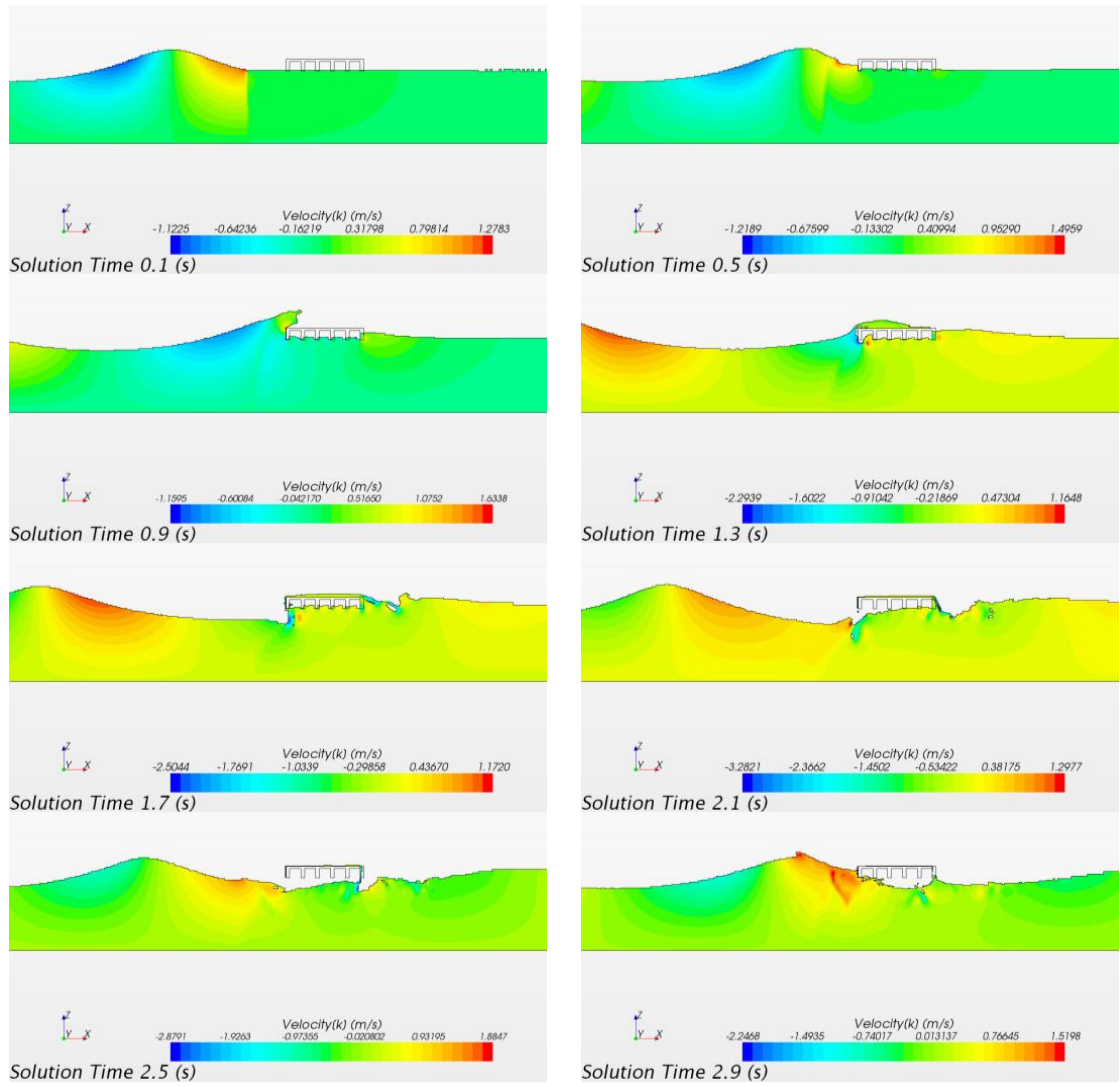


Figure 6.37: Velocity magnitude in vertical direction for $H=0.84\text{m}$ (Test #6)

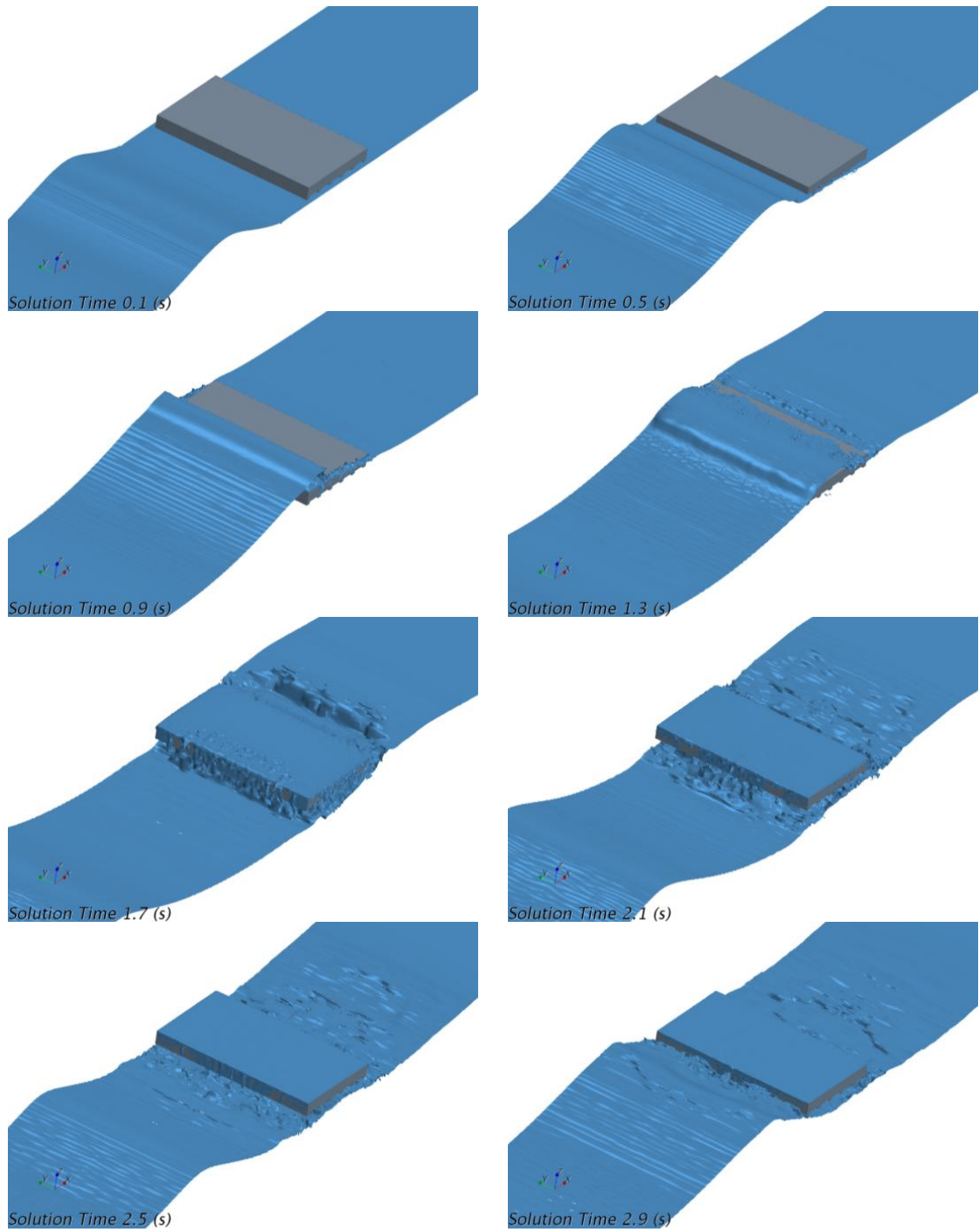


Figure 6.38: 3D iso surface for $H=0.84\text{m}$ (Test #6)

6.3 Discussion on Slamming Force

In experiments conducted at Oregon State University, even though pressure measurements contained the classic leading spike followed by quasi-steady pressure shown in figure 6.39, a review of the corresponding forces shown in figure 6.40 did not reveal a similar pattern. In contrast the load cell data only contained the quasi-steady force Bradner and Cox (2008).

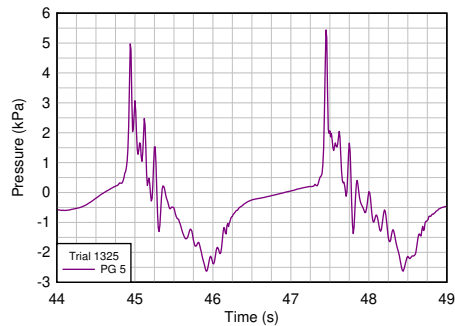


Figure 6.39: Pressure measurement taken beneath the deck adapted from Bradner and Cox (2008)

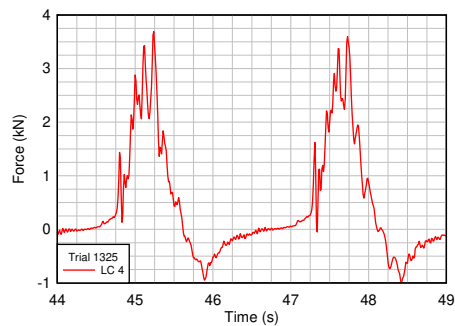


Figure 6.40: Corresponding measurement of the nearest load cell adapted from Bradner and Cox (2008)

In addition review of experimental data shows that not all the pressure measurements contained the dramatic impact spike shown in figure 6.39. One set of pressure gauges that did not show the impact spike where those mounted to the front face of the offshore external girder (shown in figure 5.6). These pressure sensors where positioned at locations where air entrapment did not happen Bradner and Cox (2008). This is consistent with our findings in this research that oscillatory behavior in vertical force time history is the result of wave interacting with entrapped air under the bridge superstructure inside cavities between bridge girders and diaphragm. As it was seen, in Test #3 when the air was allowed to completely vent out from the side of simulation domain, the slamming oscillations completely disappear from vertical force time history.

In all simulations that captured slamming oscillations (Test #2, Test #5, and Test #6), slamming oscillations were captured for some wave heights not for all. These include $H=0.34\text{m}$, $H=0.43\text{m}$, and $H=0.54\text{m}$. This is shown in figure 6.41. Slamming oscillation seem to be related to the amount of pressure incurred by trapped air under the bridge superstructure. As the wave height increase, the pressure applied to layer of trapped air between bridge superstructure and wave also increase. This increase leads to less oscillatory behavior in vertical simulation time histories for all Test cases. As a result vertical force time history for $H=0.84\text{m}$ does not show oscillatory pattern seen in vertical force time history for $H=0.34\text{m}$. This trend is consistent with findings in paper by Brody et al. (2011) which shows through basic fluid equations that the frequency of oscillation witnessed at surface of water beneath the trapped air in a plastic tube depend on the pressure applied to trapped air in the tube.

Also it was shown that when proper mesh is used. The number of slamming oscillations are equal to the number of cavities under the bridge superstructure. This is shown for Test #6 in figure 6.42. Effect of model choice (2D vs 3D) and different mesh sizes on slamming force oscillations is also shown in figure 6.42

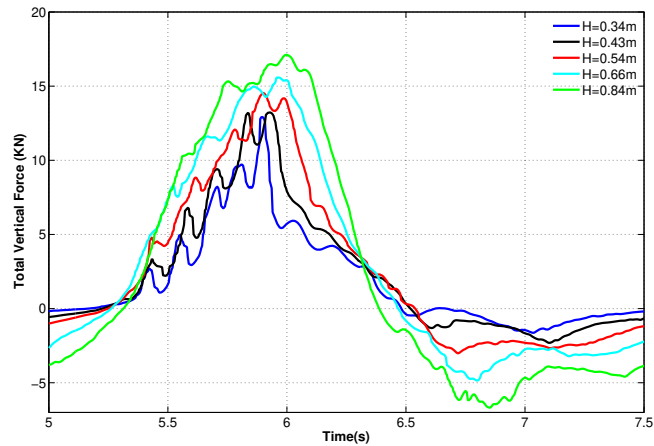


Figure 6.41: Vertical force time history for one wave period for Test #6 for different wave heights

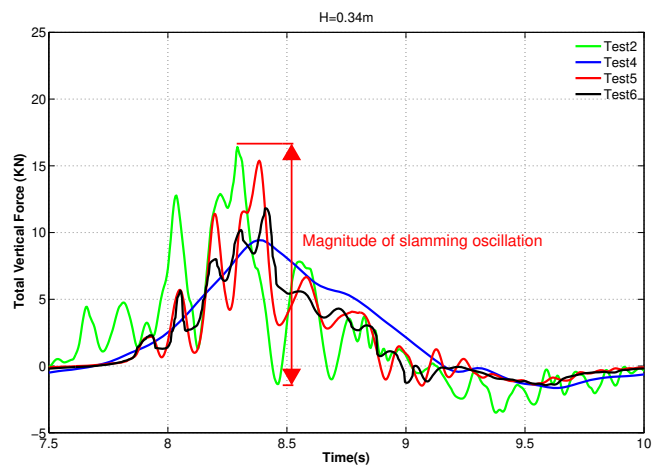


Figure 6.42: Effect of model choice and mesh size on magnitude of slamming force oscillation

As it is evident in figure 6.42, the magnitude of slamming oscillation depends on the amount of air entrapment under the bridge superstructure. In Test #2 which was a 2D model with two symmetry plane on sides of simulation domain, the model did not

allow any air to escape from sides of simulation domain. As a results the magnitude of slamming force is biggest for Test #2 compared to all other cases. Test #5 was a 3D case where air was allowed to move in transverse direction. This allowed some air to escape and the magnitude of slamming oscillation for Test #5 is smaller than Test #2. In Test #6 we further refined the mesh in bridge region by reducing the mesh size in all three dimensions into half (in respect to Test #5). This allowed more accurate modeling of air movement between girders and diaphragms. As a result Test #6 had the smallest magnitude of slamming oscillation compared to Test #2, Test #4 and Test #5. Unfortunately current computer resources does not allow to use smaller mesh than Test #6. However, the results of Test #6 are reasonably close to experimental data available from Oregon State University. Test #4 was not able to capture the slamming oscillation because the time step used in simulation was not small enough to capture high frequency slamming oscillations.

Since the slamming force was not captured in force time history available from Oregon State University, it is not possible to compare the slamming force to experimental data. How ever, qualitatively the results of Test #6 in terms of shape of slamming force is closest to the ones captured in the University of Florida experimental data (5.30).

6.4 Discussion on Simulation Results

As it was shown in previous section, the choice of mesh size and time step greatly influence the accuracy of simulations for total horizontal and vertical forces applied to bridge superstructure. Since the effect of mesh size and time step on different wave heights, varies, Normalized Root Mean Square Error (NRMSE) is calculated for all wave heights, as a measure of accuracy for each simulation test case. Table 6.3 shows NRMSE for all test cases in addition to maximum error in horizontal and vertical force

for each test case. A good quality simulation is a simulation where NRMSE for both hor-

| Test | F _x ,NRMSE % | F _z ,NRMSE % | Max %error in F _x | Max %error in F _y |
|------|-------------------------|-------------------------|------------------------------|------------------------------|
| 1 | 35 | 15 | 48 | 23 |
| 2 | 25 | 36 | 37 | 93 |
| 3 | 20 | 51 | 19 | 58 |
| 4 | 31 | 24 | 44 | 31 |
| 5 | 18 | 26 | 27 | 60 |
| 6 | 22 | 21 | 32 | 26 |

Table 6.3: Error witnessed in simulation results for different Test cases

izontal and vertical wave forces are reasonably small. In addition the maximum error in prediction of horizontal and vertical wave forces applied to bridge superstructure should also be reasonably small. Looking into data of table 6.3 the most accurate prediction of both horizontal and vertical forces are obtained in Test #6. Test #6 has reasonably small NRMSE for both horizontal and vertical force predictions and the maximum error witnessed in horizontal and vertical predictions are also reasonably small. Looking into the data of table 6.3 we can draw the following conclusions regarding the effect of time step, mesh size, and model selection (2D vs 3D) on accuracy of simulation predictions:

- Reducing time step size improved accuracy of simulations in predicting total horizontal forces in both 2D and 3D models. In 2D model reducing time step from $dt=0.02s$ to $dt=0.004s$ reduced the NRMSE for horizontal forces by 10 percent. In addition the maximum error in horizontal force predictions reduced by 11 percent. In 3D model reducing time step from $dt=0.02s$ to $dt=0.004s$ reduced the NRMSE by 13 percent and the maximum error in horizontal force predictions reduced by 17 percent.
- Reducing time step did not necessarily improve the accuracy of vertical force predictions. For example in 2D model, when time step is reduced from $dt=0.02s$ to

dt=0.004s (Test #1 and Test #2) the NRMSE increased by 21 percent and maximum error in vertical force increased by 70 percent. In the same way, in 3D model when time step reduced from dt=0.02s to dt=0.004s (Test #4 and Test #5) the NRMSE increased by 2 percent and maximum error in vertical force increased by 29 percent.

- Reducing time step from dt=0.02s to dt=0.004s improved vertical force predictions only in 3D model with sufficiently fine mesh in transverse direction (y direction). Comparison of Test #4 to Test #6 shows that when time step is reduced from dt=0.02s to dt=0.004s, NRMSE for vertical force reduced by 3 percent and the maximum error in vertical force prediction is reduced by 5 percent.
- Overall while reducing time step in both 2D and 3D models improved the accuracy of horizontal force predictions, it did not improve the accuracy of vertical force predictions significantly. The vertical force predictions only improved slightly in 3D model with sufficiently fine mesh in bridge region in all three directions (Test #6). In all other cases (Test #2 and Test #5) when the time step was reduced, the error in vertical forces were amplified.
- Comparison of Test #5 to Test #6 shows that when time step size of $dt=T_p/625$ was used, refining the mesh in bridge region improved the maximum error in vertical force prediction by 34 percent. However as we see NRMSE and maximum error in horizontal force increased by 4 percent and 5 percent respectively. This could be attributed to larger mesh aspect ratio used in Test #5 in free surface region. In Test #5 the mesh aspect ratio in free surface region was 2.4. In Test #6 the mesh aspect ratio in free surface region was 4.8.
- In order to accurately model both quasi steady and slamming oscillations, a 3D model with a time step size of order of dt=0.004s or $dt=T_p/625$ and a sufficiently

small mesh in all three directions in bridge region is required. When time step size is reduced, failure to properly refine mesh in bridge region would create very large error for wave heights which contain slamming oscillations (maximum error in vertical force increased by 29 percent in Test #5 compared to Test #4).

6.5 Guidelines for Choosing Mesh and Time Step Size in Wave-Structure Interaction Problems

Data of table 6.3) shows that the two phase Navier Stokes equations are very sensitive to the choice of mesh size and time step for problems in which air entrapment significantly influences magnitude of forces applied to structure. Using time step sizes bigger than $dt=T_p/125$ causes excessive wave dissipation which will cause the wave to die out quickly before reaching the bridge and can not model the complex wave-bridge interaction very accurately. In order to capture slamming oscillations and improve the accuracy of horizontal force predictions, time step size of order of $dt=T_p/625$ or smaller is required. With this time step, the mesh used is also required to be sufficiently fine. Otherwise reducing the time step will amplify the error in vertical force predictions in both 2D and 3D models. Error generated in vertical force predictions due to reduction in time step is mainly due to inaccurate modeling of air movement between cavities that exist between bridge girders and diaphragms. The best result obtained was for Test #6 in which the following mesh was used in different simulation regions. Directions x, y and z are shown in figure 5.19.

| Region | Mesh size in x direction | Mesh size in z direction | Mesh size in y direction |
|--------------|--------------------------|--------------------------|--------------------------|
| Bridge | $\lambda/1305$ | $H/117$ | $\lambda/326$ |
| Free surface | $\lambda/391$ | $H/35$ | $\lambda/82$ |
| Deep water | $\lambda/98$ | $H/9$ | $\lambda/41$ |

Table 6.4: Mesh used in Test #6 in terms of wave length λ and wave height H (λ is calculated for $H=0.84\text{m}$)

6.6 Viscous Effects

In all previous simulations viscous effects were neglected because in wave-bridge interaction problem we are dealing with a large mass of water interacting with bridge superstructure in a very short period of time. Using non viscid model in STAR-CCM+ made our simulations less complicated in terms of modeling and the processing time since boundary layers and other viscous effects were not resolved.

Although it is possible to simulate turbulent flow directly by resolving all the scales of the flow (called direct numerical simulation), the computer resources required are too large for practical flow simulations. Therefore, a suitable turbulence modeling approach must be selected. STAR-CCM+ offers wide range of turbulent models. The turbulence models in STAR-CCM+ are responsible for providing closure of the governing equations in turbulent flows. In general, there are three approaches for modeling turbulence. These include:

- Models that provide closure of the Reynolds-Averaged Navier-Stokes (RANS) equations.
- Large eddy simulation (LES).
- Detached eddy simulation (DES).

Second and third approach (LES and DES) are extremely sensitive to grid resolution and are computationally far more expensive than first approach. They need to be used

for a group of problems in which resolving the small time and length scales are indeed justified.

STAR-CCM+ offers four major classes of turbulent models based on Reynolds-Averaged Navier-Stokes (RANS) equations. These include: Spalart-Allmaras, K-Epsilon, K-Omega and Reynolds stress transport models. CD-adapco (2010) provides broad guideline to the applicability of each of these models. Further guidance on selecting the specific model variants can be found within the sections that provide details about the models in STAR-CCM+ manual (CD-adapco (2010)). In this research we used K-Omega model to evaluate the magnitude of viscous forces in wave-bridge interaction problem. K-Omega model is essentially very similar to K-Epsilon in that two transport equations are solved, but differ in the choice of the second transported turbulence variable (CD-adapco (2010)). The turbulent equations solved include two variables, the turbulent kinetic energy K and a quantity called ω which is defined as specific dissipation rate per unit turbulent energy. One advantage of K-Omega model over K-Epsilon model is its improved performance for boundary layers under adverse pressure gradients. However, the most important advantage of K-omega over K-Epsilon model is that it can be applied throughout the boundary layer, including the viscous-dominated region, without further modification. Furthermore, the standard K-Omega model can be used in this mode without requiring the computation of wall distance (CD-adapco (2010)). The biggest short coming of the K-Omega model boundary layer computations is that it is very sensitive to the values of ω in the free stream. This shortcoming was addressed in STAR-CCM+ by introduction of SST K-Omega Model which improves original K-Omega model based on the paper by Menter (1994). Menter (1994) essentially blended K-Epsilon model in the far-field with a K-Omega model near the wall. This approach improves the biggest drawback in applying K-Omega model to practical flow simulations.

SST K-Omega Model was applied to wave-bridge interaction problem for two wave heights were maximum error in prediction of hydrodynamic forces were witnessed. These wave heights are $H=0.34\text{m}$ and $H=0.84\text{m}$ (figures 6.31 and 6.32). Mesh size and time step used in Test #6 from previous chapter was used to ensure solution accuracy. Figure 6.43 and 6.44 show comparison of total horizontal and vertical forces for $H=0.34\text{m}$ using SST K-Omega Model to simulation results of Test #6 using inviscid model. As we witness in these figures, comparison of simulation results for both horizontal and vertical forces using SST K-Omega model to inviscid model do not show a significant difference as both graphs almost overlap each other. From this, we conclude that viscous effects do not play a major role in hydrodynamic forces applied to bridge superstructure for wave height of $H=0.34\text{m}$.

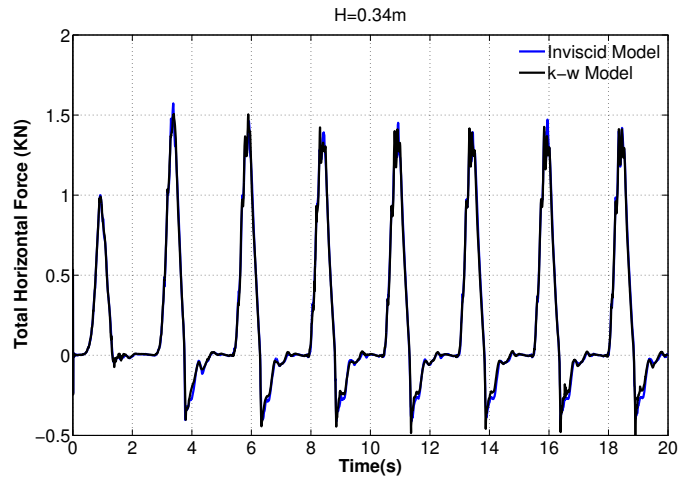


Figure 6.43: Comparison of horizontal forces using SST K-Omega model to inviscid model for $H=0.34\text{m}$ for Test #6

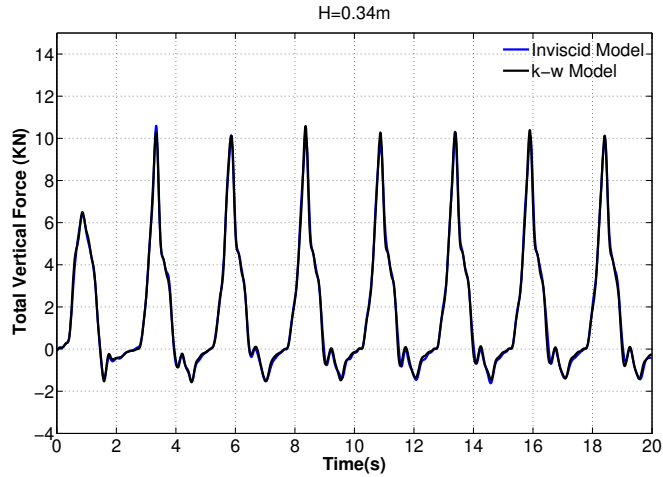


Figure 6.44: Comparison of vertical forces using SST K-Omega model simulation to inviscid model for H=0.34m for Test #6

Figure 6.45 and 6.46 shows comparison of total horizontal and vertical forces for H=0.84m using SST K-Omega Model to simulation results of Test #6 using inviscid model.

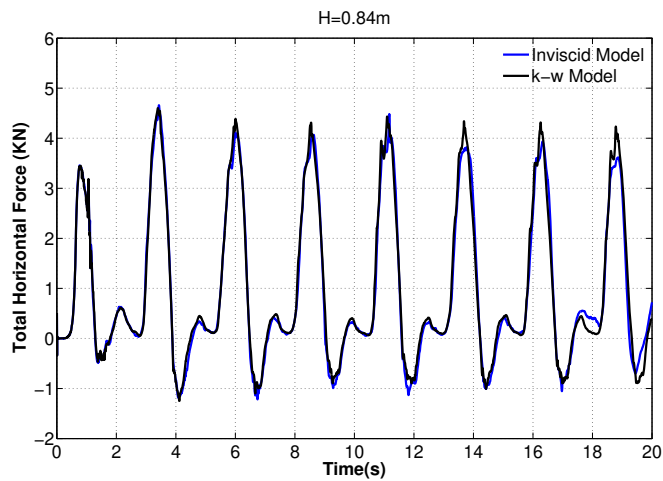


Figure 6.45: Comparison of vertical forces using SST K-Omega model simulation to inviscid model for H=0.84m for Test #6

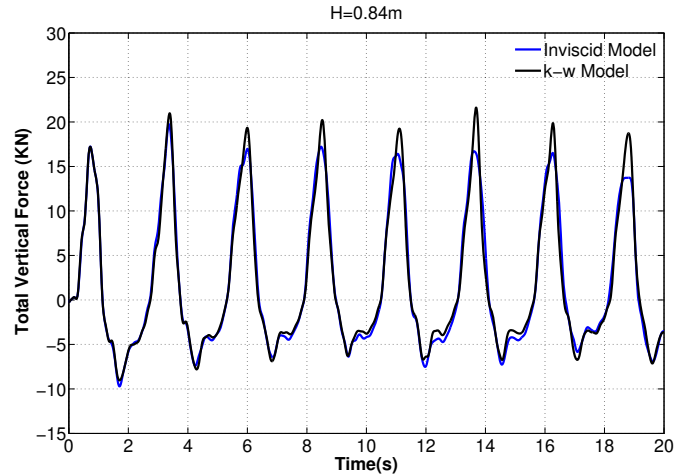


Figure 6.46: Comparison of vertical forces using SST K-Omega model simulation to inviscid model for H=0.84m for Test #6

Simulation results of SST K-Omega model for both horizontal and vertical forces are slightly different than inviscid model. Using SST K-Omega model improved the prediction of horizontal forces by 4 percent and vertical forces by 12 percent. As it is evident in figure 6.46 while for the first two waves inviscid and SST K-Omega model results match, after the second wave, SST K-Omega model seem to predict slightly bigger peaks than inviscid model. This makes the vertical force simulation results closer experimental data.

Overall, the turbulent effects seem to increase as wave height increase. The improvement in vertical force time history predictions for wave height of H=0.84m is big enough to justify more detailed modeling of viscous effects in wave-bridge interaction problem. For future research, it might worth looking into other turbulent models or modify expert properties in SST K-Omega model to improve simulation results even further.

Chapter 7

SCALE EFFECTS ON HYDRODYNAMIC FORCES AND COMPARISON OF SIMULATED FORCES TO AASHTO GUIDELINES

7.1 Scale Effects

This chapter deals with transfer of the previous supercomputer models of wave bridge interaction from laboratory scales to large scales and investigating the effect of scaling on hydrodynamic forces obtained based on Froude similitude law.

In all hydraulic models, geometric, kinematic, and dynamic similarity is important. The geometric scaling is handled by maintaining a single length scale between the prototypes and the models. The kinematic and dynamic scaling is handled by maintaining a single velocity scale ratio between prototypes and models. In hydraulic models, in general its recommended to meet both Froude and Cauchy similitude criteria (Hughes (1993). How ever in reality it is hard to meet both of these criteria at the same time. Therefore usually Cauchy criteria is neglected. In this problem since the role of compressed air might be significant, disregarding Cauchy criteria might cause disproportionately high forces due to compression of air.

The similarity criteria which is commonly used in wave structure interaction problems is usually Froude scaling (as apposed to Reynolds number similitude) because magnitude of inertia forces are significantly bigger than viscous forces. Although Froude similarity generally plays a more important role in gravity surface water flow, effects of turbulence may not be negligible when wave interacts with bridge superstructure.

In this study, numerical simulations were conducted to examine errors in applying Froude similitude law in modeling wave-bridge interaction. This is done by making a prototype bridge by scaling the original bridge analyzed in previous section to exact dimensions of old Escambia Bay Bridge. Based on Froude similitude law the following relationships exist between model and prototype dimensions, velocities and forces:

$$\begin{aligned}
 L_r &= \frac{L_p}{L_m} & (7.1) \\
 V_r &\sim \sqrt{L_r} \\
 t_r &= \frac{L_r}{V_r} \sim \sqrt{L_r} \\
 F_r &= m_r a_r = \rho_r L_r^3 \frac{L_r}{t_r^2} \sim L_r^3
 \end{aligned}$$

where L_r is length ratio, t_r is time ratio, and F_r is force ratio. Applying these formulas to simulation parameters used in previous chapter we get equivalent parameters that need to be used for prototype bridge. Table 7.1 shows an example of relationship between model and prototype simulation parameters for wave height of $H=0.34\text{m}$. Simulation

| Parameter | Model (1:5) | Prototype(1:1) |
|----------------|-------------|----------------|
| Wave Height, H | 0.34 m | 1.7 m |
| Water depth, d | 1.89 m | 9.45 m |
| Wave Period, T | 2.5 s | 5.59 s |

Table 7.1: Example of relationship between model and prototype wave condition

domain is meshed using mesh configuration used in Test #6. Mesh used for prototype bridge simulations scaled to prototype length scales which means mesh used in each mesh region was five times bigger than what was used in simulation done for model bridge in Test #6. Hence the total number of mesh cells used in simulation domain and the number of mesh cells per wave length stayed the same as model bridge. For the time step size, the same time step of $dt=T_p/625$ in Test #6 which in prototype scale bridge simulation is approximately $dt=0.01s$ is used to ensure simulation accuracy. There is no experimental data available for the prototype model, however the accuracy of simulation could be checked by monitoring residuals and convergence as the simulation progress. These concepts are explained in detail in chapter 5. Simulations for model bridge were ran for 15 seconds which include the interaction of 3 waves with prototype bridge superstructure. Figures 7.1 and 7.2 show the average of horizontal and vertical forces calculated for 3 waves interacting with prototype bridge superstructure (blue discrete horizontal line) compared to average of horizontal and vertical forces in model bridge adjusted to prototype scale using Froude similitude law (black discrete horizontal line). As it is evident in these two figures, the average of horizontal and vertical forces in prototype bridge match the average of horizontal and vertical forces in model bridge adjusted to prototype scale using Froude similitude law. Even for cases where slamming forces were present figure 7.2 shows that Froude similitude law works well for scaling both horizontal and vertical forces. It is also interesting to note that similar to model bridge, the slamming oscillations in vertical force time histories exist only for some wave heights not for all. These include wave heights of $H=1.7m$ and $H=2.15m$ (corresponding to $H=0.34m$ and $H=0.43m$ in model bridge). Also, similar to model bridge simulations in previous chapter, horizontal force time history does not show any slamming oscillations.

Figures 7.3 to 7.6 shows some simulation snapshots of wave-bridge interaction for prototype bridge for wave height of $H=4.2\text{m}$. Its is meaningful to compare these snapshots to snapshots of Test #6 in figure 6.33. VOF scenes for prototype bridge for $H=4.2\text{m}$ shown in figure 7.3 is very similar to VOF scenes for model bridge in Test #6. It is important to note that using Froude similitude relationships, $t=1.1\text{s}$ in prototype bridge simulations is equivalent to $T=0.5\text{s}$ in model bridge simulations shown in previous chapter.

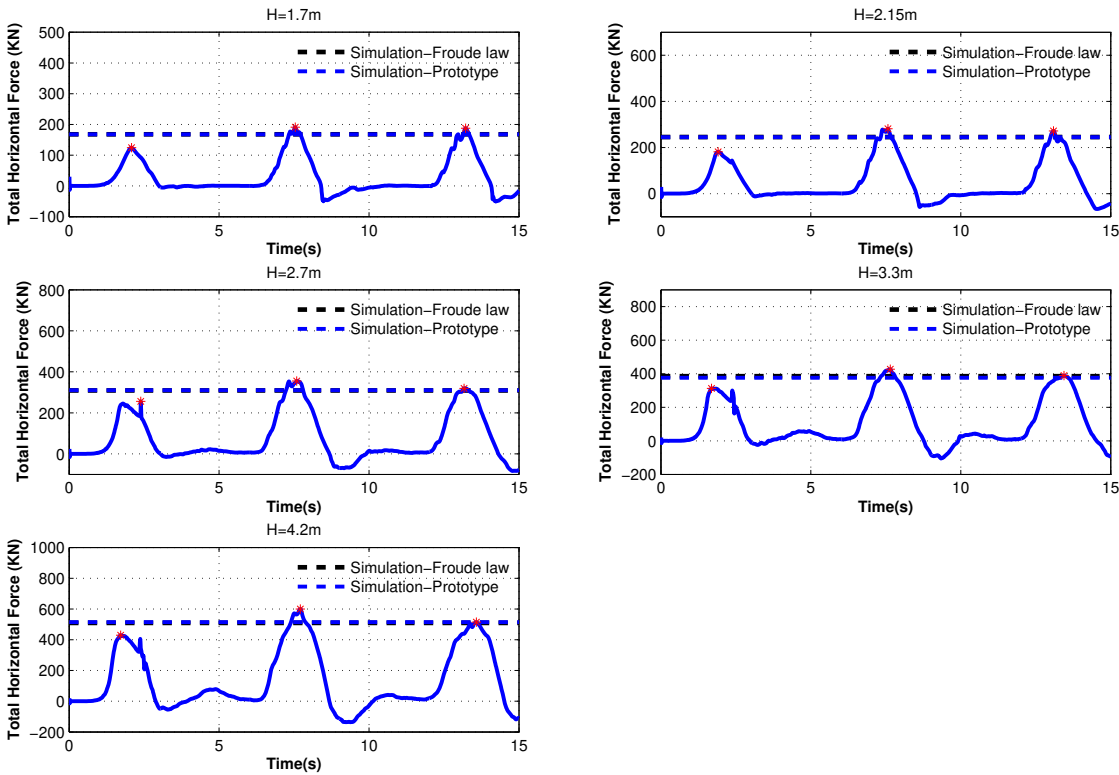


Figure 7.1: Horizontal force simulation results for prototype bridge vs. results archived from model bridge using Froude similitude law

It is also possible to compare maximum values for pressure, horizontal and vertical velocity in model and prototype bridge simulations at different simulation instances.

For example at $t=1.1\text{s}$ (before wave hit the bridge superstructure), maximum pressure in simulation domain for prototype bridge is about 104430 Pa while maximum pressure in simulation domain for model bridge is about 21083 Pa . The ratio of maximum pressure in prototype bridge simulation to maximum pressure in model bridge simulation according to Froude similitude law should be 5. In this specific instance the ratio is 4.95. At $t=3.8\text{s}$ (while wave interacts with bridge superstructure) this ratio is 4.99.

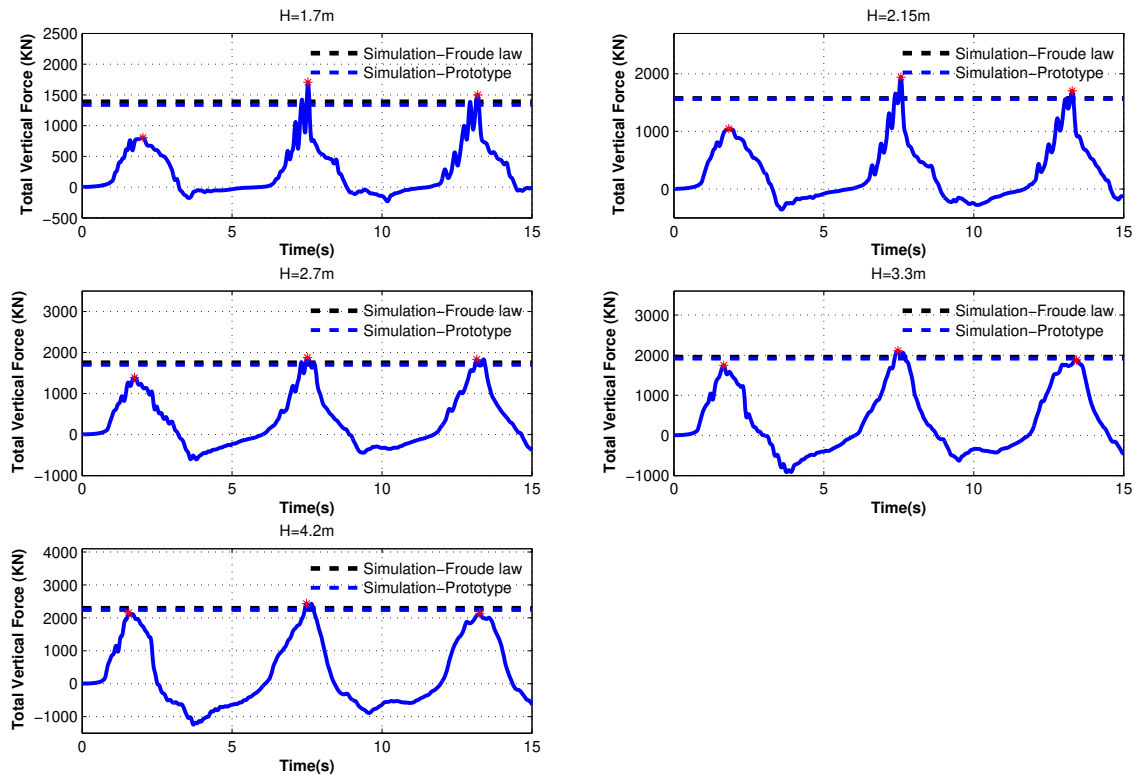


Figure 7.2: Vertical force simulation results for prototype bridge vs. results archived from model bridge using Froude similitude law

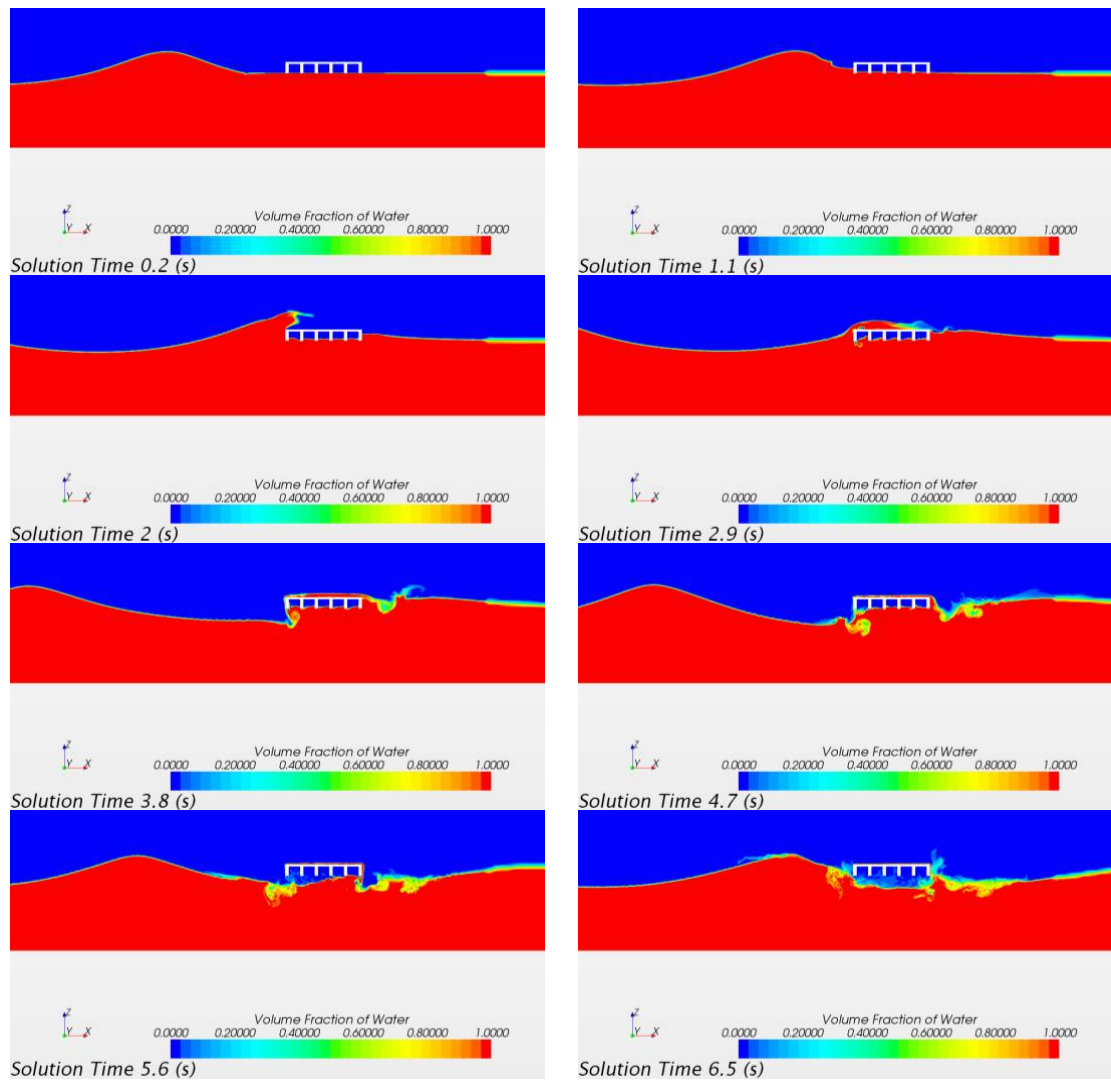


Figure 7.3: Volume of fluid (VOF) scenes for $H=4.2\text{m}$ wave interacting with prototype bridge

At $t=1.1\text{s}$ and $t=3.8\text{s}$ the ratio of maximum horizontal velocity in prototype bridge to model bridge is 2.05 and 1.97 respectively. According to Froude similitude law this ratio should be $\sqrt{5} = 2.24$.

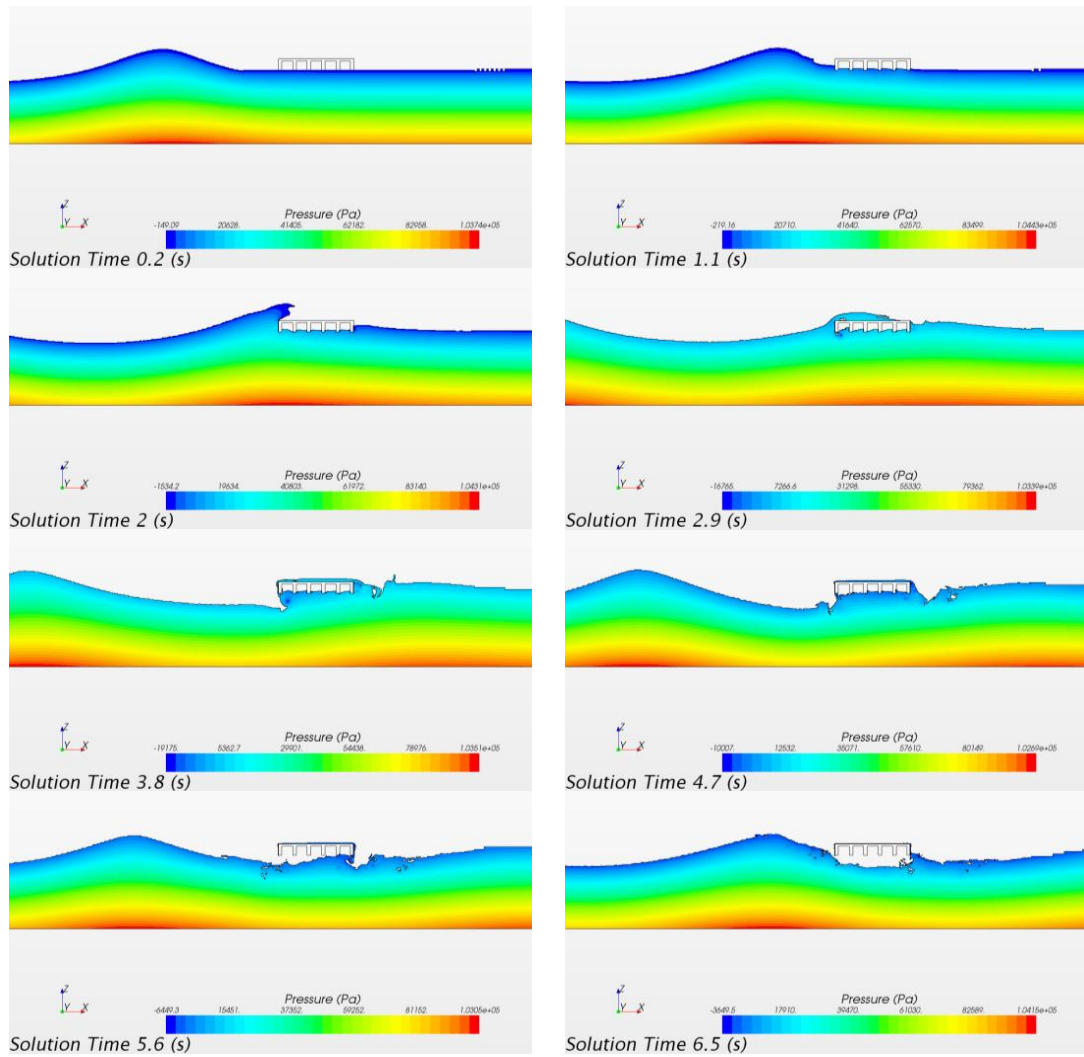


Figure 7.4: Pressure scenes for H=4.2m wave interacting with prototype bridge

At $t=1.1s$ and $t=3.8s$ the ratio of maximum vertical velocity in prototype bridge to model bridge is 2.27 and 2.84 respectively. According to Froude similitude law this ratio should be $\sqrt{5} = 2.24$.

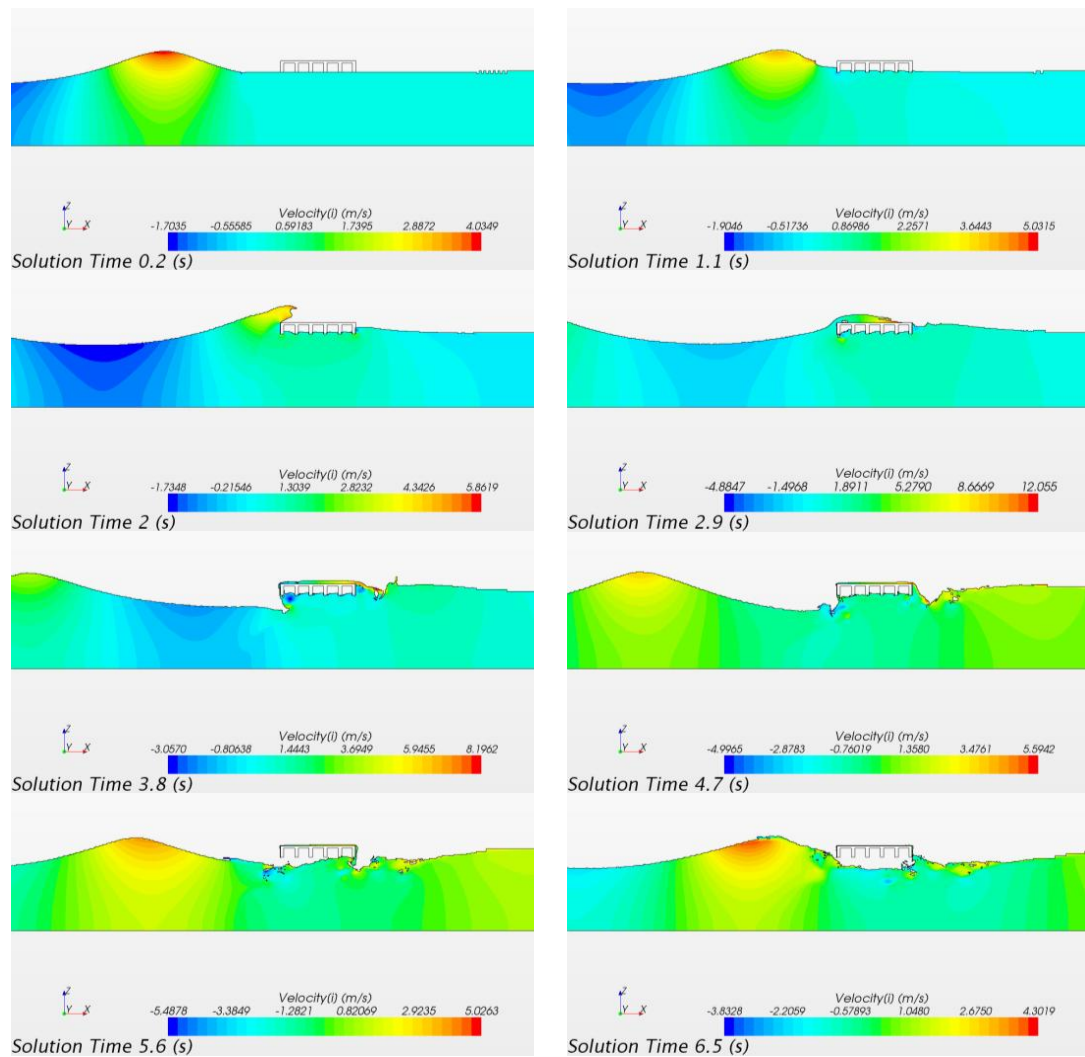


Figure 7.5: Velocity magnitude in horizontal direction for $H=4.2\text{m}$ wave interacting with prototype bridge

As we saw, the relationship between maximum pressure in simulation scenes in model and prototype bridge follows Froude similitude law very closely. However the maximum velocity in model and prototype bridge do not closely follow the Froude similitude law.

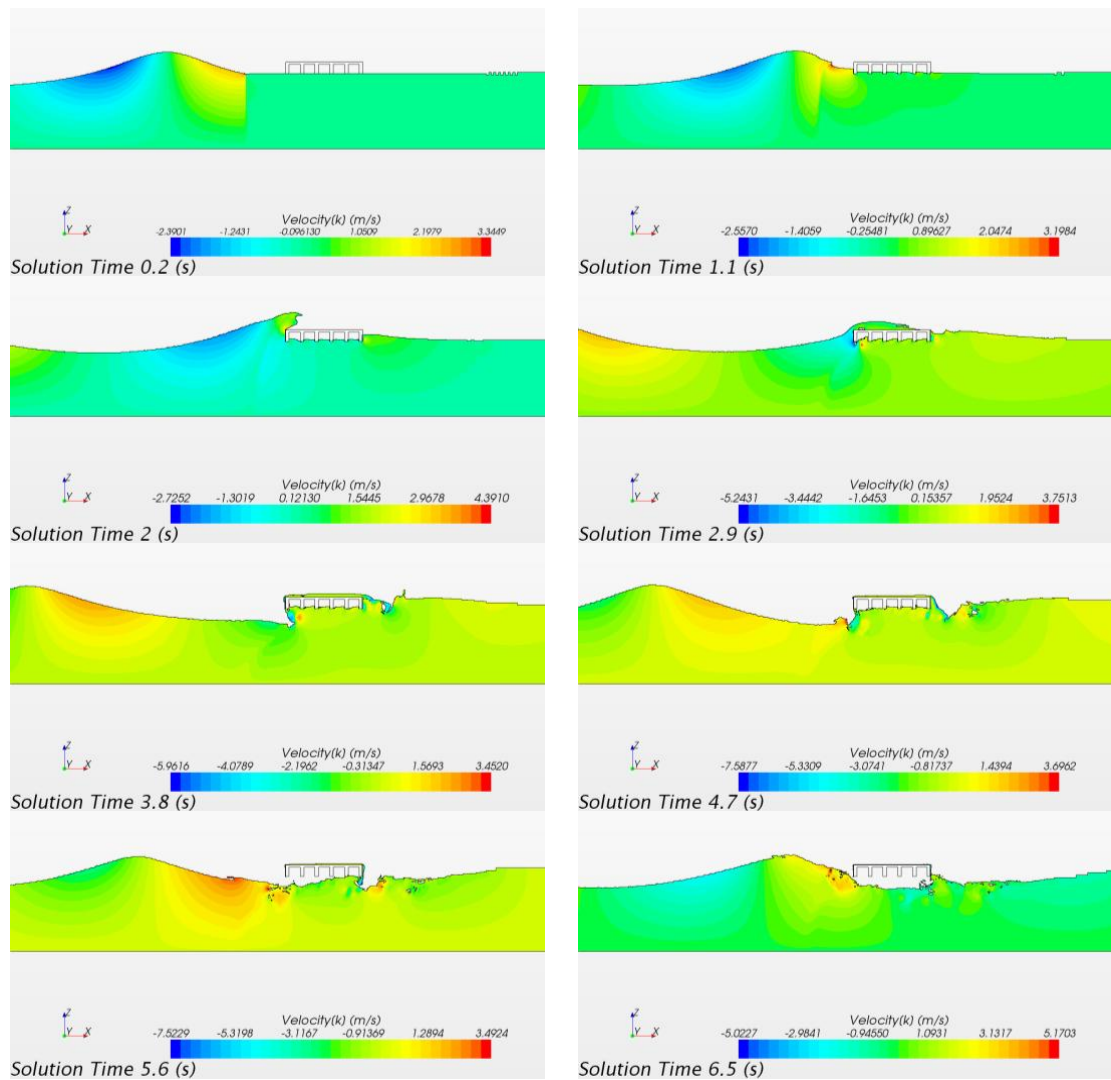


Figure 7.6: Velocity magnitude in vertical direction for $H=4.2\text{m}$ wave interacting with prototype bridge

This is expected because the maximum pressure always happens at the bottom of simulation domain under the wave profile while maximum horizontal and vertical velocities happen near free surface close to complex wave-bridge interaction. Also in general, its more challenging to accurately predict velocities compared to pressures and forces

since they are more sensitive to simulation parameters such as mesh size time step and numerical models. Nevertheless since hydrodynamic forces applied to prototype bridge matched the ones calculated from model bridge using Froude similitude law, we can confidently use Froude similitude law to calculate hydrodynamic forces applied to prototype bridge superstructure using the results for model scale bridge superstructure.

7.2 AASHTO Guidelines

Recently developed AASHTO guidelines AASHTO (2008) for wave forces on coastal bridges are compared to the previously simulated hydrodynamic forces for both model and prototype bridges. The equations in the guideline require prototype scale inputs, as a result, the bridge specimen geometry, water depths, and wave conditions are scaled to prototype dimensions using Froude scaling explained in previous section. These values are shown in table 7.1 for wave height of $H=0.34\text{m}$ (in model scale) and its corresponding prototype values. The dimensions of the prototype bridge are shown in table 5.1. The maximum quasi-steady horizontal and vertical forces in kip/ft, including the effect of variable air entrapment according to the guideline is calculated using following equations:

$$F_{H-MAX} = F_{H-MAX}^* e^{-3.18+3.76e^{(-\frac{w}{\lambda})} - 0.95[\ln(\frac{\eta_{max}-z_e}{d_b+r})]^2} \quad (7.2)$$

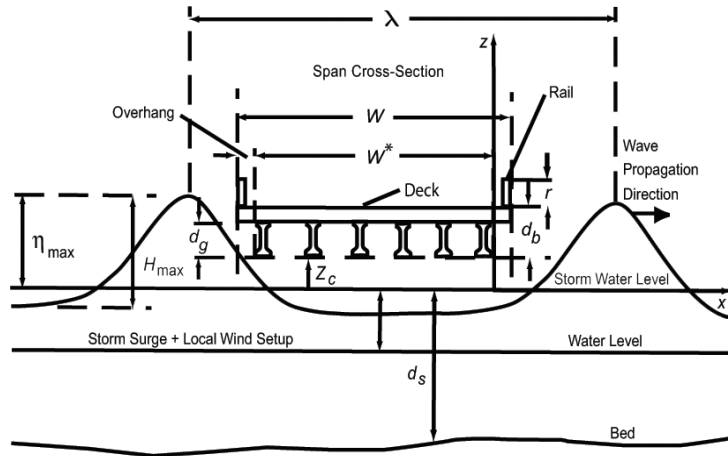
$$F_{V-MAX} = \gamma_w \bar{W} \beta \left(-1.3 \frac{H_{max}}{d_s} + 1.8 \right) [1.35 + 0.35 \tanh(1.2(T_p) - 8.5)] \quad (7.3)$$

$$(b_0 + b_1 x + \frac{b_2}{y} + b_3 x^2 + \frac{b_4}{y^2} + \frac{b_5 x}{y} + b_6 x^3)(TAF)$$

These complicated equations come from extensive studies by Sheppard and Marin (2009) and the laboratory data from 1/8 scale model wave tank tests at the university

of Florida and field data from I10 Escambia Bay Bridges damaged during Hurricane Ivan AASHTO (2008). The parameters used in these equations are explained in full detail in section 6.1.2.2 of this guideline. Some of the variable used in these equations are shown in figure 7.7. In the above equations, γ_w is unit weight of water taken as $0.0064 \text{ kip}/\text{ft}^3$, \bar{W} is some function of wave length λ , maximum wave height H_{\max} , and distance from storm water level to the bottom of bridge girder Z_c . β is some function of distance from the storm water level to design wave crest η_{\max} , Z_c , and girder height+bridge thickness d_b . y is some function of \bar{W} and λ . x is some function of H_{\max} and λ . Variables b_0 to b_6 are curve fitting coefficients that are only a function of d_b .

Equation 7.3 accounts for the air entrapment through Trapped Air Factor (TAF). TAF is used for reduction in the buoyancy component of the vertical quasi-steady force due to partial or complete venting of the air between bridge girders and diaphragm. The effect is to alter the buoyancy force, which only has a vertical component, thus the TAF is only multiplied times the vertical quasi static force AASHTO (2008). The guideline coefficients for AASHTO type III girders were used and maximum trapped Air Factor (TAF) is calculated based on a diaphragm height of 4/5 times the girder height. The resulting forces were then reduced to model scale and plotted with the measured forces from experimental data . The guideline also has an empirical equation for calculation of slamming forces.



- Water Level = mean sea level if storm surge includes astronomical tide
 = mean higher high water level if astronomical tide not included in surge
- η_{\max} = wave crest height above storm water level
- H_{\max} = maximum wave height
- λ = wave length
- d_s = storm water depth at the bridge
- d_b = girder height + deck thickness
- d_g = girder height
- Z_c = positive or negative distance from storm water level to bottom of girder
- r = rail height
- W = deck width

Figure 7.7: Nomenclature in equation 7.3 and 7.2 adapted from AASHTO (2008)

The slamming force occurs when the air-water interface impacts the structure. Vertical slamming forces exist when the bottom of the structure is located above the trough of the wave and below the wave crest. An empirical equation in the guideline is a function of the structure clearance and wave parameters using laboratory data obtained from experiments conducted at the university of Florida. Slamming force is calculated as follows:

$$F_s = A\gamma_w H_{\max}^2 \left(\frac{H_{\max}}{\lambda} \right)^B \quad (7.4)$$

In the following section, we compare the magnitude of horizontal and vertical quasi-steady forces calculated by numerical model to magnitude of horizontal and vertical

quasi-steady forces ($F_h(\text{max})$ and $F_v(\text{max})$) calculated by the guideline. Quasi-steady forces for numerical results are obtained by filtering out frequencies over 7Hz from numerical results (7Hz was the highest frequency witnessed in force time histories in experimental data available from Oregon State University Bradner and Cox (2008)). Also, we compare the magnitude of total vertical forces calculated by numerical model to magnitude of total vertical forces calculated by guideline. Total vertical force in guideline is obtained by adding quasi-steady vertical force ($F_v(\text{max})$) calculated by equation 7.3 to slamming force F_s calculated by equation 7.4.

7.3 Comparison of Simulated Wave Forces to AASHTO Guidelines

In this section hydrodynamic forces calculated using AASHTO guidelines explained in previous section are compared with numerical simulation results for both model and prototype bridge superstructures. The mesh and time step size used in these numerical simulations are the same ones used in Test #6 explained in chapter 6. Wave length is calculated assuming linear dispersion. The guideline coefficients for AASHTO type III girders are used and the maximum Trapper Air Factor was calculated using diaphragm height of 4/5 times the girder height (this means using $\%Air = 0.8$). Minimum Trapped Air Factor was calculated assuming $\%Air = 0$. Where $\%Air$ is a variable used in calculation of trapped air factor (TAF). Figure 7.8 shows comparison of forces calculated by numerical model to forces calculated using AASHTO guidelines for model bridge superstructure. Horizontal wave forces for the range of wave heights simulated, compare reasonably well with the maximum horizontal forces ($F_h(\text{max})$) calculated using guideline equations. The total vertical force ($F_v(\text{max})+F_s$) predicted by the guidelines was larger than the measured vertical force for almost every wave height except H=0.34m.

Guideline slightly under predicts the magnitude of total vertical force for $H=0.34\text{m}$. For other wave heights the maximum vertical force predicted by guideline is conservative.

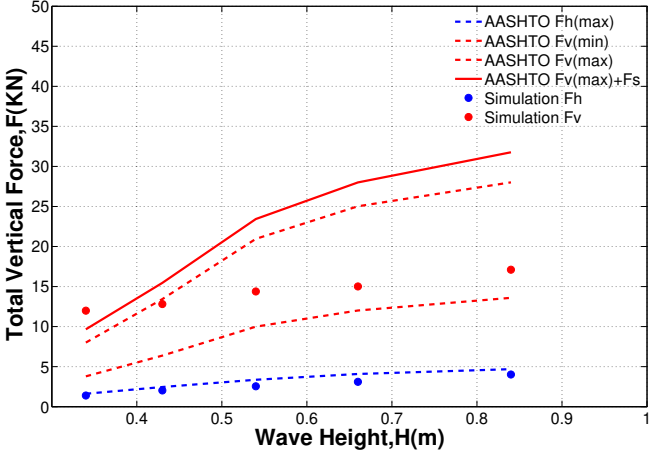


Figure 7.8: Comparison of simulated forces for model bridge to AASHTO guideline

Figure 7.9 shows comparison of quasi-steady forces for model bridge to forces calculated using AASHTO guidelines. As expected, since simulated horizontal force time histories did not contain any slamming oscillations, quasi-steady horizontal forces were exactly the same as total horizontal forces shown in figure 7.8. Therefore they compare well with AASHTO guideline predictions for horizontal forces. Figure 7.9 shows that simulated quasi-steady vertical forces fall within predictions of guideline based on minimum and maximum TAF used in equation 7.1. However for all wave heights except $H=0.34\text{m}$ and $H=0.43\text{m}$, guideline predictions of quasi-steady vertical forces based on maximum TAF are too conservative. As the wave height increase the magnitude of simulated quasi-steady vertical force gets closer to the quasi-steady vertical force calculated based on minimum TAF.

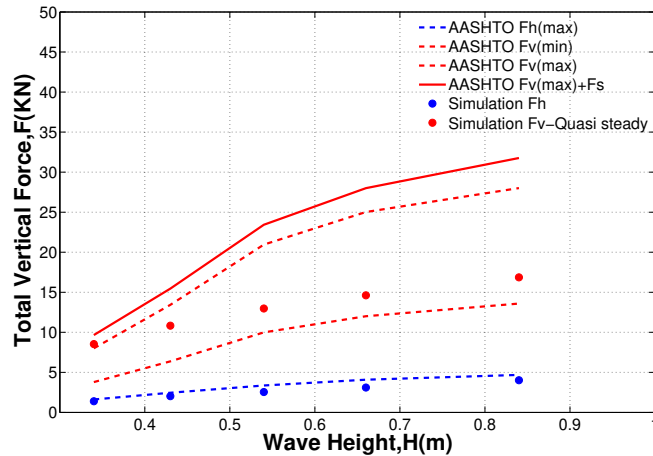


Figure 7.9: Comparison of simulated quasi-steady forces for model bridge to AASHTO guideline

Figure 7.10 shows the comparison of simulated total horizontal and vertical forces for the prototype bridge to forces calculated using AASHTO guidelines. As it is seen, like model bridge, horizontal forces are predicted with reasonable accuracy.

The simulated vertical forces for prototype bridge fall within the range of maximum and minimum vertical forces predicted by guideline. Guideline slightly under predicts the magnitude of total vertical force for $H=1.7\text{m}$ but for all other wave heights guideline prediction are conservative.

Figure 7.11 shows comparison of simulated quasi-steady forces for prototype bridge to forces calculated using AASHTO guidelines. As expected filtering did not have any effect on horizontal forces because they did not contain any high frequency slamming oscillation. Therefore quasi-steady horizontal forces simulated are in very good agreement with guideline predictions for prototype bridge.

Vertical quasi-steady forces simulated for prototype bridge also fall within guideline predictions. For $H=1.7\text{m}$ guideline prediction based on maximum trapped air factor calculated using $\%Air = 0.8$ is very close to simulated total vertical force. As the wave

height increase, simulated total vertical force becomes closer to guideline prediction based on $\%Air = 0.0$.

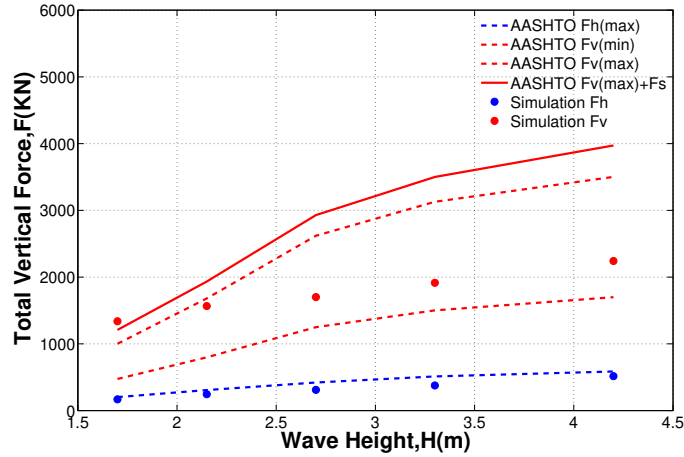


Figure 7.10: Comparison of simulated forces for prototype bridge to AASHTO guideline

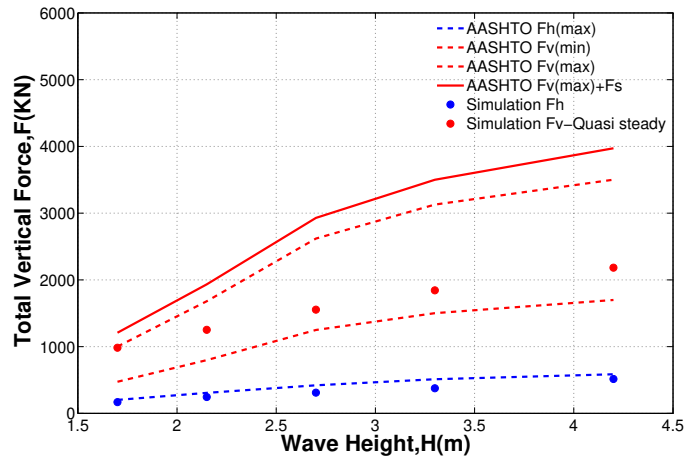


Figure 7.11: Comparison of simulated quasi-steady forces for prototype bridge to AASHTO guideline

To sum up, AASHTO guideline was well capable of predicting total horizontal forces applied to bridge superstructure for both model and prototype bridges. Magnitude of vertical forces calculated using guideline equations are shown to be very sensitive to the value chosen for trapped air factor (TAF) in equation 7.3. Simulated forces for both model and prototype bridge fell within guideline predictions for the range of wave heights simulated based on maximum and minimum trapped air factor. Except for forces calculated for wave height of $H=0.34\text{m}$ ($H=1.7\text{m}$ in prototype bridge simulations) inclusion of slamming force F_s in total vertical force was shown to be too conservative. In addition since slamming force was not present in any experimental data available from Oregon State University, designers should use their judgment and consider structural respond when deciding whether or not to include the slamming force in the design load, as the quasi-steady force alone may be sufficient for most applications.

,

Chapter 8

RETROFITTING OPTIONS AVAILABLE FOR COASTAL BRIDGES EXPOSED TO WAVES

To avoid loss of coastal bridges from Hurricane surge wave forces if possible the best way is to elevate them sufficiently to allow the surge/surface wave to pass under the bridge superstructure. However, if this is too costly and/or the bridge is already in existence, it appears that it should be very feasible to connect the bridge components in a manner, or to take retrofit action, to avoid having the hurricane surge/surface wave dump the superstructure into the water. One effective way proposed was to improve venting of underneath regions of bridge superstructure to reduce buoyant forces. This can be done by selective deck coring and the creation of large holes in span end diaphragms to allow exchange of trapped air between spans.

In this section two retrofitting options are investigated. These two options are recommended by AASHTO guidelines and several other reports including Sawyer (2008). These options are:

- Airvents in bridge deck
- Airvents in bridge diaphragm

The results of using above retrofitting options to wave bridge interaction problem is presented in the following sections.

8.1 Airvents in Bridge Deck

The hole size should be chosen carefully so that it does not disrupt the bridge structural integrity. The vent hole should also be able to provide enough venting capacity to vent out the trapped air under the bridge in a timely manner.

In option 1, 5cm hole is cut through the deck of bridge superstructure. This is shown in figure 8.1. Simulations are done using the same mesh and time step used in Test #6 from previous chapter. Figure 8.2 shows VOF scene for $H=0.84\text{m}$.

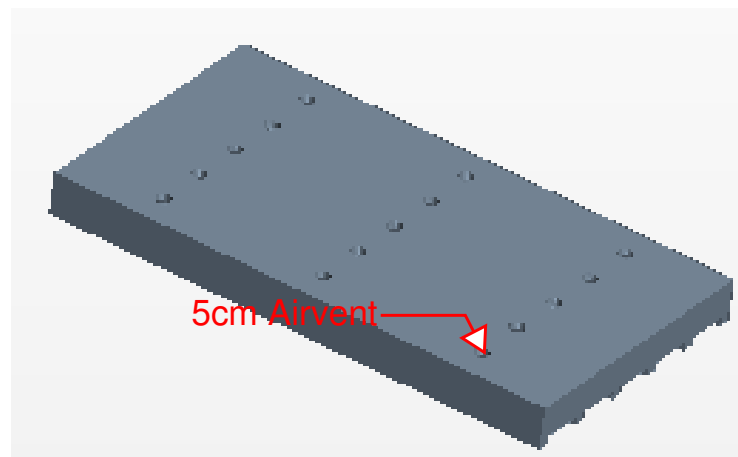


Figure 8.1: Retrofit option 1

Comparing VOF scene for retrofitted bridge to VOF scene for Test #6 we see that the only difference is that in the retrofitted bridge the water proceeds and fills up the cavities between bridge girders and diaphragm more than un-retrofitted bridge, therefore effectively reduce buoyancy forces applied to bridge superstructure. This means the water touches the bottom of bridge deck in retrofitted bridge while there is a layer of air between free surface and bottom of bridge deck in bridge without airvents.

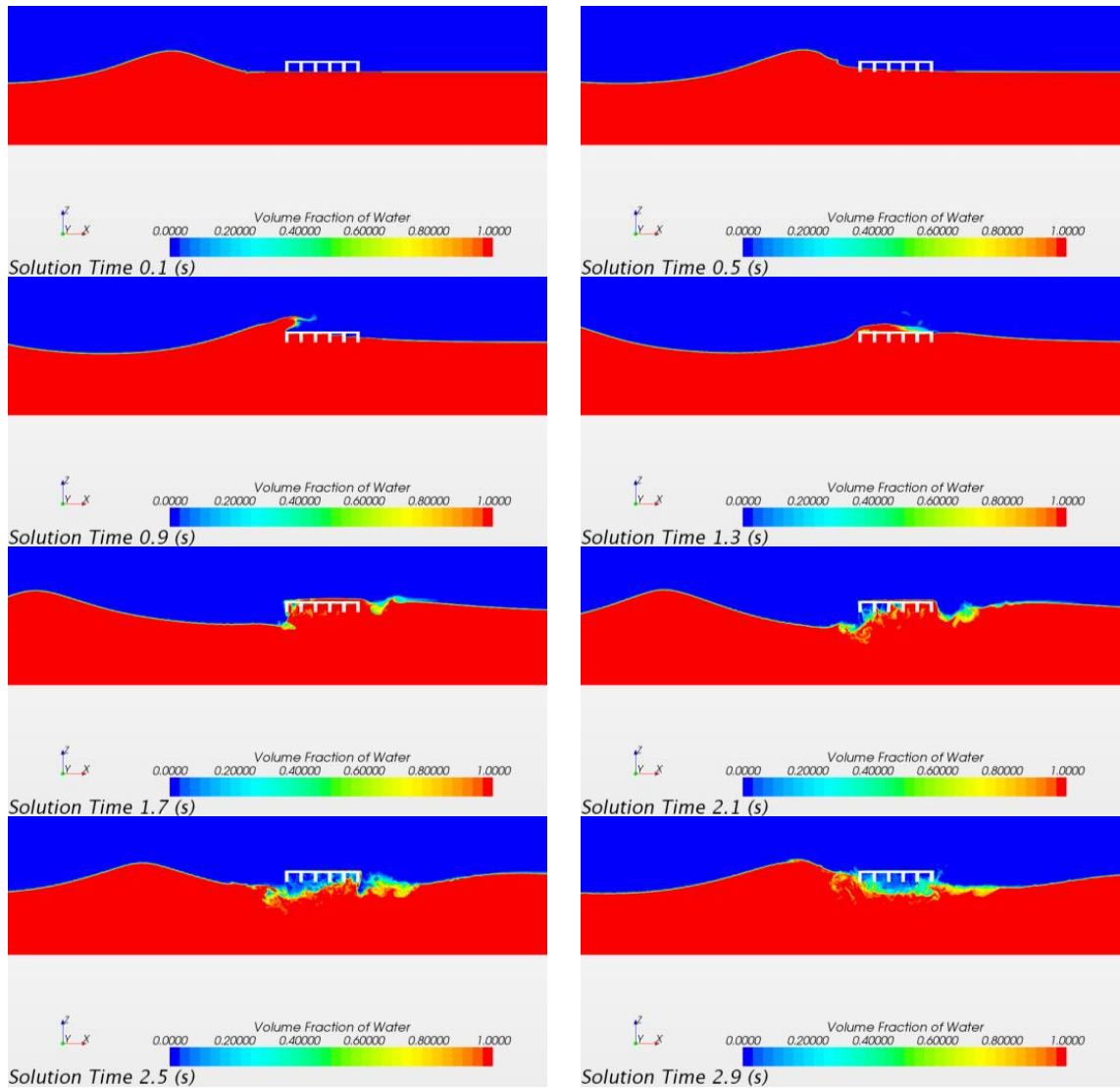


Figure 8.2: Volume of fluid (VOF) scene for option 1

Figure 8.3 shows how the bridge becomes fully inundated for $H=0.84\text{m}$. The fact that wave overtops the bridge and water covers surface of deck reduces capacity of airvents over bridge deck because they are clogged by water on top of bridge deck.

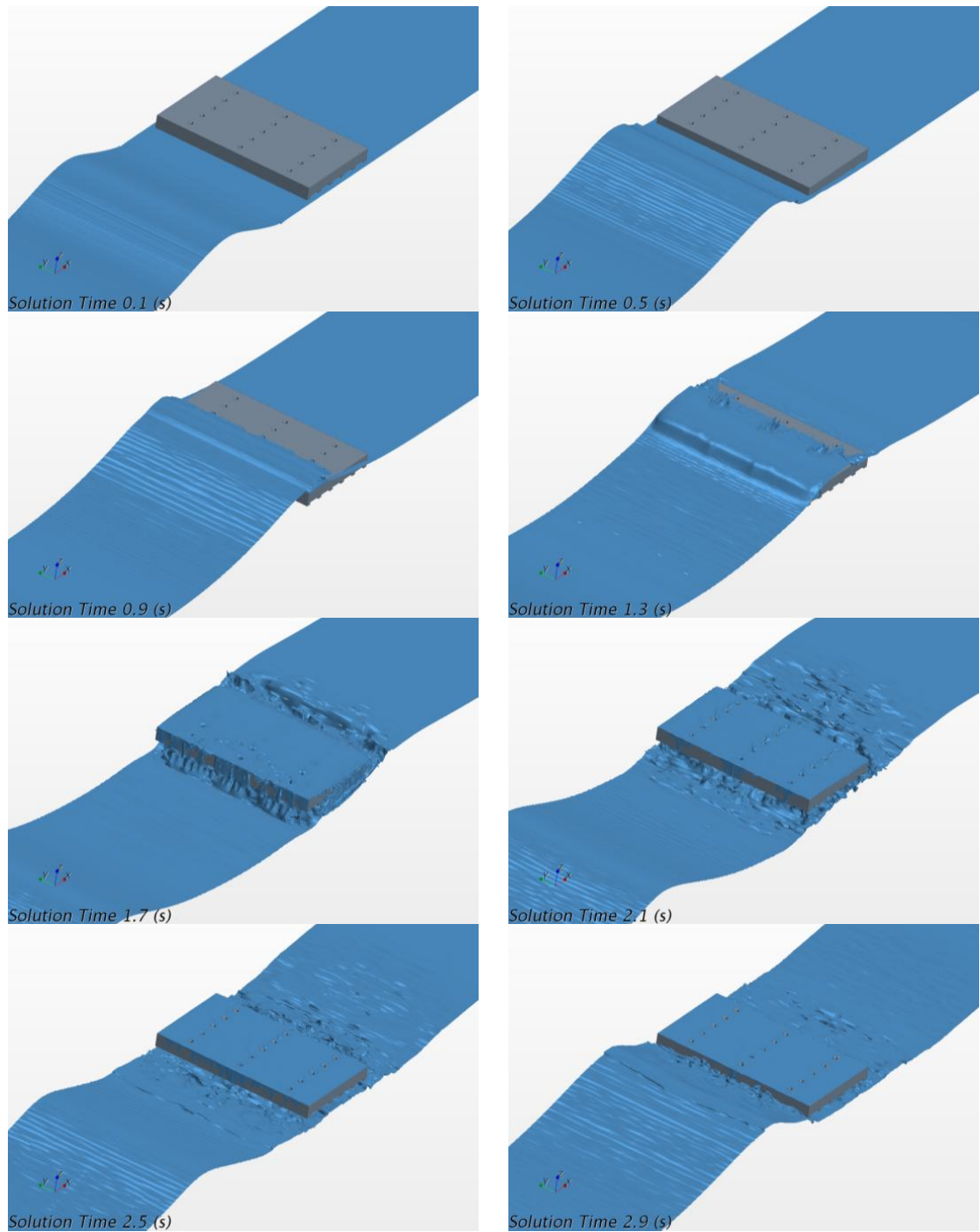


Figure 8.3: 3D iso surface for option 1

Comparison of simulations before and after adding the vent hole to bridge deck (option 1), shows that airvents can be very effective in reducing vertical hydrodynamic forces for some wave heights. As it is seen in figure 8.6 airvents in bridge deck have a two fold effect on total vertical hydrodynamic forces: they reduce the magnitude of slamming oscillation and they decrease the overall quasi-steady vertical force. Usage of 5cm air vent in bridge deck causes about 60 percent reduction in total vertical wave forces for $H=0.34\text{m}$. However as wave height increase the efficacy of airvents in reducing hydrodynamic forces decrease. For example, for $H=0.84\text{m}$ airvents reduce total vertical force by only 17 percent (figure 8.7). This may be because of one of the following reasons or combination of both:

- As wave height increase water particle velocities also increase. This means cavities under the bridge are filled much faster and there may be not enough time for 5cm airvent to fully vent out the air between bridge girders and diaphragms. This means some air will remain between bridge girders and diaphragm therefore the vertical forces do not decrease for bigger waves as much as they decrease for smaller waves.
- Another reason for airvents not being effective for bigger waves could be the water overtopping the bridge deck. Water covering the surface of bridge deck may clog the vents and prevent the air from venting out of deck air vents.

Option 1 retrofit also influence total horizontal forces applied to bridge superstructure. While for $H=0.34\text{m}$ airvents reduce total horizontal forces by 15 percent (figure 8.4) , They seem to slightly increase horizontal forces for other wave heights. For example, for $H=0.84\text{m}$ (figure 8.5) total horizontal forces increase by 7 percent.

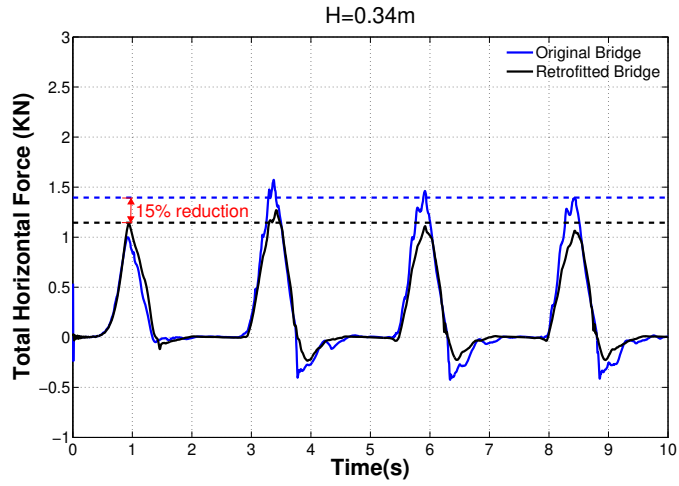


Figure 8.4: Effect of option 1 retrofit on horizontal force time history for H=0.34m

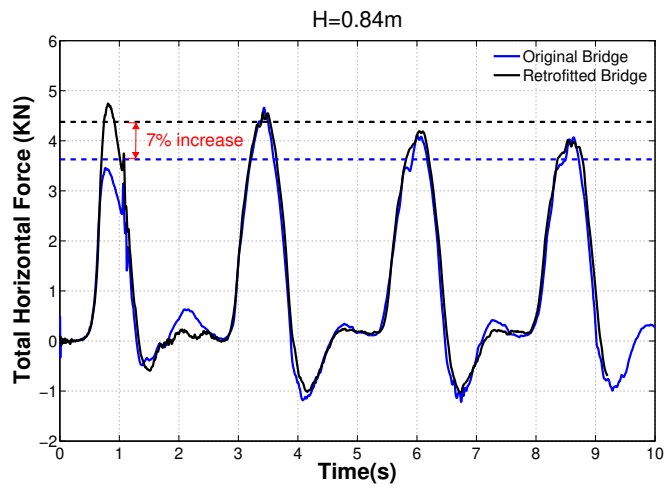


Figure 8.5: Effect of option 1 retrofit on horizontal force time history for H=0.84m

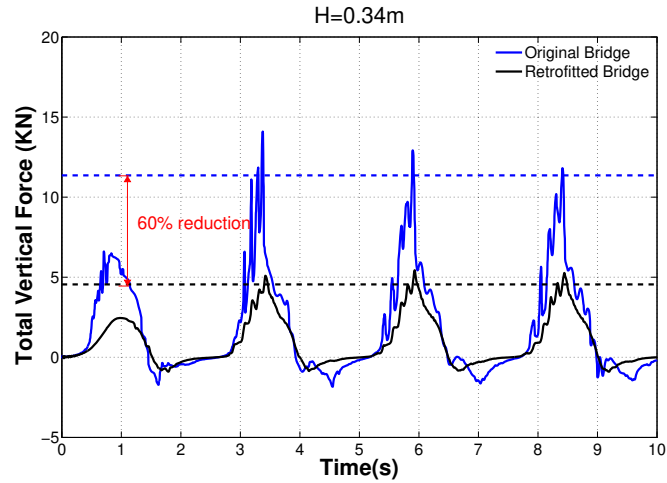


Figure 8.6: Effect of option 1 retrofit on vertical force time history for H=0.34m

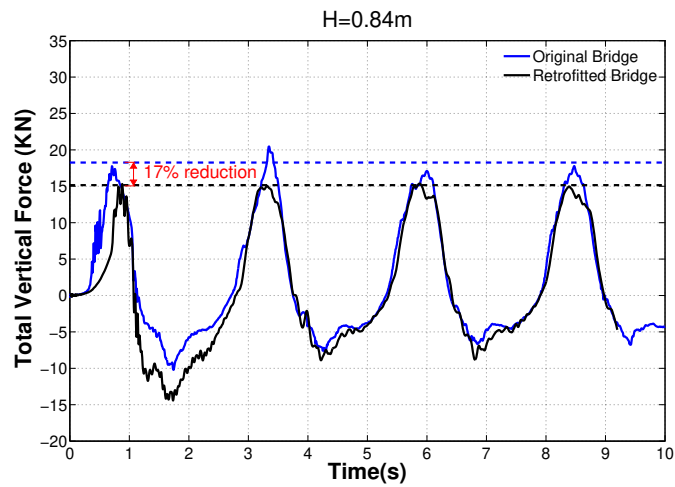


Figure 8.7: Effect of option 1 retrofit on vertical force time history for H=0.84m

overall air vents in bridge deck are effective in reducing both horizontal and vertical wave forces. However their efficacy depends on the wave height hitting the bridge superstructure and the size of vent used. They have the advantage of serving as drainage holes and the disadvantage that the water coming out of these holes may make the bridge surface wet. It is also observed that during wave interaction with bridge, air exits the

holes with a very high velocity reaching about 40 m/s (for $H=0.84\text{m}$). This is something that needs to be considered as it might cause problems for traffic passing over the bridge superstructure. The effect of air vents on horizontal and vertical forces for different wave height for option 1 retrofit is shown in figure 8.8 and 8.9. As it is evident in these figures the option 1 retrofit reduces vertical forces up to 62 percent for $H=0.34\text{m}$. As the wave height increase, the efficacy of air vents decrease reaching 17 percent for $H=0.84\text{m}$. Retrofit option 1 also influences horizontal hydrodynamic forces. For $H=0.34\text{m}$ air vents reduce horizontal force by 18 percent whereas for other wave heights the horizontal forces slightly increase. For example for $H=0.84\text{m}$, retrofit option 1 increase total horizontal force by 9 percent. The increase in horizontal force in retrofitted bridge is likely due to increase in areas of bridge superstructure that is exposed to horizontal wave momentum as a result of water penetrating the cavities between bridge girders and diaphragms.

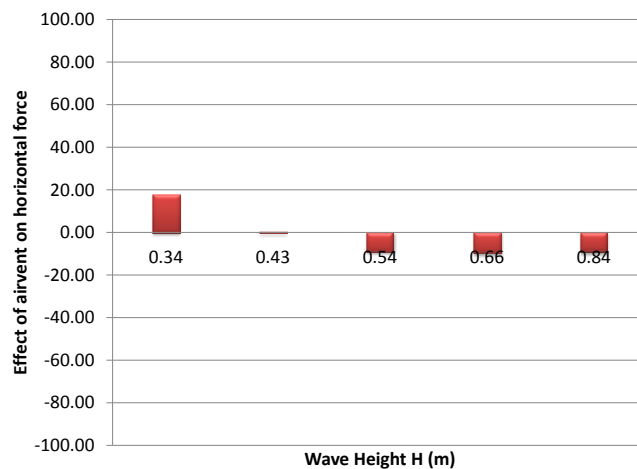


Figure 8.8: Effect of option 1 retrofit on horizontal force for various wave heights

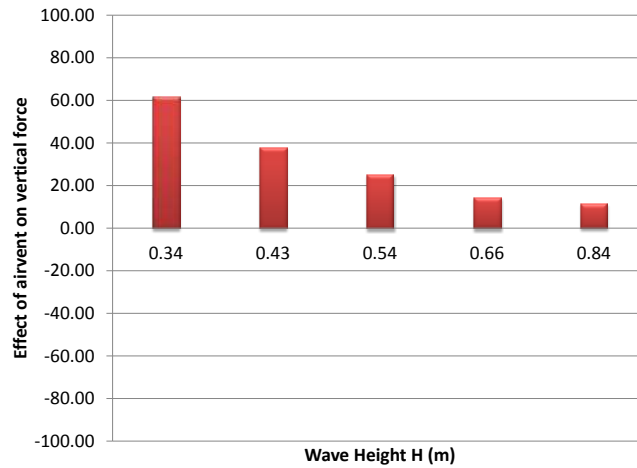


Figure 8.9: Effect of option 1 retrofit on vertical force for various wave heights

The reduction in efficacy of airvents may be overcome if larger vents are used and/or guard rail is used to prevent the water from overtopping and clogging the vent holes. However care must be taken to make sure not to disrupt bridge structural integrity by using air vents that are too big in diameter.

8.2 Airvents in Bridge Diaphragm

In this section the efficacy of the airvents in bridge diaphragm are evaluated. Airvents in bridge diaphragm might be more attractive to bridge designers and maintenance staff because the water will not leak to the surface of the bridge deck from airvents. Bridge diaphragms provide torsional rigidity to bridge superstructure and they are less structurally significant than bridge girders therefore vent holes are cored in bridge diaphragm instead of bridge girder. Figure 8.10 shows 5 cm diameter airvents cored in bridge diaphragm.

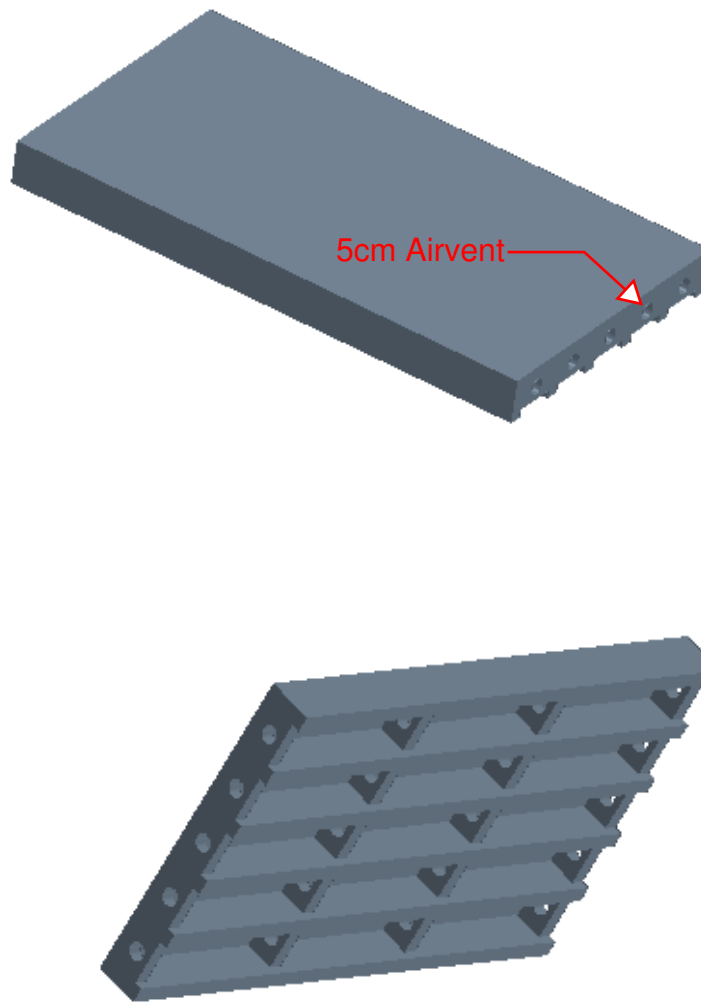


Figure 8.10: Retrofit option 2

Figures 8.11 through 8.14 show the effect of retrofit option 2 on horizontal and vertical forces for $H=0.34\text{m}$ and $H=0.84\text{m}$ respectively. Similar to retrofit option 1, airvents in bridge diaphragm are effective in reducing hydrodynamic forces applied to bridge superstructure. For $H=0.34\text{m}$ the total vertical force reduced by 37 percent where as for $H=0.84\text{m}$ the total vertical force reduced by only 8 percent. This shows that retrofit option 2 is not as effective as retrofit option 1 in reducing total vertical forces.

However retrofit option 2 performs slightly better than retrofit option 1 for horizontal forces because it causes less increase in horizontal forces compared to retrofit option 1. Retrofit option 1 as it is seen in figure 8.15 reduce the total horizontal force for $H=0.34\text{m}$ by 17 percent and increase total horizontal forces for $H=0.66\text{m}$ only by 3 percent which is almost negligible.

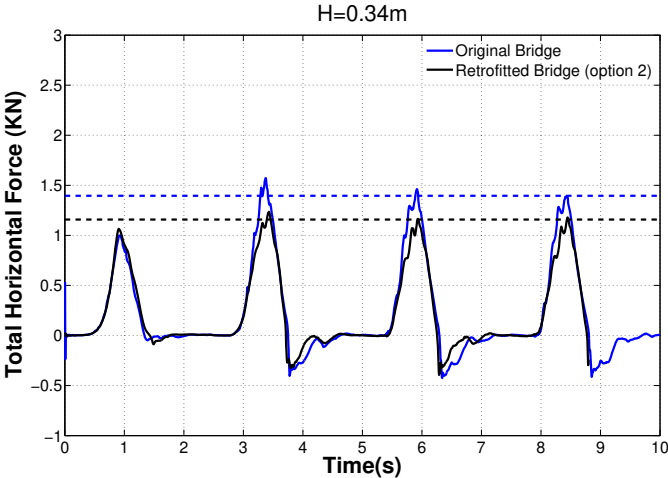


Figure 8.11: Effect of option 2 retrofit on horizontal force time history for $H=0.34\text{m}$

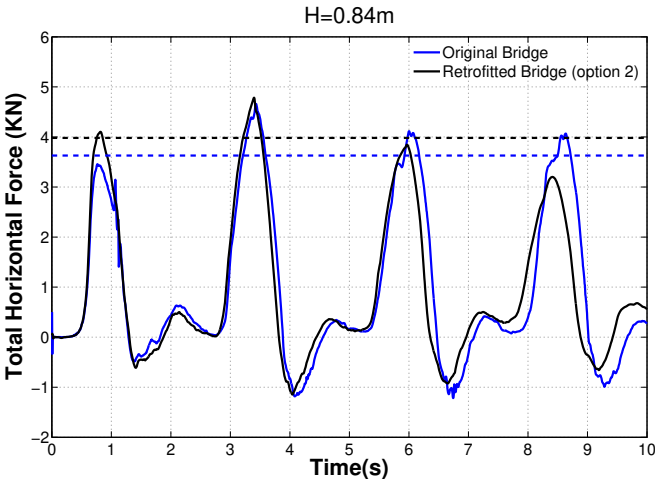


Figure 8.12: Effect of option 2 retrofit on horizontal force time history for $H=0.84\text{m}$

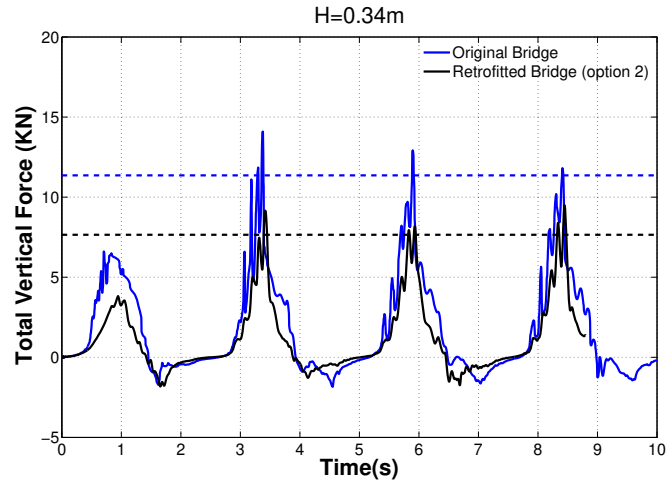


Figure 8.13: Effect of option 2 retrofit on vertical force time history for H=0.34m

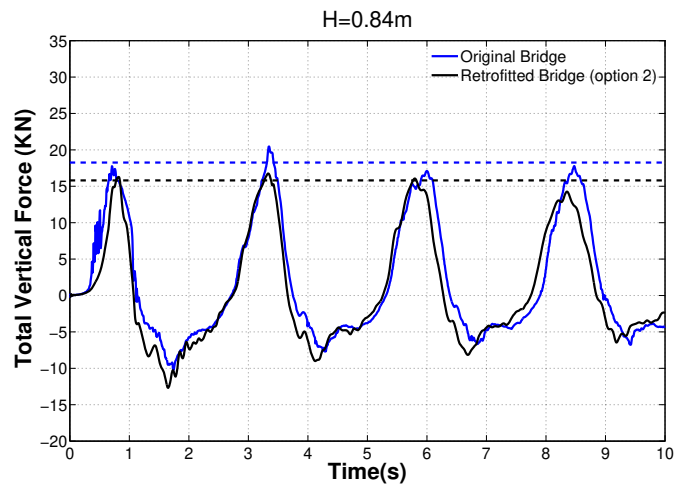


Figure 8.14: Effect of option 2 retrofit on vertical force time history for H=0.84m

Overall airvents are effective and cheap retrofitting option for reducing hydrodynamic forces applied to bridge superstructure. They can easily be used to retrofit existing bridges or can be incorporated in the design of new bridge structures. Care must be taken to evaluate the loss of capacity caused by coring the vent holes in bridge superstructure to make sure it does not reduce the structural capacity of the bridge significantly.

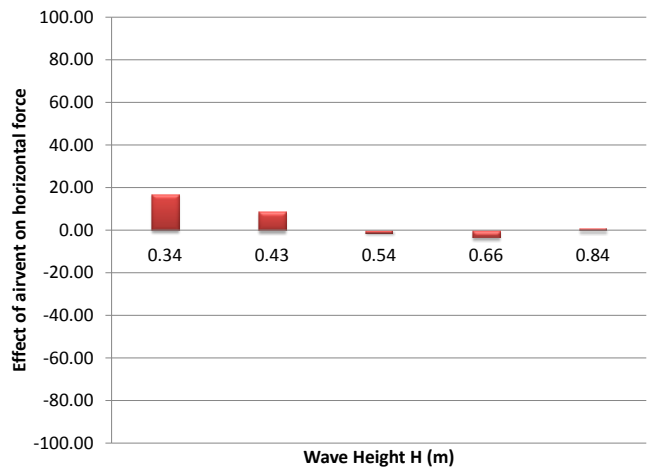


Figure 8.15: Effect of option 2 retrofit on horizontal force for various wave heights

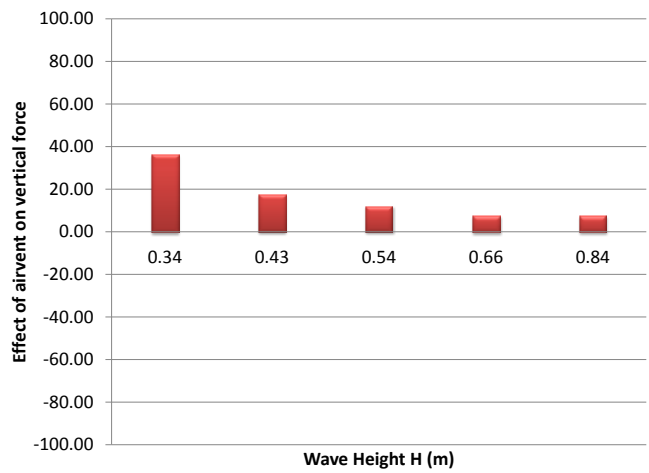


Figure 8.16: Effect of option 1 retrofit on vertical force for various wave heights

Chapter 9

CONCLUDING REMARKS

Understanding the forces acting on highway bridge superstructure is critical to improve the durability of bridges, which can, even if infrequently, be overtopped in Hurricane or Tsunami events. The overall objective of the study was to establish validated computational practice to address research needs of the transportation community in bridge hydraulics via computational fluid dynamic simulations. The study provides modeling capability for the simulation of waves interacting with a typical highway bridge superstructure. The followings conclude the findings and achievements of this study:

- In chapter 4 CFD software was validated by modeling a solitary wave interacting with a simple flat plate. It was shown that the CFD software was well capable of predicting pressure under the flat plate and velocities at different points inside the simulation domain. In addition results of simulation was compared with two other Finite Element codes previously developed. CFD software was able to predict pressure fluctuations under the flat plate with a better accuracy than two previous Finite Element codes developed.
- The validated CFD software was applied to 1:5 scaled old Escambia Bay bridge which was heavily damaged during Hurricane Ivan. Simulation results were compared to experimental data available from the O.H. Hinsdale Wave Research Laboratory at Oregon State University. Six 2D and 3D test cases were designed to investigate the effect of model selection (2D vs 3D), time step and grid resolution on simulation accuracy. Simulations were carried out to predict total horizontal and vertical forces applied to bridge superstructure. It was shown that the two

phase Navier stokes equations were very sensitive to mesh size, time step and boundary conditions used in the simulation. The 2D model was not capable of predicting horizontal and vertical wave forces with reasonable accuracy in a single simulation. While the 2D model with the time step size of $dt = T_p/125$ was capable of predicting vertical wave forces with reasonable accuracy, it could not predict horizontal wave forces with good accuracy even when a very fine mesh was used. Prediction of horizontal wave forces with a reasonable accuracy required time step size of the order of $dt = T_p/625$. Reducing time step to $T_p/625$ in 2D model improved accuracy of horizontal force predictions however it created excessive oscillatory behavior in vertical force time history which was the result of inaccurate modeling of air phase movement under bridge superstructure since the 2D model did not allow the air to move in transverse direction. Test #3 results showed that horizontal wave forces were not sensitive to air entrapment and exclusion of air phase by letting it vent out of simulation domain in fact improved the accuracy of horizontal force predictions even with time step size of $dt = T_p/125$. 3D model predicted horizontal wave forces slightly better than 2D model when similar time steps were used. 3D model was very sensitive to the mesh size used in all three dimensions including transverse direction along the bridge girder and perpendicular to bridge diaphragm. Comparison of Test #5 to Test #6 shows that refinement of mesh size in transverse direction reduced maximum error in vertical forces by 34 percent (table 6.3). In addition to mesh size, mesh aspect ratio was also shown to be important. Comparison of Test #5 to Test #6 results showed the importance of keeping mesh aspect ratio as small as what computer resources allow. In Test #5 the mesh used in free surface region had aspect ratio of 2.4 while in Test #6 the mesh used in free surface had aspect ratio of 4.8. This increase in aspect ratio increased the maximum error in horizontal forces by 5 percent. At the

end of chapter 6 meshing guidelines were proposed which were found suitable for wave-bridge interaction problem with emphasis on accurate modeling of air phase under the bridge superstructure.

- Some Test #6 force time histories showed oscillatory behavior. This include force time histories for wave heights of $H=0.34\text{m}$, $H=0.43\text{m}$, and $H=0.54\text{m}$ (figure 6.41). As the wave height increased the oscillatory behavior decreased in all test cases. While biggest amplitude oscillations happened in force time history for wave height of $H=0.34\text{m}$, force time history for wave height of $H=0.84\text{m}$ did not show any oscillatory behavior. The amplitude of these slamming oscillations in force time history for wave height of $H=0.34\text{m}$ was directly related to mesh size, time step, and specially to the boundary condition used on the side of simulation domain (2D model vs. 3D model). These high frequency slamming oscillations were not seen in experimental data available from Oregon State University. How ever they were witnessed in experimental data available from University of Florida experiments. This suggests, that existence of slamming oscillations in force time history depended on experimental setup and bridge superstructure properties (mass and damping coefficient) under experiment. Since the bridge superstructure under experiment in Oregon State University was bigger and heavier than bridge superstructure under experiment in University of Florida, we conclude that as bridge superstructure gets bigger and heavier the structure does not respond to a high frequency slamming force. This means as the wave strikes the bridge, an impact pressure may be generated but this pressure does not show itself as a reaction force at the bent cap. The large mass of bridge superstructure dissipates this impact. There may cause localized forces and resulting damage such as concrete spalling or cracking, but it is unlikely that these forces were responsible for the failures witnessed during Hurricanes Ivan and Katrina. Therefore inclusion

of these slamming oscillations witnessed in CFD simulations may not be required for prototype scale bridge superstructure.

- At the end of chapter 6, effect of turbulent modeling on hydrodynamic forces applied to bridge superstructure was evaluated by using K-omega turbulent model and comparing the simulation results to horizontal and vertical forces calculated using inviscid model. K-omega model, used with default settings in CFD software and mesh size and time step similar to mesh size and time step used in Test #6, was not able to decrease the magnitude of error witnessed in force time history of horizontal and vertical forces for wave height of $H=0.34\text{m}$. For wave height of $H=0.84\text{m}$, K-omega model was able to improve predictions of horizontal and vertical forces by 4 percent and 12 percent respectively. This suggests that as wave height increase and wave-bridge interaction becomes more violent, turbulent modeling and viscous effects need to be considered.
- Since there are a lot of concerns about scale effects when using empirical equations which are developed from small scale model experiments especially when entrapment of air is involved, in chapter 7 CFD software was used to evaluate scale effects in wave bridge interaction problem. A bridge prototype with old Escambia Bay bridge dimensions was built. Equivalent wave heights and period were calculated using Froude similitude laws from the wave heights and periods used in model simulations. The number of mesh per wave length and time step used in these simulations were similar to the ones used in Test #6. The forces obtained from CFD simulations for prototype bridge were compared to forces calculated using Froude similitude law from model bridge simulations. Both horizontal and vertical forces calculated for the prototype bridge using Froude similitude law matched the simulation results for prototype bridge. In addition force

time history for prototype bridge showed a very similar pattern to force time history for model bridge with slamming oscillation existing for only certain wave heights ($H=1.7\text{m}$, $H=2.15\text{m}$, $H=2.7\text{m}$). This proves validity of Froude similitude law for complex wave structure interaction problems even when the effect of air entrapment and entrainment is considered. In addition, CFD simulation results for model and prototype bridge were compared with recently published AASHTO guidelines. Horizontal wave forces for the range of wave heights simulated, compared reasonably well with the total horizontal forces calculated using guideline equations. The total vertical force (which included the slamming force) predicted by the guidelines was larger than the measured vertical force for almost every wave height except $H=0.34\text{m}$ and its equivalent wave height in prototype simulations $H=1.7\text{m}$. The guideline slightly under predicted the total vertical force for $H=0.34\text{m}$ in model bridge simulation and $H=1.7\text{m}$ in prototype bridge simulation. For other wave heights the maximum vertical force predicted by guideline was conservative.

- Since air entrapped between bridge girders and diaphragms was determined to be a major contributing factor behind highway bridge failures during recent hurricanes, in chapter 8 two retrofitting options were evaluated in terms of their efficacy in reducing hydrodynamics forces applied to bridge superstructure by reducing the amount of air entrapped under bridge superstructure. These two options were using airvents in bridge deck and using airvents in bridge diaphragms. Simulations in chapter 8 showed that airvents in bridge deck could be very effective in reducing both the quasi-steady and slamming forces for some wave heights. For example for wave height of $H=0.34\text{m}$, 5cm airvents in bridge deck reduced vertical wave forces by 60 percent. However as the wave height increased the efficacy of airvents decreased significantly to the extent that for $H=0.84\text{m}$ the

reduction in vertical force was only 17 percent. This was mainly because as the wave height increased the velocity of air moving under the bridge superstructure also increased, as a result 5 cm vent hole might not be able to vent out the air in a timely manner as the wave passed the bridge width. In addition, since for $H=0.84\text{m}$ wave, there was a lot of wave overtopping, The capacity of the airvents were significantly reduced because the water on top of bridge deck clogged the airvents. Efficacy of airvents in bridge diaphragms was also investigated. Comparing to airvents in bridge deck, airvents in bridge diaphragm were less effective in reducing hydrodynamic forces applied to bridge superstructure. This was mainly because when wave interacted with bridge superstructure, bridge girders and diaphragms were inundated. Therefore they were not as effective as airvents in bridge deck in venting out the air from beneath the bridge superstructure.

The ability of CFD to model a complex flow such as described in this dissertation would provide a powerful tool to predict the hydrodynamic forces under various conditions and furthermore to devise effective disaster prevention plan against bridge failure. Overall, the experimental results and CFD model provide the bridge designer with a wealth of information on the bridges response to hydrodynamic forces due to violent waves. The flexibility of CFD models to represent almost any scenario means that they have a definite advantage over physical experimentation.

Reference List

- AASHTO 2008. Guide specifications for bridges vulnerable to coastal storms (bvcs-1).
- Bea, R., Iversen, R., and Xu, T. 2001. Wave-in-deck forces on offshore platforms. *Journal of Offshore Mechanics and Artic Engineering*, 123:10–12.
- Bea, R., T. Xu, J. S., and Ramos, R. 1999. Wave forces on decks of offshore platforms. *Journal of Waterway, Port, Coastal and Ocean Engineering, American Society of Civil Engineers*, 125:136–144.
- Boussinesq, J. 1872. Theorie des ondes et des remous qui se propagent le long d'un canal rectangulaire horizontal en communiquant au liquiide contenu dans ce canal de vitesses sensiblement parreilles de la surface au fond. *Journal de Mathematiques Pures et Appliquees*, 17:55–108.
- Bradner, C. and Cox, D. 2008. Large scale laboratory observations of wave forces on highway bridge super structure. *Master Thesis Submitted to Oregon State University*.
- Brody, J., Kasir, R., and Weiss, D. 2011. Oscillations of a water column beneath trapped air. *American Journal of Physics*.
- CD-adapco 2010. User guide for star-ccm+ version 5.06.010.
- Chen, Q., Wang, L., and Haihong, Z. in press. Hydrodynamic investigation of coastal bridge callapse during hurricane katrina. *Journal of Hydraulic Engineering*.
- Cuomo, G., Shimosako, K., and Takahashi, S. 2009. Wave-in-deck loads on coastal bridges and the role of air. *Journal of Coastal Engineering*, 56:793–809.
- Demirdzic, I., Lilek, Z., and Peric, M. 1993. A collocated finite volume method for predicting flows at all speeds. *Int.J. for Numerical methods in Fluids*, 16:1029–1050.
- Demirdzic, I. and Musaferiya, S. 1995. Numerical method for coupled fluid flow, heat transfer and stress analysis using unstructured moving meshes with cells of arbitrary topology. *Comput. Methods Appl. Mech. Eng.*, pages 1–21.

- Denson, K. 1978. Wave forces on causeway-type coastal bridges. *Water Resource Research Institute, Mississippi State University*, 42pp.
- Denson, K. 1980. Wave forces on causeway-type coastal bridges: effects of angle of wave incidence and cross-section shape. *Water Resource Research Institute, Mississippi State University*, 242pp.
- Douglass, S., Chen, Q., Olsen, J., and Edge, B. 2006. Wave forces on bridge decks. *U.S. Department of Transportation Federal Highway Administration*.
- El.Ghamry, O. 1963. Wave forces on a dock. *Hydraulic Engineering Laboratory, Institute of Engineering Research Technical Report HEL-9-1, University of California, Berkeley, California*, page 206pp.
- FDOT 2008. Design build contracts status as of 09/30/2008. retrieved october 14, 2008, from florida department of transportation.
- FEMAa 2006. Hurricane katrina in the gulf coast summary rep. *FEMA548*.
- FEMAb 2006. Hurricane katrina in the gulf coast: observation, recommendations, and technical guidance. *FEMA549*.
- Fenton, J. 1972. A ninth-order solution for the solitary wave. *Journal of Fluid Mechanics*, 53:257–271.
- Ferziger, Joel, H., and Peric, M. 2002. *Computational Methods for Fluid Dynamics*. Springer-Verlag, Berlin.
- (FHWA), F. H. A. 2009. Hydrodynamic forces on inundated bridge decks. *Publication No. FHWA-HRT-09-028*.
- French, J. 1970. Wave uplift pressure on horizontal platforms. *Proceedings of the Civil Engineering in the Oceans Conference, American Society of Civil Engineers*, pages 187–202.
- Grimshaw, R. 1970. The solitary wave in water of variable depth. *Journal of Fluid Mechanics*, 42:639–656.
- Houston, A., Lawrimore, T., Levinson, J., Lott, D., McCown, N., Stephens, S., and Wuerts, D. 2005. Hurricane katrina: A climatological perspective-preliminary report. *Technical Report 2005-01*.
- Huang, W. and Xiao, H. 2009. Numerical modeling of dynamic wave force acting on escambia bay bridge deck during hurricane ivan. *Waterway, Port, Coastal, and Ocean Engineering*, 135.

- Hughes, S. 1993. Physical models and laboratory techniques in coastal engineering. *World Scientific Publishing*.
- Iradjpanah, K. 1983. Wave uplift pressure on horizontal platforms. *Ph.D dissertation submitted to University of Southern California*.
- Jin, J. and Meng, B. 2011. Computation of wave loads on the superstructures of coastal highway bridges. *Ocean Engineering*.
- Kaplan, P. 1992. Wave impact forces on offshore structures: re-examination and new interpretations. *Proceedings of the 24th Annual Conference on Offshore Technology, OTC 6814*, pages 79–86.
- Kaplan, P., Murray, J., and Yu, W. 1995. Theoretical analysis of wave impact forces on platform deck structure. *Proceedings of the 14th International Conference on Offshore Mechanics and Arctic Engineering, American Society of Mechanical Engineers*, 1-A:189–198.
- Lai, C. 1986. Wave uplift on platforms or docks in variable depth. *Coastal Engineering Proceedings*.
- Laitone, E. 1963. Higher order approximation to nonlinear waves and the limiting heights of cnoidal, solitary and stokes waves. *Beach Erosion Board, U.S. Department of the Army, Corps of Engineers, Technical Memorandum No. 133*.
- Leonard, B. 1997. Bounded higher-order upwind multidimensional finite volume convection-diffusion algorithms. *Advances in Numerical Heat Transfer*, chap 1:1–57.
- McConnell, K., Allsop, W., and Cruickshank, I. 2004. *Piers, Jetties, and related structures exposed to waves: Guidelines for hydraulic loadings*. Thomas Telford Press, London.
- McCowan, J. 1891. On the solitary wave. *Philosophy Magazine*, 32:45–58.
- Menter, F. 1994. Two-equation eddy-viscosity turbulence modeling for engineering applications. *AIAA Journal*, pages 1598–1605.
- Mhaut, B. L., Divoky, D., and Lin, A. 1968. Shallow water waves: A comparison of theories and experiments. *Proceedings of 11th Conference of Coastal Engineering, Vol. 1*.
- Mozaferija, S. and Peric, M. 1998. Computation of free surface flows using interface-tracking and interface-capturing methods. *Computational Mechanics Publications*, chap 2.

- Overbeek, J. and Klabbers, I. 2001. Design of jetty decks for extreme vertical loads. *Proceedings of the Ports 2001 Conference, American Society of Civil Engineers, 10pp.*
- Sawyer, A. 2008. Determination of hurricane surge wave forces on bridge superstructures and design/retrofit options to mitigate or sustain these forces. *Master thesis, Auburn University.*
- Schumacher, T., Higgins, C., Bradner, C., Cox, D., and Yim, S. 2008. Large-scale wave flume experiments on highway bridge superstructures exposed to hurricane wave forces. *Proceedings of the 6th National Seismic Conference on Bridges and Highways, Charleston, South Carolina.*
- Sheppard, D. and Marin, J. 2009. Wave loading on bridge decks. *Report submitted to Florida Department of Transportation (FDOT), FDOT BD545-58.*
- TCLEE 2006. Hurricane katrina performance of transportation systems. *ASCE Technical Council on Lifeline Earthquake Engineering Monograph No. 29.*
- Versteeg, H. and Malalasekera, W. 2007. An introduction to computational fluid dynamics: The finite volume method (2nd edition).
- Wang, H. 1967. Estimating wave pressure on a horizontal pier. *Technical Report R546, Naval Civil Engineering Laboratory, Port Hueneme, California.*
- Wang, H. 1970. Water wave pressure on horizontal plate. *Journal of the Hydraulics Division, American Society of Civil Engineers, 96.*
- Wikipedia 2012. John scott russell — wikipedia, the free encyclopedia. [Online; accessed 15-October-2012].

Appendix A

DISCRETIZATION SCHEMES USED IN STAR CCM+

In this appendix discretization schemes used by STAR-CCM+ to discretize Navier Stokes equations are briefly explained by showing these schemes for discretization of transport equation for a scalar variable ϕ . More information about these techniques can be found in comprehensive manual that comes with STAR-CCM+ (CD-adapco (2010)).

A.1 Transport Equation in Discrete Form

Transport of scalar quantity ϕ in integral form is represented by following equation:

$$\frac{d}{dt} \int_V \rho \phi dV + \int_A \rho \phi (\mathbf{v} - \mathbf{v}_g) \cdot d\mathbf{a} = \int_A \Gamma \nabla \phi \cdot d\mathbf{a} + \int_V S_\phi dV \quad (\text{A.1})$$

from left to right the terms in this equation are, the transient term, the convective flux, the diffusive flux and the volumetric source term. Applying Finite Volume to above equation we get the following discrete equation for cell 0:

$$\frac{d}{dt} (\rho \phi V)_0 + \sum_f [\rho \phi (\mathbf{v} \cdot \mathbf{a} - G)]_f = \sum_f (\Gamma \nabla \phi \cdot \mathbf{a})_f + (S_\phi V)_0 \quad (\text{A.2})$$

where G is grid flux computed from mesh motion given by $G_f = (a \cdot v_g)_f$. Transient term is discretized according to second order temporal scheme which make use of current time level $n+1$, as well as those from the previous two time levels, n and $n-1$, as follows:

$$\frac{d}{dt}(\rho\phi V)_0 = \frac{3(\rho_0\phi_0)^{n+1} - 4(\rho_0\phi_0)^n + (\rho_0\phi_0)^{n-1}}{2\Delta t} V_0 \quad (\text{A.3})$$

On the first time step a first order discretization is used since only two time levels are available. The source term is approximated as the product of the value of the integrand S_ϕ , evaluated at cell centroid and the cell volume, V :

$$\int_V S_\phi dV = (S_\phi V)_0 \quad (\text{A.4})$$

Convective term at face is discretized as follows:

$$[\phi\rho(v \cdot a - G)]_f = (\dot{m}\phi)_f = \dot{m}_f\phi_f \quad (\text{A.5})$$

where ϕ_f and \dot{m}_f are the scalar values and mass flow rates at the face, respectively. Several schemes are offered by STAR-CCM+ for computation of face value ϕ_f . In present study we used second order upwind scheme as follows:

$$(\dot{m}\phi)_f = \begin{cases} \dot{m}_f\phi_{f,0} & \text{for } \dot{m}_f \geq 0 \\ \dot{m}_f\phi_{f,1} & \text{for } \dot{m}_f < 0 \end{cases} \quad (\text{A.6})$$

where the face values $\phi_{f,0}$ and $\phi_{f,1}$ are linearly interpolated from the cell values on either side of the face as follows:

$$\phi_{f,0} = \phi_0 + s_0(\nabla\phi)_{r,0} \quad (\text{A.7})$$

$$\phi_{f,1} = \phi_1 + s_1(\nabla\phi)_{r,1} \quad (\text{A.8})$$

where $s_0 = x_f - x_0$, $s_1 = x_f - x_1$, and $(\nabla\phi)_{r,0}$ and $(\nabla\phi)_{r,1}$ are limited reconstruction gradients in cell 0 and 1 respectively. The flux at the boundary is evaluated as:

$$(\dot{m}\phi)_f = \begin{cases} \dot{m}_f\phi_{f,0} & \text{for } \dot{m}_f > 0 \\ \dot{m}_f\phi_f & \text{for } \dot{m}_f < 0 \end{cases} \quad (\text{A.9})$$

where $\phi_{f,0}$ is interpolated from the cell value using the limited reconstruction gradients in cell 0 (see equation A.7) and ϕ_f is the face value as dictated by boundary conditions. The diffusive flux D_f is discretized as follows:

$$D_f = \sum_f (\Gamma\nabla\phi \cdot a)_f \quad (\text{A.10})$$

where Γ , $\nabla\phi$ and a represent the face diffusivity, gradient and area vector, respectively. For obtaining an accurate second-order expression for an interior face gradient that implicitly involve the cell values ϕ_0, ϕ_1 , the following decomposition is used:

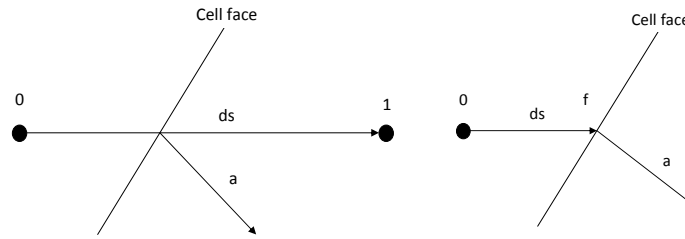


Figure A.1: decomposition used in calculation of Diffusion term

$$\nabla\phi_f = (\phi_1 - \phi_0)\vec{\alpha} + \bar{\nabla}\phi - (\bar{\nabla}\phi \cdot \vec{ds})\vec{\alpha} \quad (\text{A.11})$$

where $\vec{\alpha} = \frac{\vec{a}}{\vec{a} \cdot \vec{d}s}$, $\vec{d}s = \vec{x}_1 - \vec{x}_0$, and $\bar{\nabla}\phi = \frac{\nabla\phi_0 + \nabla\phi_1}{2}$. The diffusion flux at an interior face may be written:

$$D_f = \Gamma_f \nabla\phi_f \cdot a = \Gamma_f [(\phi_1 - \phi_0)\vec{\alpha} \cdot a + \bar{\nabla}\phi \cdot a - (\bar{\nabla}\phi \cdot \vec{d}s)\vec{\alpha} \cdot a] \quad (\text{A.12})$$

where Γ_f is average value of the cell values. Second term and third term in above equation represent the secondary gradient or cross diffusion contribution. They are necessary for maintaining accuracy on non-orthogonal meshes. For boundary faces a similar decomposition is used

$$D_f = \Gamma_f \nabla\phi_f \cdot a = \Gamma_f [(\phi_f - \phi_0)\vec{\alpha} \cdot a + \nabla\phi_0 \cdot a - (\nabla\phi_0 \cdot \vec{d}s)\vec{\alpha} \cdot a] \quad (\text{A.13})$$

where $\vec{d}s = \vec{x}_f - \vec{x}_0$. Similar to interior faces the second and third term are cross diffusion contribution which can be neglected if mesh is orthogonal.

A.2 Gradient Computation

STAR-CCM+ first calculates unlimited reconstruction gradients. Using unlimited reconstruction gradients direct is problematic because it may in some instances exceed the cell values bounding the face. For this reason it is necessary to limit reconstruction gradients by scaling them appropriately in each cell. Once these unlimited reconstruction gradients are limited they are used to evaluate the cell gradients to reconstruct face values for flux computations. Unlimited reconstruction gradients for pressure is calculated using weighted least squares method. In weighted least square method the initial

unlimited reconstruction gradients $(\nabla\phi)_r^u$ in cell 0 are computed using the following weighted list square formula:

$$(\nabla\phi)_r^u = \left[\sum_f \frac{ds \otimes ds}{ds \cdot ds} \right]^{-1} \left[\sum_f \frac{(\phi_0 - \phi_n) ds}{ds \cdot ds} \right] \quad (\text{A.14})$$

where $\vec{ds} = \vec{x}_n - \vec{x}_0$, and \vec{x}_0 and \vec{x}_n representing centroid of cell 0 and neighbor cell addressed through face and ϕ_0 and ϕ_n represent the data values in cell 0 and its neighbors. Gauss divergence theorem is used to calculate unlimited reconstruction gradients for calculation of other variables such as velocity. Gauss divergence theorem states that:

$$\int_V \nabla\phi dV = \int_A \phi da \quad (\text{A.15})$$

written in discrete form allows us to compute initial unlimited reconstruction gradients as:

$$(\nabla\phi)_r^u = \frac{1}{V_0} \sum_f \phi_f a_f \quad (\text{A.16})$$

where the face value ϕ_f is approximated by the arithmetic average of the adjacent cell values as $\phi_f = \frac{\phi_0 + \phi_1}{2}$. Limited reconstruction gradients for cell 0 are calculated using the scale factor α as follows:

$$(\nabla\phi)_{r,0} = \alpha (\nabla\phi)_{r,0}^u \quad (\text{A.17})$$

where $\alpha = \min(\alpha_f)$ and α_f is given by following equation:

$$\alpha_f = \frac{2r_f + 1}{r_f(2r_f + 1) + 1} \quad (\text{A.18})$$

r_f is given by:

$$r_f = \begin{cases} \frac{\Delta_f}{\Delta_{\max}} & \text{for } \Delta_f > 0 \\ \frac{\Delta_f}{\Delta_{\min}} & \text{for } \Delta_f \leq 0 \end{cases} \quad (\text{A.19})$$

Δ_f is given by:

$$\Delta_f = \phi_{f,0} - \phi_0 = s_0(\nabla\phi)_{r,0}^u \quad (\text{A.20})$$

where:

$$\Delta_{\max} = \phi_0^{\max} - \phi_0 \quad (\text{A.21})$$

$$\Delta_{\min} = \phi_0^{\min} - \phi_0 \quad (\text{A.22})$$

For cell 0, ϕ_0^{\max} and ϕ_0^{\min} quantities can be defined as:

$$\phi_0^{\max} = \max(\phi_0, \phi_{\text{neighbors}}) \quad (\text{A.23})$$

$$\phi_0^{\min} = \min(\phi_0, \phi_{\text{neighbors}}) \quad (\text{A.24})$$

where $\phi_{\text{neighbors}}$ represents the cell values in each neighbor that has a common face with cell-0. Reconstruction gradients explained in previous section are used for computing bounded face values from cell values and are used for convective quantities. Cell gradients are used in many other places such as secondary gradients for diffusive terms and pressure gradients in pressure-velocity coupling. The improved estimates of face values obtained from reconstruction gradients can in turn be used to obtain better estimates of cell gradients. Using Gauss divergence theorem we obtain:

$$\nabla\phi = \frac{1}{V_0} \sum_f \phi_f \quad (\text{A.25})$$

Where the face value is approximated by arithmetic average of the face values from adjacent cell values as $\phi_f = \frac{\phi_{f,0} + \phi_{f,1}}{2}$. where $\phi_{f,0}$ and $\phi_{f,1}$ are obtained using equation A.7, A.8.